# RAMAN AND BRILLOUIN SPECTROSCOPIC STUDIES OF SINGLE CRYSTALS OF $CH_4$ AND $CD_4$

CENTRE FOR NEWFOUNDLAND STUDIES

TOTAL OF 10 PAGES ONLY
MAY BE XEROXED

(Without Author's Permission)

EUGENE GREGORYANZ

# RAMAN AND BRILLOUIN SPECTROSCOPIC STUDIES OF SINGLE CRYSTALS OF $CH_4$ AND $CD_4$

By

©Eugene Gregoryanz
M.Sc., Moscow State University

A THESIS SUBMITTED TO THE SCHOOL OF GRADUATE
STUDIES IN PARTIAL FULFILLMENT OF THE
REQUIREMENTS FOR THE DEGREE OF
DOCTOR OF PHILOSOPHY

DEPARTMENT OF PHYSICS
MEMORIAL UNIVERSITY OF NEWFOUNDLAND

1998

ST. JOHN'S NEWFOUNDLAND

National Library
of Canada

Acquisitions and
Bibliographic Services

395 Wellington Street
Ottawa ON K1A 0N4
Canada

Bibliothèque nationale
du Canada

Acquisitions et
services bibliographiques

395, rue Wellington
Ottawa ON K1A 0N4
Canada

Your file Votre référence

Our file Notre référence

The author has granted a non-exclusive licence allowing the National Library of Canada to reproduce, loan, distribute or sell copies of this thesis in microform, paper or electronic formats.

L'auteur a accordé une licence non exclusive permettant à la Bibliothèque nationale du Canada de reproduire, prêter, distribuer ou vendre des copies de cette thèse sous la forme de microfiche/film, de reproduction sur papier ou sur format électronique.

The author retains ownership of the copyright in this thesis. Neither the thesis nor substantial extracts from it may be printed or otherwise reproduced without the author's permission.

L'auteur conserve la propriété du droit d'auteur qui protège cette thèse. Ni la thèse ni des extraits substantiels de celle-ci ne doivent être imprimés ou autrement reproduits sans son autorisation.

0-612-36204-3

Canada

## Abstract

A technique has been developed for obtaining single crystals of molecular crystals in solid phases which can be reached only from other solid phases. The technique was used to produce large ($\approx 50$ mm$^3$) single crystals of $CH_4$-I and $CD_4$-I in a liquid helium cryostat cell, which then were successfully cooled down below the phase transition temperatures. The crystals were studied by the means of Raman and Brillouin spectroscopies. X-ray Laüe diffraction techniques were applied to determine the orientation of the crystals in the laboratory frame. The elastic constants of $CH_4$-I, II and $CD_4$-I, II and III were determined as a function of temperature from 90 K to 15 K. The possible space groups of $CD_4$-III were determined on the basis of Brillouin data.

Bulk adiabatic moduli and shear moduli were calculated from the elastic constants as functions of temperature. The elastic constants were used to calculate the acoustic velocities in high symmetry planes, and also the Debye temperature which is in agreement with previous results. The rotational specific heat of each species was calculated as a function of temperature.

Raman spectra of the fundamental modes $\nu_1$ and $\nu_3$ were recorded and their shifts and full width at half height were determined as functions of temperature through the phase transition.

# Acknowledgements

I would like to express my appreciation and gratitude to my supervisors Dr. M.J. Clouter and late Dr. H. Kiefte for their support and guidance. I would like to thank Dr. Clouter for helping me to write this thesis.

Also, I am grateful to Dr. N. Rich for the helpful discussions we had and to Dr. R. Goulding for his help in the experiment. I thank my collegues Dr. C. Tulk and Mr. T. Andrews for the help and discussions we had over the past years.

And my special thanks are due to Mr. W. Holly who was providing me with liquid helium and nitrogen all these years without which the experiment would never have succeeded.

# Table of Contents

**1 Introduction** **1**

1.1 Noble Gases and Methane . . . . . . . . . . . . . . . . . . . . . . . . . . 1

1.2 Molecules of Methane and Interaction Between Them . . . . . . . . . . . 4

1.3 Elastic Properties of Methane . . . . . . . . . . . . . . . . . . . . . . . . 7

1.4 Order-Disorder Phase Transitions . . . . . . . . . . . . . . . . . . . . . . 12

1.5 Phases of $CH_4$ and $CD_4$ . . . . . . . . . . . . . . . . . . . . . . . . 17

1.5.1 Methane . . . . . . . . . . . . . . . . . . . . . . . . . . . 17

1.5.2 Heavy Methane . . . . . . . . . . . . . . . . . . . . . . . 17

**2 Theory of Elasticity, Brillouin and Raman Spectroscopy** **21**

2.1 Theory of Elasticity . . . . . . . . . . . . . . . . . . . . . . . . . . . . . 21

2.1.1 The Stress Tensor . . . . . . . . . . . . . . . . . . . . . . 22

2.1.2 The Strain Tensor . . . . . . . . . . . . . . . . . . . . . . 23

2.1.3 Elastic Constants, Stress and Strain . . . . . . . . . . . . 24

2.2 Brillouin Scattering . . . . . . . . . . . . . . . . . . . . . . . . . . . . . 26

2.2.1 Acoustic Waves and Elastic Constants . . . . . . . . . . . 27

2.3 Raman Scattering . . . . . . . . . . . . . . . . . . . . . . . . . . . . . . 34

**3 Experimental Apparatus and Technique** **41**

3.1 Brillouin Apparatus . . . . . . . . . . . . . . . . . . . . . . . . . . . . . 41

3.1.1 Optical setup . . . . . . . . . . . . . . . . . . . . . . . . 41

3.1.2 Fabry-Perot Interferometer . . . . . . . . . . . . . . . . . 43

3.2 Raman Apparatus . . . . . . . . . . 46
3.3 Cryogenic Setup and Sample Preparation . . . . . . . . . . 47
3.3.1 Helium Cryostat . . . . . . . . . . 47
3.3.2 Single Crystal Growth and Cooling . . . . . . . . . . 51

**4 Raman Measurements 53**

4.1 $CH_4$ . . . . . . . . . . 53
4.2 $CD_4$ . . . . . . . . . . 60

**5 Brillouin Measurements and Analysis for $CH_4$ 66**

5.1 Crystal Orientation and Refractive Indices . . . . . . . . . . 66
5.2 Determination of Elastic Constants . . . . . . . . . . 68
5.3 Results . . . . . . . . . . 69
5.3.1 Elastic Moduli . . . . . . . . . . 69
5.3.2 Thermodynamic Properties . . . . . . . . . . 79

**6 Brillouin Measurements and Analysis for $CD_4$ 87**

6.1 Crystal Growth of $CD_4$ . . . . . . . . . . 87
6.1.1 Density and Refractive Indices of $CD_4$ . . . . . . . . . . 88
6.2 Results . . . . . . . . . . 89
6.2.1 Elastic Moduli . . . . . . . . . . 89
6.2.2 Thermodynamic Properties . . . . . . . . . . 98

**7 Discussion 107**

**Bibliography 112**

**A Brillouin scattering data 122**

**B X-ray diffraction pattern and Brillouin spectra** **125**

# List of Figures

1.1 The comparison of liquid and disordered crystals. X is position and Ω orientation, < .. > denotes complete order, {..}partial order and (..) complete disorder. . . . . . . . . . . . . . . . . . . . . . . . . . . . . . . 3

1.2 Molecule of methane (schematic) . . . . . . . . . . . . . . . . . . . . . . . 6

1.3 Arrangement of the eight sublattices in $CH_4$ and $CD_4$ in the phase II (space group F$m3c$) with the disordered molecule in the symmetry center. Adapted from Ref. [81] . . . . . . . . . . . . . . . . . . . . . . . . . . 18

1.4 Proposed phase diagram of $CH_4$. Adapted from Ref. [31] . . . . . . . . . 19

1.5 Phase diagram of $CH_4$ at low pressures and temperatures. Adapted from Ref. [57]. . . . . . . . . . . . . . . . . . . . . . . . . . . . . . . . . . 19

2.1 The forces acting on the faces of an elementary cube . . . . . . . . . . . 22

2.2 The transformation of a string under deformation . . . . . . . . . . . . . 23

2.3 Brillouin scattering: (a) wave picture (b) quantum picture . . . . . . . . 29

2.4 Rayleigh and Raman Scattering . . . . . . . . . . . . . . . . . . . . . . . 39

3.1 Experimental optical setup for Brillouin experiment: $F_1$ - narrow band pass filter, $L_3$ - focusing lens, He-Ne - alignment laser, $M_2$ - mirror, C - collimator, $Ar^+$ - argon laser. PM - photomultiplier tube, AD - amplifier discriminator, $F_2$ - narrow band pass filter, $L_4$, $L_5$ -lenses, $D_1$, $D_2$ - pinholes, DAS-2 - data acquisition system. . . . . . . . . . . . . . . . . . . . . . . 42

3.2 Optical path difference, s, between two reflected beams. . . . . . . . . . 44

3.3 Experimental setup for Raman experiment: $F_1$ - narrow band pass filter, $L_3$ - focusing lens, He-Ne - alignment laser, $M_2$ - mirror, C - collimator, $Ar^+$ - argon laser, $L_1$, $L_1$ - lenses, DAS-1 - data acquisition system, P - polarizer, S - scramble. . . . . . . . . . . . . . . . . . . . . . . . . . 48

3.4 The cryostat quartz cell. . . . . . . . . . . . . . . . . . . . . . . . . . 49

4.1 The Raman spectra of $\nu_1$ and $\nu_3$ and $2\nu_2$ of $CH_4$ at T=89 K. The sharp peaks around $\nu_1$ are the peaks from the thorium/neon calibrating lamp. The spectra were collected without polarizer and scrambler. . . . . . . 56

4.2 Typical Raman spectra of $\nu_1$ and $\nu_3$ of $CH_4$. (a) and (c) show the $\nu_1$ spectrum in phases I and II, respectively, and (b) and (d) are corresponding spectra for $\nu_3$. $\nu_3$ was recorded with the polarizer axis perpendicular to the polarization vector of the scattered light. . . . . . . . . . . . . . . . 57

4.3 The shift (a) and full width (b) at half height of $\nu_1$ of $CH_4$ as a function of temperature. (◇) indicate the second peak which appeared after the phase transition. (△) are from Ref. [131]. The errors in measurements of shift are of the size of the symbols. The errors in measurements of FWHM are estimated to be ~ 2%. The dashed line is positioned at the phase transition temperature of 20.5 K and at the liquid-solid phase at 90.67 K. 58

4.4 The shift (a) and full width at half height (b) of $\nu_3$ of $CH_4$ as a function of temperature. The (●) are for decreasing and (◇) for increasing temperatures. The inset (c) shows a magnified view of the FWHM around the phase transition temperature. The errors in measurements of shift are of the size of the symbols. The errors in measurements of FWHM are estimated to be ~ 2%. The dashed line is positioned at the phase transition temperature of 20.5 K and at the liquid-solid phase at 90.67 K. . . . . 59

4.5 Unprocessed representative Raman spectra of $CD_4$. All spectra but the one at T=18 K are collected without polarizer. The spectrum at T=18 K was collected with the polarizer axis perpendicular to the polarization vector of the scattered light. The small peak between $\nu_1$ and $2\nu_2$ is the $\nu_1$ line of $CD_3H$. . . . . . . . . . . . . . . . . . . . . . . . . . . . . 62

4.6 Smoothed spectra of $\nu_1$ (a, c, e) and $\nu_3$ (b, d, f) of $CD_4$ in three phases with phase I at the top. $\nu_1$ was recorded with the polarizer axis parallel to vector of the scattered light and $\nu_3$ with the axis perpendicular. . . . . 63

4.7 The shift (a) and full width at half height (b) of $\nu_1$ of $CD_4$ as a function of temperature. (◇) indicates the second peak which appeared after the first phase transition. The errors in measurements are comparable to the symbol size. The errors in measurements of FWHM are estimated to be ~ 2%. The dashed lines are positioned at the phase transition temperatures $T_c$=27.1 K and 22.1 K and at the liquid-solid phase boundary at 88.78 K. 64

4.8 The shift (a) and full width at half height (b) of $\nu_3$ of $CD_4$ as a function of temperature. (◇) indicates the second peak which appeared after the second phase transition. The inset (c) shows a magnified view of FWHM around the phase transition temperature. The errors in measurements are comparable to the symbol size. The errors in measurements of FWHM are estimated to be ~ 2%. The dashed lines are positioned as in Fig. 4.7. . . 65

5.1 Representative Brillouin spectra of $CH_4$ in phases I (a) and II (b). The Rayleigh peaks are labeled $R_i$, longitudinal $L_i$, where $i$ is the number of corresponding Rayleigh and longitudinal peak. Transverse modes are labeled $T_{(s,f)i}$ where $s,f$ stand for slow and fast transverse modes and $i$ shows the Rayleigh peak to which a given transverse peak belongs. . . . . 70

5.2 Calculated (solid lines) and measured (solid circles) frequency shifts of $CH_4$-I at 23 K. . . . . . . . . . . . . . . . . . . . . . . . . . . . . 73
5.3 Elastic constants of $CH_4$ as a function of temperature over the investigated temperature range. The error bars shown represent the standard deviation in the best fit parameters and uncertainties in the frequency shift and crystal orientation. The dashed line is positioned at the phase transition temperature of 20.5 K. The solid lines in the phase II are drawn as guides to the eye only. . . . . . . . . . . . . . . . . . . . . . . . . . . . . 75
5.4 Elastic constants of $CH_4$ as a function of temperature around the phase transition temperature. The error bars shown are as in Fig. 5.3. The dashed line is positioned as in Fig. 5.3. The solid lines in the phase II are drawn as guides to the eye only. . . . . . . . . . . . . . . . . . . . . . . . 76
5.5 Elastic constants of $CH_4$ as a function of temperature. The combinations correspond to the longitudinal and two transverse waves in the $< 110 >$ direction. The error bars shown are from the errors in elastic constants as in Fig. 5.3. The dashed line is positioned as in Fig. 5.3. . . . . . . . . . . 77
5.6 Elastic moduli of $CH_4$ as a function of temperature: bulk modulus (a), shear modulus (b). The error bars shown are from errors in elastic constants as in Fig. 5.3. The dashed line is positioned as in Fig. 5.3. . . . . 78
5.7 (a) $\delta=(C_{12}\text{-}C_{44})/C_{12}$ of $CH_4$ as a function of temperature. (b) Anisotropy factor A of $CH_4$ . The error bars shown are from the errors in elastic constants as in Fig. 5.3. The dashed line is positioned as in Fig. 5.3. . . 80
5.8 Acoustic velocities of $CH_4$ (in $ms^{-1}$) in high symmetry planes in phase I at 89 K. (a) (100) plane. (b) (110) plane. . . . . . . . . . . . . . . . . . . . 81
5.9 Acoustic velocities of $CH_4$ (in $ms^{-1}$) in high symmetry planes in phase II at 15.5 K. (a) (100) plane. (b) (110) plane. . . . . . . . . . . . . . . . . . . 82

5.10 (a) Poisson ratio ($\sigma$) of $CH_4$. The (△) are from Ref. [139]. (b) Debye temperature of solid $CH_4$ (●). Compared with results (△) from Ref. [16] and (◇) Debye temperature of solid argon from Ref. [141] and (+) Ref. [142]. The dashed line is positioned as in Fig. 5.3. . . . . . . . . . . . . . 83

5.11 The lattice specific heat of $CH_4$ (●). Compared with $C_v$ of argon (- - -) and krypton (- · · - - ·) from Ref. [143, 144, 145]. The solid line is positioned at 3R. . . . . . . . . . . . . . . . . . . . . . . . . . . . . . . . 85

5.12 The Grüneisen parameter of $CH_4$. The dashed line is positioned as in Fig. 5.3. . . . . . . . . . . . . . . . . . . . . . . . . . . . . . . . . . 86

5.13 Rotational specific heat of $CH_4$ as a function of temperature. (- · · - - ·) line is positioned at $\frac{3}{2}$R. The dashed line is positioned as in Fig. 5.3. . . . 86

6.1 Frequency shifts in $CD_4$ as a function of temperature. The symbols show measured shifts as a function of angle $\phi$. Solid and dot-dashed curves are obtained from the best-fit elastic constants at each temperature. . . . . . 91

6.2 Frequency shifts in $CD_4$ - III versus rotational angle $\phi$ at T=18 K. The solid curves are for the symmetry classes $4mm$, 422, $\bar{4}2m$ and $4/mmm$. The dotted curves are for classes 4, $\bar{4}$, $4/m$. . . . . . . . . . . . . . . . . 92

6.3 Elastic constants $C_{11}$ (●) and $C_{33}$ (□) of $CD_4$ as a function of temperature. The error bars shown represent the standard deviation in the best fit parameters and uncertainties in the frequency shift and crystal orientation. The dashed lines are positioned at phase transition temperatures of $T_{c1}$=27.1 K and $T_{c2}$=22.1 K . . . . . . . . . . . . . . . . . . . . 95

6.4 Elastic constants $C_{12}$ (●) and $C_{13}$ (□) of $CD_4$ as a function of temperature. The error bars shown are as in Fig. 6.3. The dashed lines are positioned as in Fig. 6.3. . . . . . . . . . . . . . . . . . . . . . . . . . . . 96

6.5 Elastic constants $C_{44}$ (●) and $C_{66}$ (□) of $CD_4$ as a function of temperature. The error bars shown are as in Fig. 6.3. The dashed lines are positioned as in Fig. 6.3. . . . . . . . . . . . . . . . . . . . . . . . . . . . 97

6.6 Elastic constants of $CD_4$ as a function of temperature in phases I and II. The combinations correspond to the longitudinal and two transverse modes. $\frac{1}{2}(C_{11}$-$C_{12})$ and $C_{44}$ also correspond to the shear moduli in cubic system. The error bars shown are from the errors in elastic constants as in Fig. 6.3, 6.4 and 6.5. The dashed lines are positioned as in Fig. 6.3. . 99

6.7 Elastic moduli of $CD_4$ as a function of temperature. The error bars shown are from the errors in elastic constants as in Fig. 6.6. The dashed lines are positioned as in Fig. 6.3. . . . . . . . . . . . . . . . . . . . . . . . 100

6.8 (a) Anisotropy factor and (b) violation of Cauchy relation of $CD_4$ as a function of temperature. The dashed lines are positioned as in Fig. 6.3. . 101

6.9 Acoustic velocities of $CD_4$ (in $ms^{-1}$) in high symmetry planes in phases I and II. (a) and (b) are at 88.2 K (phase II). (c) and (d) at 25 K (phase II). (a) and (c) are in the (100) plane, (b) and (d) are in the (110) plane. 102

6.10 Acoustic velocities of $CD_4$ (in $ms^{-1}$ in phase III at 18 K. (a) is in the (100) plane and (b) is in the (110) plane. . . . . . . . . . . . . . . . . . . . . . 103

6.11 (a) Poisson ratio ($\sigma$) of $CD_4$ as a function of temperature. (b) Debye temperature of solid $CD_4$ (●). Compared with results (△) from Ref. [17]. The dashed lines are positioned as in Fig. 6.3 . . . . . . . . . . . . . . . 104

6.12 The lattice specific heat of $CD_4$ (●). Compared with $C_v$ of argon (· · ·), krypton (- · · · · ·) from Ref. [143, 144, 145] and $CH_4$ ( - - - -). The solid line is positioned at 3R. . . . . . . . . . . . . . . . . . . . . . . . . . . . 105

6.13 Rotational specific heat of $CD_4$ as a function of temperature. (- · · · · ·) line is positioned at $\frac{3}{2}$R. The dashed lines are positioned as in Fig. 6.3 . . 106

6.14 The Grüneisen parameter of $CD_4$. The dashed lines are positioned as in Fig. 6.3 . . . . . . . . . . . . . . . . . . . . . . . . . . . . . . . . . . . 106

B.1 The diffraction pattern of $CH_4$-I at 90 K. . . . . . . . . . . . . . . . . . . 125

B.2 The diffraction pattern of $CH_4$-I at 22 K after crystal has gone twice through the I-II phase transition. . . . . . . . . . . . . . . . . . . . . . . . 126

B.3 The diffraction pattern of $CD_4$-I at 88.2 K. . . . . . . . . . . . . . . . . . 127

B.4 The diffraction pattern of $CD_4$-II at 25 K. . . . . . . . . . . . . . . . . . 128

B.5 Representative Brillouin spectra of $CD_4$ in phases I (a) and III (b). The Rayleigh peaks are labeled $R_i$, longitudinal $L_i$, where $i$ is the number of corresponding Rayleigh and longitudinal peak. Transverse modes are labeled $T_{(s,f)i}$ where $s$,$f$ stand for slow and fast transverse modes and $i$ shows the Rayleigh peak to which a given transverse peak belongs. . . . . 129

## List of Tables

1.1 Physical properties of methane and heavy methane. . . . . . . . . . . . 6

1.2 Comparison of experimental and theoretical values of elastic constants (kbar) of $CH_4$ and $CD_4$. . . . . . . . . . . . . . . . . . . . . . . . . . 9

1.3 Ratios of sound velocities in high symmetry directions of the rare gas solids compared with those for orientationally disordered crystals. . . . . . . . . 9

1.4 Elastic properties of the RGS and orientationally disordered crystals. B is the bulk modulus in kbar, A is the anisotropy factor and $\delta$ is the measure of the violation of the Cauchy relation. . . . . . . . . . . . . . . . . . . . . 11

1.5 Phase transition temperatures of methane and its deuterated species. . . 11

4.1 Fundamental frequencies[1] of gaseous $CH_4$ and $CD_4$. Adapted from Ref. [117]. . . . . . . . . . . . . . . . . . . . . . . . . . . . . . . . 54

5.1 Elastic constants of $CH_4$ in phase I and II in kbars. Temperatures are accurate to within ±0.2 K. . . . . . . . . . . . . . . . . . . . . . . . . 72

6.1 Density and refractive Indices of $CH_4$ and $CD_4$ . . . . . . . . . . . . . . . 88

6.2 Elastic constants of $CD_4$ in phase I, II and III in kbars. Temperatures are accurate to within ±0.2 K. . . . . . . . . . . . . . . . . . . . . . . . . 94

7.1 Ratios of sound velocities in high symmetry directions of the rare gas solids compared with $CH_4$ and $CD_4$ at different temperatures . . . . . . . . . . 108

A.1 Brillouin scattering data for $CH_4$-I at 90 K, $\theta$=85.56$^0$, $\chi$=201.90$^0$. . . . . 122

A.2 Brillouin scattering data for $CH_4$-II at 17.3 K, $\theta$=99.37$^0$, $\chi$=115.83$^0$. . . . 122

A.3 Brillouin scattering data for $CD_4$-I at 88.2 K, $\theta$=58.91$^0$, $\chi$=28.18$^0$. . . . . 123

A.4 Brillouin scattering data for $CD_4$-II at 32.0 K, $\theta$=135.23$^0$, $\chi$=113.80$^0$. . . 123

A.5 Brillouin scattering data for $CD_4$-III at K, $\theta$=135.23$^0$, $\chi$=113.80$^0$. . . . . 124

# Chapter 1

# Introduction

## 1.1 Noble Gases and Methane

The discovery of helium by Janssen and Lockyer in 1868 and argon by Lord Rayleigh and W. Ramsay [1] later ultimately created a new field of interest in physics - namely, rare gas solids (RGS). These solids have been, and still are, used in a wide range of experiments, for molecular dynamic simulations and for testing the predictions of lattice dynamics theories. In many respects the inert gases form the simplest crystals known. The crystals are composed of atoms with completely filled outermost shells and which have spherically symmetric distributions of electronic charge. These crystals all have face-centered cubic (fcc) structure with the exception of $He^3$ and $He^4$ (which also have fcc structure at higher pressures [2]).

The RGS were among the first solid materials intensively studied but, despite the progress made in the understanding of properties of the RGS, a unified and reliable theory of them is still to come. At the same time, theoretical and experimental research on more complex systems such as molecular crystals is moving ahead. The molecular crystals are much more complicated systems than the RGS. Among them hydrogen and methane are distinguishable as special cases.

Hydrogen, the "simplest" element, the first entry in the Periodic Table and the most abundant element in the solar system became the most common compound in the condensed-matter physics research. After Wigner and Huntington predicted in 1935

[3] that solid molecular hydrogen would dissociate to form a monatomic metallic solid under a pressure of 25 GPa a lot of theoretical research was done which showed that such a dense metallic solid would possess some unusual properties. That in turn generated intense study and development of high pressure physics and as a result the creation of "metallic hydrogen" in the laboratory became one of the principal goals of condensed-matter studies (recently the measurements of electric conductivity of liquid hydrogen at pressures of $\approx$ 140 GPa [4] showed that hydrogen does become metallic).

Methane is another obvious candidate for the role of guinea-pig because with increasingly complicated crystal structure and intermolecular forces it still remains a relatively simple compound. Just like the RGS, methane forms a cubic fcc lattice with van der Waals interaction between molecules and it has a closed electron shell and almost spherically symmetric molecular structure. Because of their molecular simplicity and similarity to the rare gas solids, solid methane $CH_4$ and its deuterated compounds $CH_xD_{4-x}$ fueled theoretical and experimental interest in recent times. These crystals are also of interest because they are orientationally disordered. In most crystals, the positions and orientations of the molecules are ordered. In orientationally disordered crystals, molecules are in positional order with orientational disorder. Orientationally disordered crystals are, in some sense, like liquid crystals with the difference that, in the latter case, there is orientational order with positional disorder in liquid crystals (See Fig. 1.1).

The idea of molecules in a crystal rotating around one or more axes was introduced in 1923 by Simon and von Simson [5] who studied the crystal structure of the fcc phase of hydrogen chloride. Then Timmermans [6, 7] noticed that certain organic compounds, although in the solid state, have relatively high vapor pressure and melting points, and were soft and plastic. He attributed these characteristics to the molecular shape which he called "globular". The molecules actually have either tetrahedral symmetry or spherical or ellipsoidal. He called these solids "plastic crystals". Timmermans supposed that in

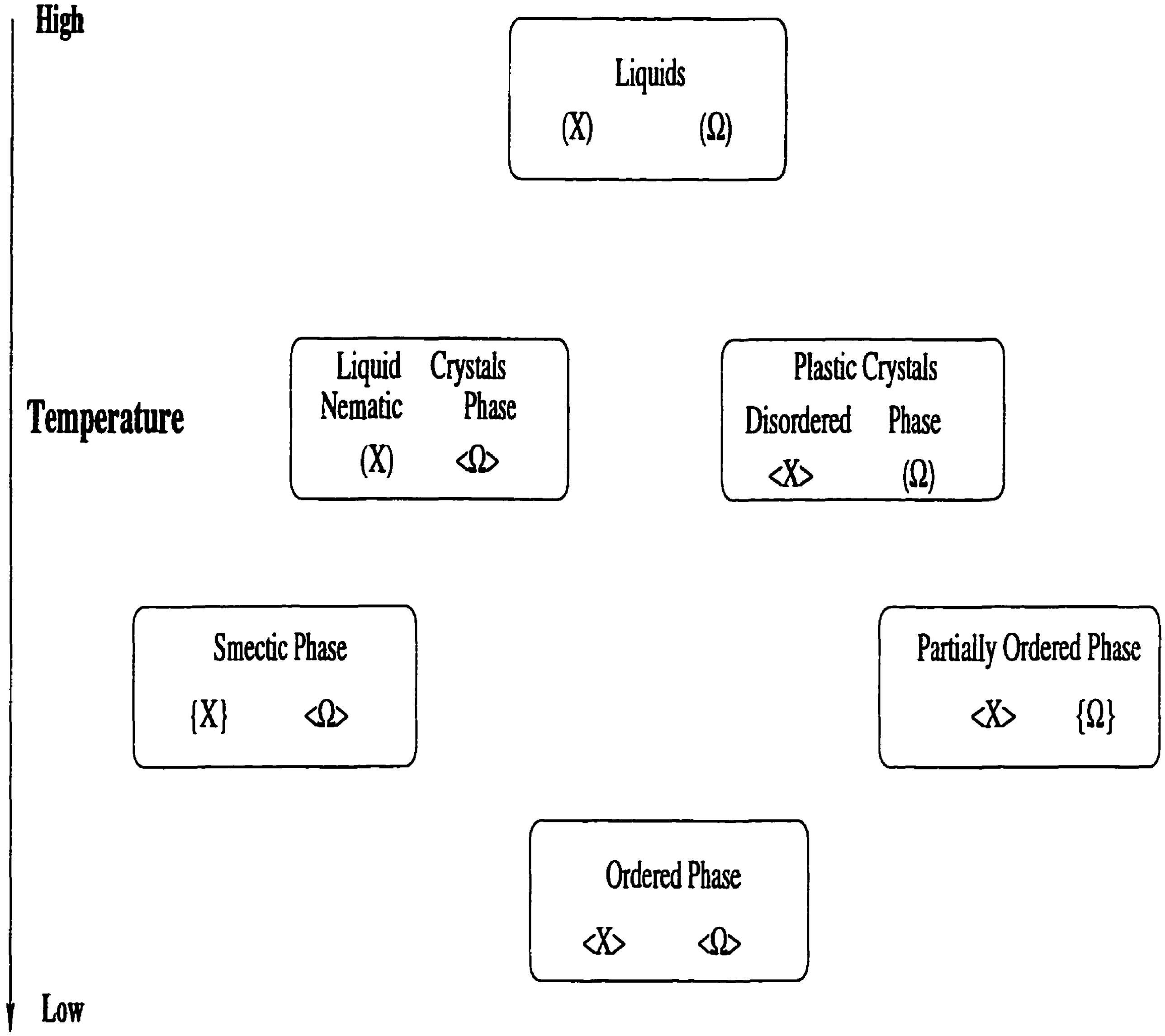
High
Temperature
Low
Liquids
(X) (Ω)
Liquid Crystals
Nematic Phase
(X) <Ω>
Plastic Crystals
Disordered Phase
<X> (Ω)
Smectic Phase
{X} <Ω>
Partially Ordered Phase
<X> {Ω}
Ordered Phase
<X> <Ω>

Figure 1.1: The comparison of liquid and disordered crystals. X is position and Ω orientation, < .. > denotes complete order, {..} partial order and (..) complete disorder.

the plastic phase the molecules are in rotational motion.

The plastic crystals are commonly of cubic symmetry and below some phase transition temperature they transform to crystals with lower symmetry. Later, Zernike [8] noticed that the transition in such crystals could be understood as a transition from an orientationally disordered state to an orientationally ordered state. Although the plastic-crystalline state itself has a special interest as an unusual state of the solid matter, its relationship with the other states, stable and metastable, is of interest as well.

## 1.2 Molecules of Methane and Interaction Between Them

Methane, $CH_4$, is one of the simplest of all organic compounds. It is the major constituent (up to 97%) of natural gas found on earth. It also is a significant hydrocarbon constituent of several planetary bodies in the solar system. Condensed $CH_4$ (possibly crystalline) has been identified on Pluto [9] and Neptune's moon Triton [10]. Condensed $CH_4$ is expected to exist on Uranus [11] and Neptune [12].

The molecule of methane consists of an atom of carbon (C) and four atoms of hydrogen (H). Carbon has two unpaired electrons in the *2p* shell and, in order to combine with four hydrogens, carbon provides one of its *2s* electrons to the *2p* shell. Carbon becomes bonded to hydrogen using 3 *2p* electrons and one *2s* electron. All these bonds are equivalent to each other and are directed to the corners of a tetrahedron as in Fig. 1.2. Each carbon-hydrogen bond has the same length (1.09 Å) and the angle between any two C-H bond is $109.5^0$. The symmetry of the $CH_4$ molecule is $\bar{4}3m$ ($T_d$). Because the molecule is highly symmetrical the dipole moment of the methane molecule equals zero. Some of the physical characteristics of $CH_4/CD_4$ are shown in the Table 1.1.

Methane, at room temperature and under atmospheric pressure, is a gas which liquefies at 111.5 K into a colorless liquid of density $\sim$0.485 g/cm$^3$ . As for almost all orientationally disordered crystals, methane is soft and plastic. It solidifies at 90.67 K into a transparent jelly like solid of fcc structure. How do methane molecules form a crystal if they are neutral? Let us look at the rare gas solids made up from inert gases like Ar or Ne. If the charge distributions of the atoms were rigid there would not be any interaction between them and the RGS would not exist. But, although the average dipole moment is zero at any instant, there may be a transient electric dipole moment because of the motion of electrons. If this dipole moment is $p_1$ it will create an electric field $E = 2p_1/R^3$ at the center of the second atom which is distance R away. This field will induce an instantaneous dipole moment $p_2=\alpha E=2\alpha p_1/R^3$ (where $\alpha$ is polarizability) in the second atom. The potential energy of these two interacting dipole moments is

$$U(R) = -\mathbf{p_2 E} \approx \frac{-p_1 p_2}{R^3} \approx \frac{-\alpha p_1^2}{R^6} = -\frac{C}{R^6} \tag{1.1}$$

These very weak attractive forces acting between the atoms are called **van der Waals** or **fluctuating dipole** forces. If the atoms are brought close enough to each other their charge distributions will eventually overlap. The resulting potential will be repulsive, mostly because of the Pauli exclusion principle, and it is very well fitted with an empirical repulsive potential of the form $B/R^{12}$, where B, and C from Eq. 1.1, are empirical parameters determined from measurements. The total potential energy of two atoms is consequently,

$$U(R) = 4\epsilon[(\frac{\sigma}{R})^{12} - (\frac{\sigma}{R})^6] \tag{1.2}$$

where $\epsilon$ and $\sigma$ are the parameters, with $4\epsilon\sigma^6$ =C and $4\epsilon\sigma^{12}$ = B. This semiempirical potential giving the potential energy between two neutral atoms is called the **Lennard-Jones** potential.

For a more precise treatment of molecular solids we have to consider some other effects of higher order. In methane we need somehow to incorporate the interaction between the

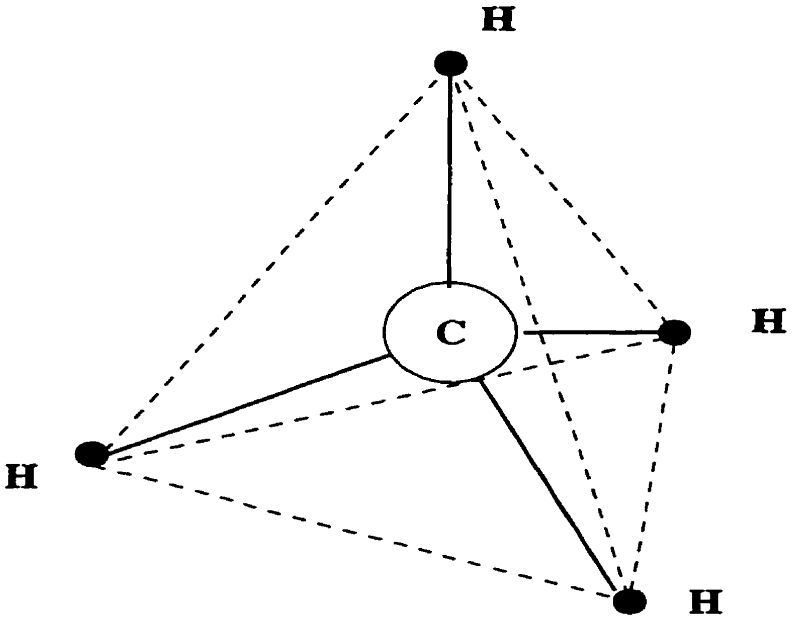

Figure 1.2: Molecule of methane (schematic)

Table 1.1: Physical properties of methane and heavy methane.

| | $CH_4$ | Ref. | $CD_4$ | Ref. |
|---|---|---|---|---|
| Molecular weight (g) | 16.043 | [13] | 20.045 | [13] |
| Triple point temp., K | 90.68 | [14] | 89.78 | [14] |
| Triple point press., Torr | 88.10 | [15] | 79.51 | [14] |
| Density (trip. p.) | 0.489 | [16] | 0.616 | [17] |
| Lattice constant, Å (trip. pt.) | 6.014 | [16] | 6.002 | [17] |
| Refractive index (trip. pt.) | 1.323 | [18] | 1.321 | [18] |
| Near-neighbor distance a, Å | 4.2568 | [19] | 4.2336 | [20] |

rotating molecules which are not perfectly spherical; but in the first approximation the Lennard-Jones potential describes molecular crystals, including methane, very well.

## 1.3 Elastic Properties of Methane

One of the first investigations of solid methane was carried out by Clusius [21] in 1929 when he discovered the phase transition in $CH_4$ by measuring the specific heat of solid methane. He observed a $\lambda$-type singularity at 20.5 K. Since then methane and the whole family of its deuterated species $CH_xD_{4-x}$ in all three states are under the scrutiny of physicists and chemists all over the world. Much effort was made to understand the properties of such systems at low temperatures and, particularly, around their phase transitions.

Methane and its deuterated species have been under investigation in spectroscopic [22-35], ultrasonic [36], calorimetric [14], neutron scattering [37-42] and X-ray [16,17,19,20,43-46] experiments. Also, there was a series of theoretical papers on methane [47-58] and molecular dynamics stimulations [59]. The experiments yielded important information about the phase transition and attempts were made to describe both phases of methane at low temperature. The main problem in studying methane experimentally at low temperatures is obtaining the sample. Phase II does not have boundaries with the liquid and the only path which is available at the low temperatures is through the phase I. This fact imposes quite a few constraints on the ability to conduct the experiments because, after cooling the crystal for a few tens of degrees through the phase transition, the most likely result will be a polycrystalline sample under a lot of mechanical strain. For some types of experiments such as thermodynamic measurements of specific heat it is rather unimportant whether the specimen is a single crystal or polycrystalline. On the other hand some measurements, for example diffusion, mechanical strength, x-ray diffraction and thermal conductivity are extremely sensitive to the presence of crystal defects and for these types of experiments high quality single crystals may be required. And if we want to measure the anisotropic properties, such as elastic constants, single and unstrained crystals become necessary.

Due to the difficulties in growing single crystals of the methane family within optical setups, only a few experiments on the elastic properties of heavy and normal methane have been published [18, 35, 40]. There are no sufficient data on the elastic properties of deuterated methane and there are no consistent values for the elastic constants of $CH_4$ and $CD_4$ over a wide temperature range. The elastic constants are important properties of crystals and they can be used to determine the phase diagrams and the order of transitions. They measure the stiffness of a crystal and are generally dependent on changes in molecular orientations. When the elastic constants are known such important thermodynamic properties as Debye temperature, Grüneisen parameter and specific heat can be calculated, and the equation of state can be deduced.

In contrast to the rare gas solids, for which good agreement between experimental and calculated values of elastic constants has been shown [60-71], there are difficulties in dealing with molecular solids such as methane. For krypton and argon, elastic constants have been determined and the phonon dispersion curves along high-symmetry directions have been measured [72, 71] to be in good agreement with theoretical calculations [66]. Some available values of elastic constants obtained by different techniques for $CH_4$ and $CD_4$ are given in Table 1.2.

Table 1.2: Comparison of experimental and theoretical values of elastic constants (kbar) of $CH_4$ and $CD_4$.

| $CH_4$ | T,K | $C_{11}$ | $C_{12}$ | $C_{44}$ | Ref. |
|---|---|---|---|---|---|
| Brillouin spectra | 90.4 | 19.57±0.30 | 14.46±0.20 | 9.20±0.15 | [18] |
| Molecular dynamics | 91.0 | 16.40±1.00 | 13.60±1.00 | 6.00±0.30 | [59] |
| Brillouin spectra[1] | 300 | 10 - 25 | 8 - 23 | 4 - 7 | [35] |
| $CD_4$ | | | | | |
| Brillouin spectra | 89.2 | 20.04±0.30 | 15.00±0.24 | 9.15±0.15 | [18] |
| Neutron scatt. | 32.5 | 30.80±2.00 | 21.40±2.40 | 15.8±0.60 | [40] |
| Born-von Karman | 32.5 | 34.10 | 26.8 | 14.20 | [40] |
| Lennard-Jones | 34.5 | 30.70 | 16.40 | 18.6 | [37] |
| Neutron scatt. | 34.5 | 32.80 | 23.90 | 14.9 | [37] |

Table 1.3: Ratios of sound velocities in high symmetry directions of the rare gas solids compared with those for orientationally disordered crystals.

| Crystal | T,K | <100> | <111> | <110> | <110> | Ref. |
|---|---|---|---|---|---|---|
| | | $V_l/V_t$ | $V_l/V_t$ | $V_l/V_{t1}$ | $V_l/V_{t2}$ | |
| Ar | 80.0 | 1.46 | 2.27 | 1.66 | 2.75 | [61] |
| Ne | 24.0 | 1.40 | 2.20 | 1.61 | 2.66 | [73] |
| Kr | 115.6 | 1.45 | 2.26 | 1.66 | 2.73 | [62] |
| Xe | 160.0 | 1.44 | 2.24 | 1.65 | 2.71 | [60] |
| $CCl_4$-(Ia) | 244.1 | 1.79 | 3.07 | 2.01 | 4.70 | [74] |
| $CBr_4$-I | 333.0 | 1.62 | 2.65 | 1.83 | 3.54 | [75] |
| $CH_4$-I | 90.4 | 1.46 | 2.44 | 1.69 | 3.20 | [18] |
| $CD_4$-I | 89.2 | 1.48 | 2.47 | 1.71 | 3.25 | [18] |

---

[1] The values of elastic constants are in GPa. Pressure was varied from 1 GPa to 5 GPa.

There are not many theoretical treatments of lattice dynamics and elastic properties of methane and generally they are based on the use of atom-atom potentials. For $CH_4$, the molecular dynamics simulation of Bounds *et al.* [59] yields values of elastic constants which are much smaller than the ones obtained by Brillouin spectroscopy [18]. For $CD_4$, the use of a Lennard-Jones potential [37], which reproduced thermophysical data, failed to give good agreement with neutron scattering experiments at 34.5 [37] and 32.5 K [40]. It also did not show the observed inequality $C_{11} > C_{12} > C_{44}$. The Born-von Karman calculations of Stirling *et al.* [40], based on harmonic force-constant models with nearest neighbor interactions between point masses, also gave poor agreement with the experimental results.

All these disagreements could be attributed to rotation-translation (RT) coupling in solid methane. RT coupling is the interaction between center of mass displacements and large amplitude orientational motion that may occur in molecular crystals or crystals with molecular ions, and results in a possible change of orientational order. It arises from terms in the Hamiltonian in which the orientational dependence of the potential of a molecule changes as a result of relative displacement of the center of mass of pairs of molecules.

In Tables 1.3 and 1.4 ratios of sound velocities in high symmetry directions and anisotropy factor (A) and bulk moduli (B) of the rare gas solids [72] are compared with those for orientationally disordered (OD) crystals of molecular solids. We can see that all the ratios of the sound velocities are the same to within a few percent, with the exception of $V_l/V_t$ in the <110> direction for OD crystals where $V_l/V_t$ is higher by $\sim 25\%$ in $CH_4$, $CD_4$, $CBr_4$ and enormously high in $CCl_4$ which is a fascinating substance in respect of RT by itself. This anomaly is due to a low value of $V_t$ in the <110> direction and sometimes is called "transverse mode softening". A similar comment applies to the anisotropy factor which is $\sim 30\%$ larger in OD crystals than in RGS.

Table 1.4: Elastic properties of the RGS and orientationally disordered crystals. B is the bulk modulus in kbar, A is the anisotropy factor and $\delta$ is the measure of the violation of the Cauchy relation.

| Crystal | T (K) | B | A | $\delta$ | Ref. |
|---|---|---|---|---|---|
| Ne | 24.0 | 8.77 | 2.74 | 0.17 | [73] |
| Ar | 80.0 | 18.3 | 2.74 | 0.28 | [61] |
| Kr | 115.0 | 20.3 | 2.70 | 0.26 | [62] |
| Xe | 160.0 | 22.6 | 2.74 | 0.22 | [60] |
| $CCl_4$-(Ia) | 244.1 | 33.0 | 3.48 | 0.64 | [74] |
| $CBr_4$-I | 333.0 | 36.5 | 3.73 | 0.52 | [75] |
| $CH_4$-I | 90.4 | 16.16 | 3.60 | 0.36 | [18] |
| $CD_4$-I | 89.2 | 16.68 | 3.63 | 0.39 | [18] |

Table 1.5: Phase transition temperatures of methane and its deuterated species.

| Species | Phase Transition Temperature T (K) | | |
|---|---|---|---|
| | liquid ↔ I | I ↔ II | II ↔ III |
| $CH_4$ | 90.67 | 20.5 | - |
| $CH_3D$ | 90.41 | 23.1 | 16.1 |
| $CH_2D_2$ | 90.17 | 24.9 | 19.1 |
| $CHD_3$ | 89.96 | 26.0 | 20.9 |
| $CD_4$ | 89.78 | 27.1 | 22.1 |

Most recently, an effort to shed some light on RT coupling was undertaken by Lynden-Bell and Michel [76]. They have shown that RT coupling is caused by the changes in orientational potential felt by a molecule due to its own motion or the motion of nearby molecules. The amount of this change depends on the actual strength and form of the intermolecular potential. They also showed that RT coupling in orientationally disordered crystals can influence phase transitions, affect the values of elastic constants, and change the appearance of phonon spectra. They pointed out, however, that there is a shortage of experimental data on orientationally disordered crystals at the present time.

## 1.4 Order-Disorder Phase Transitions

The presence of phase transitions in some substances at certain temperatures and pressures can be easily detected just by visual observation e.g. vapor, liquid water and ice. This is possible because of the big difference in physical properties between phases. In many other cases the presence of phase transitions can only be detected from very specific observation of subtle changes in physical quantities. Vast numbers of transitions between different phases of solids are hardly detectable by eye. The detection of a phase transition implies that there is at least one specific quantity which differs in both phases. This quantity can be any physical property e.g. density, refractive index, direction of the magnetic moments, conductivity, etc. In the case of liquid-vapor transition, a relevant quantity is the fluid/vapor density, the value of which normally depends continuously on temperature and pressure, whereas the transition point is defined by a discontinuous change of density.

Usually, in most phase transitions, there will be a thermodynamic quantity which will be discontinuous in two different phases. Ehrenfest [77] classified phase transitions depending on the relation between the thermodynamic quantity undergoing discontinuous change and the Gibbs free energy function. The transition is said to be of the same order as the derivatives of the Gibbs free energy which shows a discontinuous change at the transition point. From the Gibbs free energy:

$$G = E + PV - TS \tag{1.3}$$

we have

$$dG = VdP - SdT \tag{1.4}$$

The first derivatives of the free energy can be written as:

$$(\frac{\partial G}{\partial P})_T = V, \qquad (\frac{\partial G}{\partial T})_P = -S, \tag{1.5}$$

and the second as:

$$(\frac{\partial^2 G}{\partial P^2})_T = -V\beta, \qquad (\frac{\partial^2 G}{\partial P \partial T})_P = V\alpha, \qquad (\frac{\partial^2 G}{\partial T^2})_T = -\frac{C_p}{T}. \tag{1.6}$$

Here, $C_p$, $\alpha$ and $\beta$ are the heat capacity, volume thermal expansivity and compressibility, respectively. The transition in which a discontinuous change occurs in volume and entropy belongs to the first order, and those in which a discontinuous change occurs in the heat capacity, thermal expansivity and compressibility belong to the second order. Third and higher-order transitions will involve higher differential quantities. Several known phase transitions do not strictly belong in any such category. There is a superposition of second-order behavior in many first-order transitions and vice versa. It often happens that derivatives diverge at the phase transition and true second order phase transitions are in fact a rarity.

In the vapor-liquid transformation two phases can be considered as quantitatively distinct but qualitatively identical because beyond the critical point the two phases are indistinguishable. The concept of a qualitative difference between two phases can be defined as a difference of symmetry. The symmetry can be defined as a set of geometrical transformations which leaves the spatial configuration of the atoms or molecules in the given phase unchanged. In liquid or vapor, the distribution of molecules is isotropic and homogeneous and both phases have the same symmetry.

The transition between different symmetries, e.g. crystal and liquid, or different crystal modifications, cannot happen in a continuous manner such as for liquid and gas. In every state the solid has some symmetry and the symmetry is different in different phases. The transition between different crystal modifications usually involves a sudden rearrangement of the crystal lattice and the state of the body changes discontinuously. In this case the transition point can be defined not only by a discontinuous jump of a physical parameter but by the occurrence of symmetry change as well. The Landau theory of phase transitions [78] treats such kinds of phase transitions. It assumes the existence of symmetry change over the phase transition point. The theory establishes the mutual compatibility of the symmetry and physical characteristics of the transition: i.e. the relationship between symmetries of the two phases and the discontinuous behavior of physical characteristics across the transition.

The transitions with symmetry change are usually of the second order and they are almost always associated with some kind of (dis)ordering process. In general, there are two types of order/disorder associated with such phase transitions:

1) positional order/disorder, when center-of-mass translation is possible.

2) orientational order/disorder, when molecules can have different orientations.

A substance can be characterized by the amount of dis(order) pertaining to a particular phase of that substance. Landau introduced a quantitative characteristic, the *degree of ordering* $\eta$, which is zero in the disordered state and takes various positive or negative non-zero values in the states with various degrees of ordering. If the degree of ordering becomes zero discontinuously from some finite value, the transformation from an ordered to a disordered state will be a phase transition of the first order, but if the degree of ordering becomes zero continuously the phase transition will be of the second order. In almost all transitions of the second kind the more symmetrical phase corresponds to the higher temperature and the less symmetrical to the lower one.

Landau gave the mathematical description of a phase transition of the second kind and accounted for the continuous behavior of thermodynamic parameters such as volume and entropy, and discontinuous behavior of heat capacities and compressibility. It can be done by expanding the Gibbs free energy in terms of the degree of ordering, $\eta$. For small values of $\eta$ (near the transition), it may be written as :

$$G(P,T,\eta) = G_0 + \alpha\eta + A\eta^2 + B\eta^3 + C\eta^4 + ... \tag{1.7}$$

where the coefficients $\alpha$, A, B, C,... are functions of P and T. It can be shown [78] that if the states with $\eta$=0 and $\eta \neq 0$ are of different symmetry, the first-order term in the expansion $\alpha$ as well as all odd (in power of $\eta$) terms are equal to 0. Therefore

$$G(P,T,\eta) = G_0 + A\eta^2 + C\eta^4 + ... \tag{1.8}$$

For the temperature induced phase transition one can assume that pressure is constant and near the transition point, $T_c$, A can be written as

$$A(T) = a(T - T_c) \tag{1.9}$$

where

$$a = [\frac{\partial A}{\partial T}]_{T=T_c} \tag{1.10}$$

is a constant and C(T) is put equal to constant $C(T_c)$. The dependence of $\eta^2$ on temperature can be determined by way of the equilibrium condition $\partial G/\partial\eta$=0. The result from Eq. 1.8 is $\eta(A+2C\eta^2)=0$, therefore

$$\eta^2 = -\frac{A}{2C} = \frac{a(T_c - T)}{2C} \tag{1.11}$$

The entropy and heat capacity can now be derived from Eq. 1.8 and Eq. 1.11 simply by differentiating G with respect to $\eta$ and neglecting higher-order terms. The entropy S can be written as:

$$S = -(\frac{\partial G}{\partial T})_{P,\eta} = S_0 - \eta^2(\frac{\partial A}{\partial T})_{P,\eta} \tag{1.12}$$

where $S_0 = -\partial G_0/\partial T$. In the phase with higher symmetry $\eta=0$ and therefore $S=S_0$. In the phase with lower symmetry $\eta$ is described by Eq. 1.11 and entropy is

$$S = S_0 + \frac{A}{2C}\frac{\partial A}{\partial T} = S_0 + \frac{a^2}{2C}(T - T_c) \tag{1.13}$$

It can be seen that entropy continuously approaches $S_0$ as the temperature approaches $T_c$.

The specific heat at constant pressure is $C_p=T(\partial S/\partial T)_P$. Again, using Eq. 1.13, the specific heat in the phase with lower symmetry at the transition point can be written as:

$$C_p = C_{p0} + \frac{a^2 T_c}{2C} \tag{1.14}$$

where $C_{p0}=T_c(\partial S_0/\partial T)_P$. Because in the phase with higher symmetry $S=S_0$, the specific heat is $C_p=C_{p0}$. This means that during the phase transition the specific heat changes discontinuously from $C_{p0}$ to $C_{p0}+a^2T_c/2C$.

Other quantities, such as specific heat at constant volume and compressibility, can be shown to be discontinuous over the phase transition as well. Thus Landau's theory provides the basis for the Ehrenfest classification of the phase transitions.

## 1.5 Phases of $CH_4$ and $CD_4$

### 1.5.1 Methane

Among all methane species only the phase diagram of methane $CH_4$ (shown in Fig. 1.4) is known over a wide temperature and pressure range. Seven phases of methane have been reported, and the discovery of a new low-temperature high-pressure phase was recently reported [79]. Not much is known about the structures of the high pressure phases. Phase III was calculated to be tetragonal $P_{42}/mbc$ and completely ordered [80] but this contradicts the neutron elastic scattering experimental results of Ref. [41, 42]. The structures of all other high-pressure phases are unknown.

At low pressures methane has only two phases; all other deuterated species have three (see Table 1.5 and Figure 1.5). Methane $CH_4$ exists in an orientationally disordered plastic fcc phase I (space group $Fm3m$ [38, 81]) between its melting point of 90.67 K and the phase transition at $T_c$=20.5 K, where it changes to a partially ordered phase II (space group $Fm3c$ [38, 81]). In phase I the unit cell consists of four molecules which are orientationally disordered. Phase II is also fcc but in this phase some ordering is present: three out of four molecules are ordered with a local symmetry $\bar{4}2m$ and the remaining one is orientationally disordered with almost-free rotation. The lattice parameter changes from 6.013 Å to 5.876 Å in phase I (90 - 20.5 K) and from 5.870 Å to 5.858 Å in phase II (20.3 - 10 K) [19, 16].

### 1.5.2 Heavy Methane

The investigation of Press and Kollmar [39] using incoherent neutron scattering tends to confirm that phases I and II of $CH_4$ are isostructural with the corresponding phases of $CD_4$. A statistical mechanical theory of the phase structures in $CD_4$ has been published by James and Keenan [47] (theoretical interest in studying $CH_4/CD_4$ was sparked by

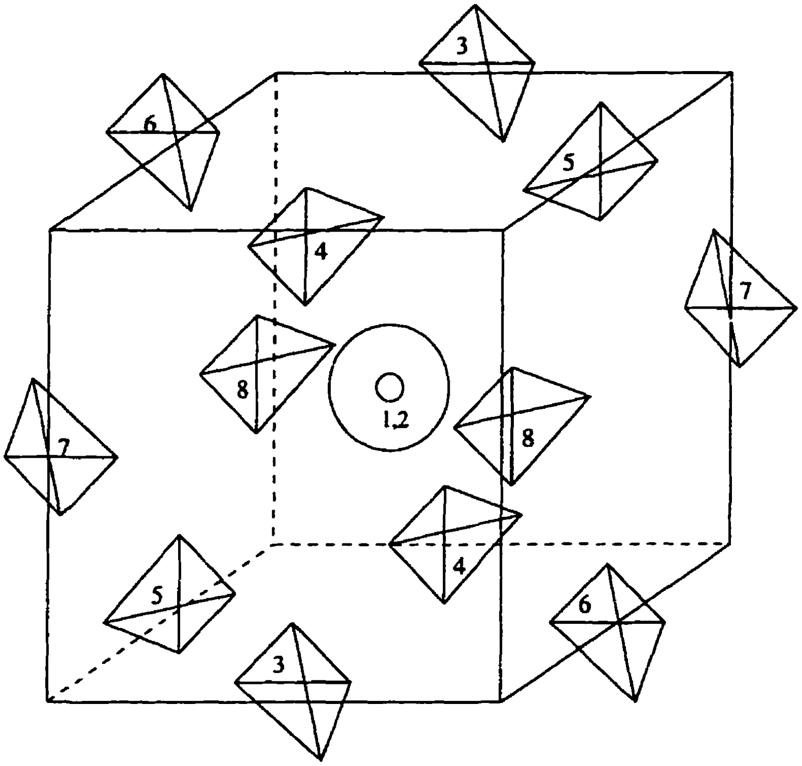

Figure 1.3: Arrangement of the eight sublattices in $CH_4$ and $CD_4$ in the phase II (space group $Fm\mathit{3}c$) with the disordered molecule in the symmetry center. Adapted from Ref. [81]

this famous paper). In this paper the classical treatment was employed to describe only solid $CD_4$ since quantum effects cannot be neglected in the description of $CH_4$. In the intermolecular potential energy function the interaction involving electrostatic dipoles and quadrupoles was found to vanish as a result of symmetry. The octupole-octupole interaction was taken as dominant, and higher-order interactions were neglected. The theory predicts that in phase I of $CD_4$ all molecules are orientationally disordered while in phase II one molecule out of four rotates freely. Phase III is predicted to be tetragonal with all molecules librating about equivalent equilibrium orientations. After selecting a value for the octupole moment which allows the theoretical value of the I-II transition temperature to be fit with the experimentally observed 27.1 K, the predicted lower

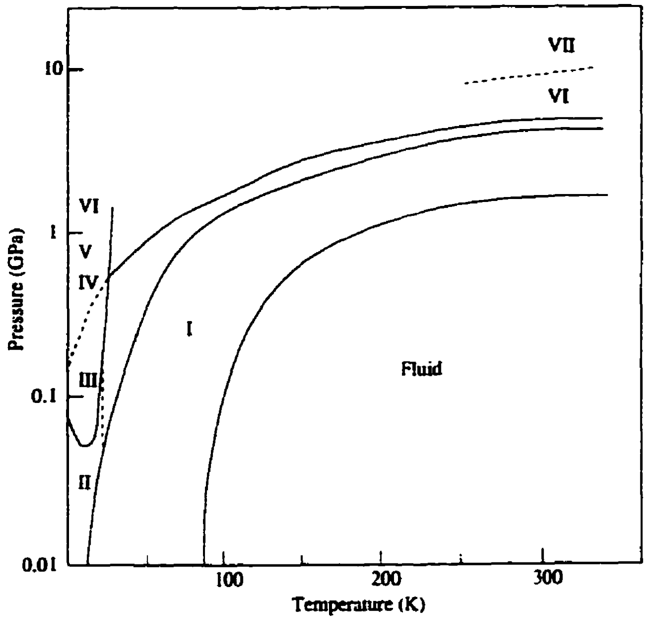

Figure 1.4: Proposed phase diagram of $CH_4$. Adapted from Ref. [31]

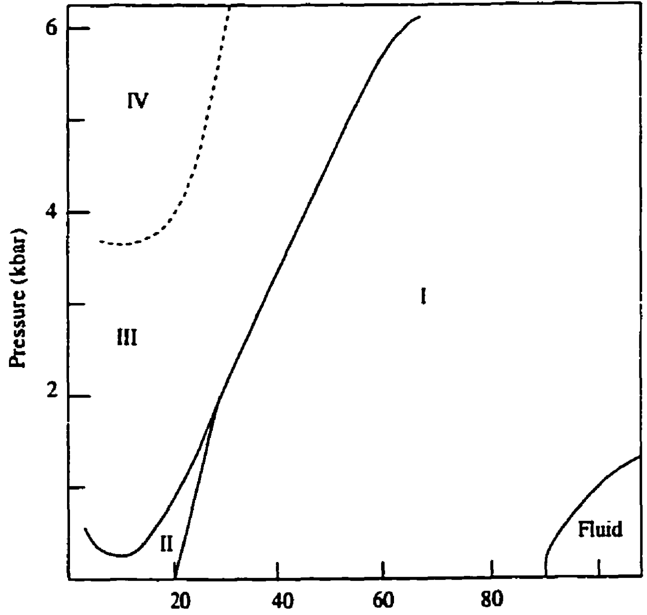

Figure 1.5: Phase diagram of $CH_4$ at low pressures and temperatures. Adapted from Ref. [57].

transition temperature is 24.4 K, and is to be compared with the observed 22.1 K. Phase I of deuteromethane extends between the melting point of 89.78 K and 27.1 K. Bol'shutkin [82] found that this phase has a fcc structure with four molecules per unit cell. Press *et al.* [81, 83], using coherent neutron scattering from powder samples, derived the space group as $Fm3m$. Phase II which exists between 22.1 and 27.1 K was found by Bol'shutkin [82] to be also fcc. The neutron investigation [81, 83] showed that the space group is $Fm3c$ and, as for $CH_4$, some ordering is present with six out of eight molecules ordered with a local symmetry $\bar{4}2m$.

The structure of the low temperature phase III which exists below 22.1 K was described [82] as face-centered tetragonal. The results of Ref. [81, 83] did not give a clear answer about the structure of phase III and suggested that it might be primitive cubic. The results of Ref. [84] show that at 4.2 K the cell is tetragonal with lattice parameters a=8.183 Å and c=11.671 Å and sixteen molecules per primitive cell. The fact that the structure of phase III most probably is not cubic was supported by optical measurements of Balic *et al.* [85, 86] who found that this phase is birefringent. Assuming that the structure is tetragonal, the observed values of the birefringence may be used to calculate the lattice parameters. They were found to be a=5.77 Å and c=5.84 Å. The most recent x-ray technique results [20, 17] suggest that this phase is tetragonal with lattice parameters changing from a=5.784 Å to 5.678 Å and c=5.865 Å to 5.861 Å across the temperature range of 22.1 to 5 K.

# Chapter 2

# Theory of Elasticity, Brillouin and Raman Spectroscopy

## 2.1 Theory of Elasticity

The elastic properties of solids are of interest for both basic research and technology. In technology the information is important for considerations of engineering design. In basic research, the elastic data can be combined with other physical measurements and provide a better understanding of the inter atomic/molecular forces in solid matter.

When external forces are applied to a solid, the dimensions and shape change in a manner which depends on the details of the applied forces. Applied forces change the relative arrangement of the particles in a solid, and move them from the positions of equilibrium which correspond to minima of potential energy. The resulting interatomic interactions give rise to forces within the body which tend to return the particles to their initial positions. These internal forces act against the external forces and in equilibrium the net force is zero. If the stress is within some limit which depends on the substance, then the movement of the particles and deformations are reversible. Such deformations are called elastic. When the external forces are removed an elastically deformed body returns to its initial state. The energy of elastic deformations stored in crystals can be measured by determining the work done by the external forces.

The macroscopic theory of elasticity ignores the discrete-particle structure of matter and considers the material as a continuum. An applied load can be then expressed as external force per unit area, or stress; and the deformation as fractional displacement, or

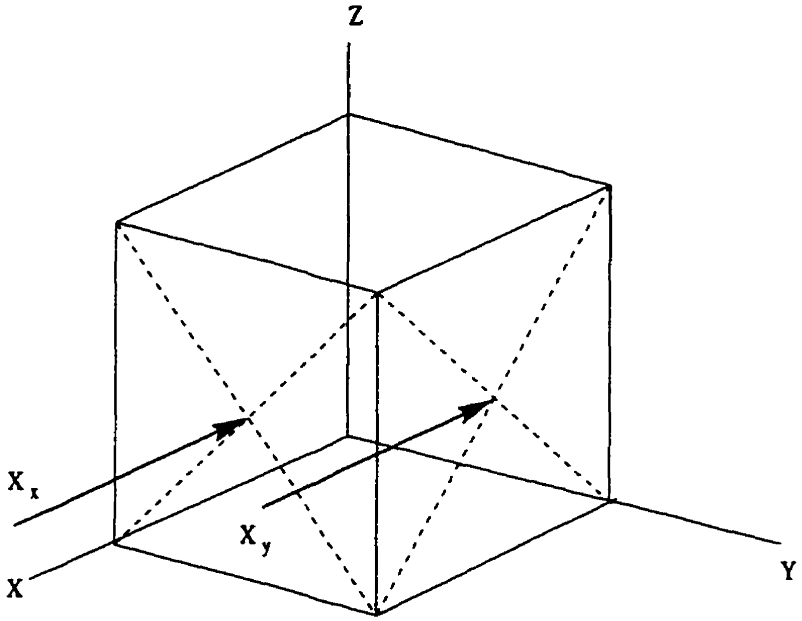

Figure 2.1: The forces acting on the faces of an elementary cube

strain. The quantitative description of the relation between strain and stress is given in many books [87-91] . Below, a brief description is given.

### 2.1.1 The Stress Tensor

If a small cube is subjected to external forces the stress can be defined as force acting on a unit area (see Fig. 2.1). It is assumed that the stress is homogeneous throughout the body, all parts of the body are in static equilibrium and there are no internal body-forces or body-torques.

Altogether there are nine components of stress $X_i$, $Y_i$ and $Z_i$, where $i$ is x, y or z. The capital letter shows the direction of force and subscript indicates the normal to the plane to which force is being applied. These components determine a tensor of second rank. The diagonal components $X_x$, $Y_y$ and $Z_z$ are perpendicular to the three faces of the cube and are compressive stresses. The other six are parallel to the faces and are shear stresses. In equilibrium, the moments of corresponding pairs are equal: $X_y$=$Y_x$,

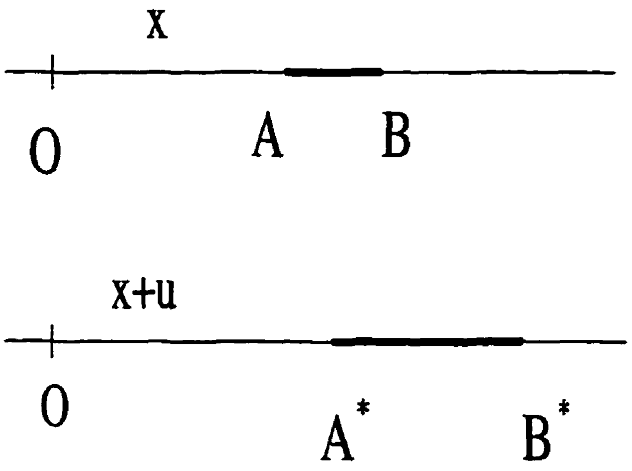

Figure 2.2: The transformation of a string under deformation

$Y_z$=$Z_y$, $Z_x$=$X_z$. It makes the tensor symmetrical and reduces the number of independent components to six. The tensor can be written as:

$$\sigma_{ij} = \begin{vmatrix} X_x & Y_x & Z_x \\ X_y & Y_y & Z_y \\ X_z & Y_z & Z_z \end{vmatrix} = \begin{vmatrix} \sigma_{11} & \sigma_{12} & \sigma_{13} \\ \sigma_{21} & \sigma_{22} & \sigma_{23} \\ \sigma_{31} & \sigma_{32} & \sigma_{33} \end{vmatrix}, \quad \sigma_{ij} = \sigma_{ji}$$

It can be proved that $\sigma_{ij} = \sigma_{ji}$ holds even when the stress is inhomogeneous, and when the body is not in static equilibrium and body-forces are present (see Ref. [88]).

### 2.1.2 The Strain Tensor

In order to define the strain let us consider a string which is being stretched (see Fig. 2.2). If an origin is O, then an arbitrary point A on the string moves to $A^*$. Let OA=x and $OA^*$=x+u and let a point B, close to A, move to $B^*$ and let AB=$\Delta$x. Then $A^*B^*$=$\Delta$x+$\Delta$u. The strain of section AB is defined as:

$$U = \frac{A^*B^* - AB}{AB} = \frac{\Delta u}{\Delta x} \tag{2.1}$$

and the strain at the point A is defined as:

$$U = \lim_{\Delta x \to 0} \frac{\Delta u}{\Delta x} = \frac{du}{dx}. \tag{2.2}$$

In two dimensions, the point A($x_1$,$x_2$) is transformed into the point A*($x_1$+$u_1$,$x_2$+$u_2$). Vector $u_i$ is the displacement of A. The strain at point A is defined as:

$$U_{11} = \frac{\partial u_1}{\partial x_1}; \quad U_{12} = \frac{\partial u_1}{\partial x_2}; \quad U_{21} = \frac{\partial u_2}{\partial x_1}; \quad U_{22} = \frac{\partial u_2}{\partial x_2}; \tag{2.3}$$

Similar to the one and two dimensional cases, the strain of a three dimensional body is defined as:

$$U_{ij} = \frac{\partial u_i}{\partial x_j}; \quad (i, j = 1, 2, 3) \tag{2.4}$$

The *strain tensor* $\epsilon_{ij}$ is defined as:

$$\epsilon_{ij} = \begin{vmatrix} \epsilon_{11} & \epsilon_{12} & \epsilon_{13} \\ \epsilon_{12} & \epsilon_{22} & \epsilon_{23} \\ \epsilon_{31} & \epsilon_{23} & \epsilon_{33} \end{vmatrix} = \begin{vmatrix} U_{11} & \frac{1}{2}(U_{12} + U_{21}) & \frac{1}{2}(U_{13} + U_{31}) \\ \frac{1}{2}(U_{12} + U_{21}) & U_{22} & \frac{1}{2}(U_{23} + U_{32}) \\ \frac{1}{2}(U_{13} + U_{31}) & \frac{1}{2}(U_{23} + U_{32}) & U_{33} \end{vmatrix}$$

or in short

$$\epsilon_{ij} = \frac{1}{2}(U_{ij} + U_{ji}) \tag{2.5}$$

The diagonal components of $\epsilon_{ij}$ are the tensile strains. Non-diagonal components are the shear strains.

### 2.1.3 Elastic Constants, Stress and Strain

The relation of the stress and strain tensors is given by the generalized Hooke's Law:

$$\sigma_{ij} = C_{ijkl}\epsilon_{kl} \tag{2.6}$$

where $C_{ijkl}$ is a tensor of fourth-order with 81 elements. The symmetry of the stress and strain tensor implies that $C_{ijkl}$ can have at most 36 independent elements. If we consider the change of energy of a small volume under homogeneous strain, for small deformations it could be written:

$$\Phi = \Phi(0) + [\frac{\partial\Phi}{\partial\epsilon_{ij}}]_0\epsilon_{ij} + \frac{1}{2}[\frac{\partial^2\Phi}{\partial\epsilon_{ij}\partial\epsilon_{kl}}]_0\epsilon_{ij}\epsilon_{kl} + ... \tag{2.7}$$

where $\Phi(0)$ is the internal energy in a state from which strain is measured. Assuming, that $\Phi(0)$ is at a relative minimum the first derivative in Eq. 2.7 is equal 0 and the energy of deformation is given by:

$$\Phi - \Phi(0) = \frac{1}{2}[\frac{\partial^2\Phi}{\partial\epsilon_{ij}\partial\epsilon_{kl}}]_0\epsilon_{ij}\epsilon_{kl} + O(\epsilon_{ij}^3) \tag{2.8}$$

If work is done to create some strain it means that the quadratic right side of Eq. 2.8 is positive and

$$[\frac{\partial^2\Phi}{\partial\epsilon_{ij}\partial\epsilon_{kl}}]_0 = [\frac{\partial^2\Phi}{\partial\epsilon_{kl}\partial\epsilon_{ij}}]_0 \tag{2.9}$$

The work which is done when the stress $\sigma_{ij}$ creates the strain $\epsilon_{ij}$ is equal to:

$$\triangle W = \frac{1}{2}\sigma_{ij}\epsilon_{ij} \tag{2.10}$$

and it is equal to the difference between $\Phi$ and $\Phi(0)$. The stress can be written as

$$\sigma_{ij} = [\frac{\partial^2\Phi}{\partial\epsilon_{ij}\partial\epsilon_{kl}}]_0\epsilon_{kl} \tag{2.11}$$

Comparing Eq. 2.6 and 2.9 it follows that

$$C_{ijkl} = [\frac{\partial^2\Phi}{\partial\epsilon_{ij}\partial\epsilon_{kl}}]_0 = C_{klij} \tag{2.12}$$

So, the tensor $C_{ijkl}$ has some more symmetry coming from the positive energy and it can be further reduced to "only" 21 independent elements. This tensor is called the *elastic constants* tensor.

The fundamental significance of the elastic constants lies in the fact that they appear as the second derivatives of the energy with respect to the strains.

## 2.2 Brillouin Scattering

At the end of the last century, Lord Rayleigh obtained the famous result that the intensity of the scattered light is inversely proportional to the fourth power of the frequency of the incident radiation (see Eq. 2.34) [92, 93]. Later, Brillouin [94] (and independently Mandelshtam [95]) having combined the Bragg diffraction condition with the concept of acoustic waves of thermal origin, arrived at the conclusion that the light scattered by the acoustic waves will be present along with the Rayleigh scattering but at different frequencies. The experimental confirmation came much later [96] owing to the experimental difficulties of detection and measurement of the Brillouin shifts which are $\sim$0.3-3.0 cm$^{-1}$ away from the Rayleigh line and extremely weak.

The invention of the laser in 60's gave impetus to Brillouin spectroscopy and a lot of work was done in liquids [97-102] and, despite the fact that it is much more difficult to conduct Brillouin experiments in many solids (because of the difficulties with the optical properties of crystals and high Rayleigh scattering), considerable progress in solids was made [60, 61, 62, 73, 103]. Most of the interest in solids centered on the measurements of the elasticity because Brillouin spectroscopy is almost a perfect tool to study the elastic properties: it does not require physical contact with the sample as in ultrasonic experiments and, unlike in neutron scattering it can be done in relatively small volumes. It has its limitations as well: the range of investigations is confined close to the center of Brillouin zone and it requires optically transparent media. At the present time, with the refinement of diamond anvil techniques and use of a tandem Fabry-Perot, the vast majority of the Brillouin experiments are done on the surface of opaque samples and at very high pressures.

Recently, a new technique which can successfully complement Brillouin scattering, was developed [104-108] . It is called laser-induced phonon spectroscopy (LISP). In this experiment an acoustic grating is formed in the sample as a result of constructive interference of two time-coincident pulses created from a single laser pulse. Then the grating is probed by the same, usually frequency doubled, delayed pulse. The delayed pulse is scattered off the acoustic grating and can be observed. The observation of this pulse permits the determination of frequency of the acoustic wave. The great advantage of this technique is the large signal to noise ratio (so that data can be collected in matter of seconds), and independency of refractive index. This technique seems to be ideally coupled with high-pressure experiments in a diamond anvil cell where extremely small size of the sample is one of the conditions. The elastic moduli of $\beta$-oxygen up to 9 GPa and sound velocities in methanol up to 31 GPa have been measured by this method [107]. But the number of experiments with LISP is not extensive and the limit of maximum pressure achievable with this technique is not known but believed to lie in the megabar region.

### 2.2.1 Acoustic Waves and Elastic Constants

In the theory of Brillouin scattering the molecular structure of the medium is completely ignored (because the wavelength of acoustic waves is much greater than the intermolecular distance). Here, let us consider the thermally generated fluctuations of density in a medium. Consider the medium as a number of layers as in Fig. 2.3(a). The sound waves can be represented by plane parallel regions of higher and lower densities as if the waves were stationary. One can thus expect an optical analogy with Bragg reflection.

Let monochromatic light of wavelength $\lambda$ be incident along ANR, and let RSB be the direction of the scattered light. The distance between the planes is d, which is the wavelength of the sound waves $\lambda_s$. For the geometry in Fig. 2.3(a) $\phi = \phi_i = \phi_s$, $\theta = \pi - 2\phi$. For constructive interference to occur (Fig. 2.3(a)) the path difference should be an integral multiple, m, of the optical wavelength $\lambda_i$ of the incident wave, where m is the order of interference. This path difference is equal to :

$$NR + RS = 2NR = 2nd\sin(90 - \phi_i) \tag{2.13}$$

where $n$ is refractive index of medium and $m\lambda_i = 2nd\sin(90 - \phi_i)$. For the $1^{st}$ order m=1 this becomes $\lambda_i = 2nd\sin(90 - \phi_i)$. Using a geometrical equality and expressing the frequency of sound waves and incident light as $V_s = \nu_s\lambda_s$ and $c=\nu_i\lambda_i$, respectively it can be written as

$$\lambda_i = \frac{c}{\nu_i} = 2nd\cos\phi_i = 2n\lambda_s\cos(\frac{\pi}{2} - \frac{\theta}{2}) = 2n\frac{V_s}{\nu_s}\sin(\frac{\theta}{2}) \tag{2.14}$$

And finally, by expressing the Brillouin shift as a function of the wavelength of the incident light, scattering angle and the velocity of the sound waves the *Brillouin equation* can be written as:

$$\triangle\,\nu = \pm\nu_s = \pm 2n\frac{V_s}{\lambda_i}\sin(\frac{\theta}{2}) \tag{2.15}$$

The implication of Eq. 2.15 is that the scattered radiation is a consequence of the Doppler effect of the acoustic wave on the incident optical wave, giving rise to a modified scattered optical wave which is called the Brillouin component.

In the quantum consideration of the Brillouin effect for long wavelength acoustic modes, $\omega_s$ is linear in $\mid \vec{q} \mid$ to a very good approximation. The dispersion relation is then,

$$\omega_s = V_s \mid \vec{q} \mid \tag{2.16}$$

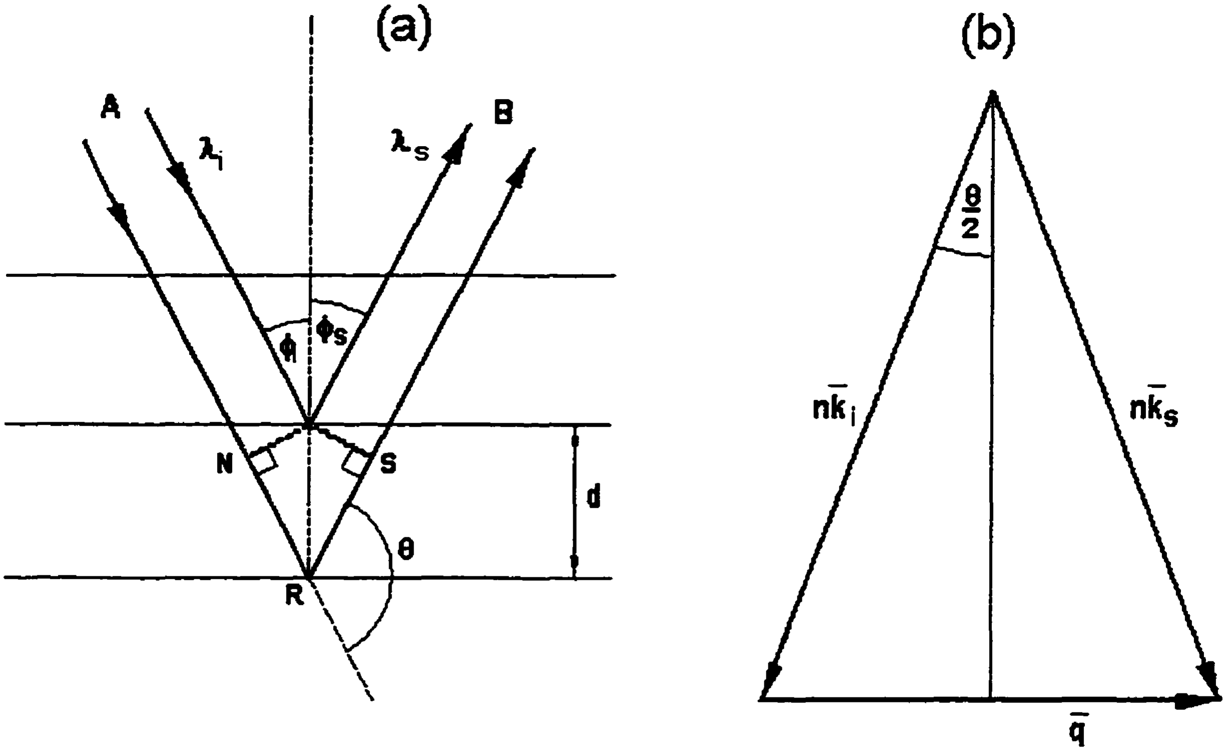
(a)
A
$\lambda_i$
$\lambda_s$
B
$\phi_i$
$\phi_s$
N
S
d
$\theta$
R
(b)
$\frac{\theta}{2}$
$n\bar{k}_i$
$n\bar{k}_s$
$\bar{q}$

Figure 2.3: Brillouin scattering: (a) wave picture (b) quantum picture

where $V_s$ is the velocity of one of the acoustic modes in the $\vec{q}$ direction. In the scattering process there is very little difference between the magnitude of the wavevector of the incident light, $k_i$ and that of the scattered light, $k_s$. This is because the typical phonon (acoustic wave) energy is much less than that of a typical photon.

Hence the triangle in Fig. 2.3(b) is nearly isosceles and it can be easily seen that

$$q = 2nk_i \sin(\frac{\theta}{2}), \tag{2.17}$$

where n is the index of refraction of the medium being probed and $\theta$ is the scattering angle. Substitution of 2.16 into 2.17 will yield the Brillouin equation.

In order to combine the elastic properties of media with the theory of Brillouin scattering the equation of motion is needed. The velocity of the propagating acoustic wave can be found by solving the equation of motion for a small volume of solid with density $\rho$. If all the forces (compressional and shear) are acting on the arbitrary volume element as in Fig. 2.1 the equation of motion for the x direction can be written:

$$\begin{aligned} -(\sigma_{11}dydz + \sigma_{12}dzdx + \sigma_{13}dxdy + [(\sigma_{11} + \frac{\partial\sigma_{11}}{\partial x}dx)dydz + \\ (\sigma_{12} + \frac{\partial\sigma_{12}}{\partial y}dy)dxdz + (\sigma_{13} + \frac{\partial\sigma_{13}}{\partial z}dz)dxdy)] \\ = \rho\frac{d^2u_1}{dt^2}dxdydz. \end{aligned} \tag{2.18}$$

This can be simplified to:

$$\frac{\partial\sigma_{11}}{\partial x_1} + \frac{\partial\sigma_{12}}{\partial x_2} + \frac{\partial\sigma_{13}}{\partial x_3} = \rho\frac{\partial^2 u_1}{\partial t^2}, \tag{2.19}$$

where $x_i$ are x, y and z. Similar equations can be written for the y and z directions. These equations may be written in concise form as:

$$\frac{\partial\sigma_{ij}}{\partial x_i} = \rho\ddot{u}_i. \tag{2.20}$$

When this is combined with the Hooke's Law Eq. 2.6 and the relation Eq. 2.5 the equation of motion becomes

$$\rho\ddot{u}_i = \frac{1}{2}C_{ijkl}[\frac{\partial^2 u_k}{\partial x_j\partial x_l} + \frac{\partial^2 u_l}{\partial x_j\partial x_k}]. \tag{2.21}$$

To solve the equation of motion 2.21 we seek plane wave solutions of the form

$$u(r,t) = u(q)\Pi(q)e^{i(\vec{q}\cdot\vec{r}-\omega t)} \tag{2.22}$$

where $\Pi(q)$ is unit polarization vector and $u(q)$ is the amplitude of the elastic wave which will propagate with wavevector q.

Substituting Eq. 2.22 into Eq. 2.21 and performing the necessary differentiations yields the secular equation

$$[C_{ijkl} - \rho V^2 \delta_{il}]\Pi(q) = 0 \tag{2.23}$$

and V is given by Eq. 2.16 for long wavelength acoustic waves. For nontrivial solutions it is necessary that

$$|C_{ijkl} - \rho V^2 \delta_{il}| = 0. \tag{2.24}$$

The determinant in Eq. 2.24 is known as the Christoffel determinant which relates the elastic constants to the acoustic velocity. This is a cubic equation for $\rho V^2$ which is extremely complicated for an arbitrary direction. The determinant was solved by Every [109] for waves traveling in arbitrary directions in most crystal structures. But the usual way of solving the equation is by numerical diagonalization of the determinant. In high symmetry directions the determinant becomes much less complex but in a real experiment the orientation of the crystal is not usually under complete control and it is not possible to choose the scattering vector in a high symmetry direction. Having measured the Brillouin shifts one can combine the Christoffel determinant with the Brillouin equation 2.15 and determine the elastic constants of the medium under investigation.

The polarization of the wave and its velocity depends only on the direction of q. In high symmetry directions e.g. $< 110 >$ the highest velocity mode is purely longitudinal, while the other two modes are purely transverse. In general the polarization is neither longitudinal nor transverse although the highest velocity mode is predominantly parallel to the wave propagation direction and it's usually called quasilongitudinal and two other modes are predominantly orthogonal to the direction of the wave propagation and called quasitransverse acoustic waves. It was discussed above that the $C_{ijkl}$ form a tensor of rank four but symmetry properties of the tensor reduce the number of independent elements from 81 to 21. The tensor may then be written in matrix form by reducing the number of subscripts from 4 to 2 using the standard notation of Voigt. In the case of cubic crystals, such as phases I and II of $CH_4$ and $CD_4$, the high symmetry of the lattice further reduces the number of elastic constants to three, namely $C_{11}$, $C_{12}$ and $C_{44}$ [110] - and the elastic constant matrix becomes:

$$\begin{pmatrix} C_{11} & C_{12} & C_{12} & 0 & 0 & 0 \\ C_{12} & C_{11} & C_{12} & 0 & 0 & 0 \\ C_{12} & C_{12} & C_{11} & 0 & 0 & 0 \\ 0 & 0 & 0 & C_{44} & 0 & 0 \\ 0 & 0 & 0 & 0 & C_{44} & 0 \\ 0 & 0 & 0 & 0 & 0 & C_{44} \end{pmatrix} \tag{2.25}$$

where for cubic crystals

$$\Gamma_{il} = \begin{cases} (C_{11} - C_{44})q_i^2 + q^2 C_{44} & i = l \\ (C_{12} + C_{44})q_i q_l & i \neq l \end{cases} \tag{2.26}$$

Explicitly then Eq. 2.26 becomes,

$$\begin{Vmatrix} (C_{11} - C_{44})q_1^2 + \lambda & (C_{12} + C_{44})q_1 q_2 & (C_{12} + C_{44})q_1 q_3 \\ (C_{12} + C_{44})q_2 q_1 & (C_{11} - C_{44})q_2^2 + \lambda & (C_{12} + C_{44})q_2 q_3 \\ (C_{12} + C_{44})q_3 q_1 & (C_{12} + C_{44})q_3 q_2 & (C_{11} - C_{44})q_3^2 + \lambda \end{Vmatrix} = 0 \tag{2.27}$$

where $\lambda = C_{44}q^2 - \rho V^2$

This equation has been solved analytically by Every [109] to yield:

$$\rho V_{q\mu}^2 = \frac{1}{3}C_1 + \frac{2}{3}C_2(1 - aS)^{\frac{1}{2}} \cos(\Psi + \frac{2}{3}\pi j) \tag{2.28}$$

where,

$$C_1 = C_{11} + 2C_{44}, \quad C_2 = C_{11} - C_{44}, \quad C_3 = \frac{K}{C_{11} - C_{44}}$$

$$K = C_{11} - C_{12} - 2C_{44}, \quad S = q_1^2 q_2^2 + q_2^2 q_3^2 + q_3^2 q_1^2, \quad Q = q_1^2 q_2^2 q_3^2 \tag{2.29}$$

$$\Psi = \frac{1}{3} \arccos[\frac{1 - \frac{3}{2} aS + bQ}{(1 - aS)^{\frac{3}{2}}}], \quad a = 3C_3(2 - C_3), \quad b = \frac{27}{2} C_3^2 (3 - 2C_3)$$

The index $j = 0,\ 1,\ 2$ and corresponds to $\mu = L, T_1$ and $T_2$ respectively, which are longitudinal and two transverse modes.

In the directions $< 100 >$, $< 110 >$ and $< 111 >$ Eq. 2.28 is considerably simplified and can easily be solved to give the following acoustic wave velocities in the high symmetry directions:

$< 100 >$

$$V_L = [\frac{C_{11}}{\rho}]^{\frac{1}{2}}, \quad V_{T_1, T_2} = [\frac{C_{44}}{\rho}]^{\frac{1}{2}}. \tag{2.30}$$

$< 110 >$

$$V_L = [\frac{C_{11} + C_{12} + 2C_{44}}{2\rho}]^{\frac{1}{2}}, \quad V_{T_1} = [\frac{C_{44}}{\rho}]^{\frac{1}{2}}, \quad V_{T_2} = [\frac{C_{11} - C_{12}}{2\rho}]^{\frac{1}{2}}. \tag{2.31}$$

$< 111 >$

$$V_L = [\frac{C_{11} + 2C_{12} + 4C_{44}}{3\rho}]^{\frac{1}{2}}, \quad V_{T_1, T_2} = [\frac{C_{11} - C_{12} + C_{44}}{3\rho}]^{\frac{1}{2}}. \tag{2.32}$$

As mentioned above, in the present experiment the orientation of each crystal was completely arbitrary and it was necessary to use numerical methods to solve the Christoffel determinant.

In a medium of tetragonal symmetry such as phase III of $CD_4$ the elastic matrix becomes more complicated than in the case of a cubic symmetry. A tetragonal system has two different classes of symmetry: lower symmetry classes such as $4,\bar{4}$ and $4/m$ have seven independent elastic constants and higher symmetry classes $\bar{4}2m$, $4mm$, 422 and $4/mmm$ have six. The elastic constants matrix for the lower symmetry classes is:

$$\begin{pmatrix} C_{11} & C_{12} & C_{13} & 0 & 0 & C_{16} \\ C_{12} & C_{11} & C_{13} & 0 & 0 & -C_{16} \\ C_{13} & C_{13} & C_{33} & 0 & 0 & 0 \\ 0 & 0 & 0 & C_{44} & 0 & 0 \\ 0 & 0 & 0 & 0 & C_{44} & 0 \\ C_{16} & -C_{16} & 0 & 0 & 0 & C_{66} \end{pmatrix} \tag{2.33}$$

The elastic constants matrix for the higher classes is essentially the same but the $C_{16}$ constant is zero.

## 2.3 Raman Scattering

Light scattering experiments have been carried out for more then one hundred years. Some of the earliest investigations were done by Tyndall [111]. He incorrectly concluded that both the polarization and blue color of light from the sky were caused by the scattering of sunlight by dust particles in the atmosphere.

Lord Rayleigh [92] examined the scattering of light by spherical particles of relative permittivity $k$ suspended in a medium of relative permittivity $k_0$. If the particle separation is greater than the wavelength, $\lambda$, of the incident light (so that the particles scatter independently of each other) and the particle radius is less than the wavelength, the intensity of scattered light is given by:

$$I_s = I\frac{9\pi^2 N v^2}{2\lambda^4 r^2}[\frac{k-k_0}{k+2k_0}]^2(1+\cos^2\phi) \tag{2.34}$$

where $I$ is the intensity of unpolarized incident light, $N$ is the number of scattering particles in volume $v$, $\phi$ is the angle through which the light is scattered, and $r$ is the distance to the point of observation. An important feature of this result is the $\lambda^{-4}$ dependence of the scattered light intensity, known as Rayleigh's law, which was also shown to be the same for scattering by molecules.

Further progress in understanding of the frequency dependence of the scattered light was made by Brillouin [94], who found that the spectrum of a fluid consists of a doublet, split symmetrically, around the frequency of incident light, arising from the scattering of light on the acoustic waves. This was first observed experimentally by Gross in 1930 [96].

The beginning of this century was characterized in physics by the development of the theory of quantum mechanics. And, of course, the quantum-mechanical theory of light scattering was developed as well. Smekal studied the scattering of light by a system with two quantized energy levels and predicted that [112] radiation scattered from molecules contains not only photons with the incident-photon frequency but also some with a changed frequency. These theoretical predictions, however, had no relation to the actual discoveries of Raman scattering which happened at the approximately same time. In India C.V. Raman and K.S. Krishnan, guided in their studies by the optical analog of Compton scattering, observed Raman shifts in liquids [113]. Also, the Raman shifts were observed in the USSR, where Landsberg and Mandelstam were studying the light scattering in crystals, looking for frequency shifts in scattered radiation as a result of the modulation of the incident light by the eigenfrequencies of the crystal [114, 115].

Since then, formidable progress in Raman studies has been made. The invention of the laser and improvement of detection techniques simplified the obtaining of Raman spectra and also led to discoveries of unknown effects such as the resonance Raman effect and stimulated Raman effect. Raman spectroscopy has developed into a prominent branch of molecular spectroscopy and its methods are widely used in the study of material composition and structure and in molecular spectral analysis.

Raman scattering is one of the processes resulting from the interaction of radiation with matter. A characteristic feature of Raman scattering is the change in the frequency of the scattered light. As distinct from luminescence, where the frequency of re-emitted radiation is also changed, in Raman scattering the system is not excited for any measurable length of time to a higher energy level. All excitations in the Raman scattering process are purely virtual states.

By now the Raman scattering in all three normal phases of matter is very well understood and documented [116-122] . The Raman scattering can be described using two different approaches: classical and quantum mechanical. In the classical approach the interaction between the light and matter (a crystal in our case) occurs via the polarizability of the scattering medium. The electric field of the incident light causes a shift of charge and induces a dipole moment $\mu$ proportional to the electric field intensity $\mathbf{E}$:

$$\mu = \alpha \mathbf{E} \tag{2.35}$$

The proportionality factor $\alpha$, known as the polarizability, is characteristic of the constituent molecules. The polarizability of a molecule is usually anisotropic, i.e. different for different directions in space. The variation of the polarizability with direction can be given most generally in the form of polarizability tensor:

$$\alpha_{ij} = \begin{vmatrix} \alpha_{xx} & \alpha_{xy} & \alpha_{xz} \\ \alpha_{yx} & \alpha_{yy} & \alpha_{yz} \\ \alpha_{zx} & \alpha_{zy} & \alpha_{zz} \end{vmatrix} \tag{2.36}$$

In Raman scattering the tensor of the polarizability derivative with respect to the vibrational normal coordinate Q, i.e.

$$\alpha' = \left(\frac{d\alpha}{dQ}\right). \tag{2.37}$$

is important because the intensity of the scattering depends on that tensor. If the electric field intensity, **E**, of the incident electromagnetic wave varies as

$$\mathbf{E} = \mathbf{E_0} \sin(2\pi\nu_0 t) \tag{2.38}$$

the induced dipole will be an oscillating dipole with frequency $\nu_0$. Substituting Eq. 2.38 into Eq. 2.35 we obtain the equation for the induced dipole moment:

$$\mu(t) = \alpha\mathbf{E_0} \sin(2\pi\nu_0 t) \tag{2.39}$$

That value varies in accordance with the incident wave frequency and the molecule becomes a source of radiation at that frequency ($\nu_0$).

In the present work the interest is primarily in the effects that molecular vibrations have in modulating this radiated spectrum. If a given molecule vibrates with a frequency of its own the components of the polarizability tensor $\alpha_{ij}$ may be represented in the approximate form:

$$\alpha_{ij} = (\alpha_{ij})_0 + \left(\frac{d\alpha_{ij}}{dQ}\right)_0 Q \tag{2.40}$$

where $\frac{d\alpha_{ij}}{dQ}$ is the change of component $\alpha_{ij}$ in the course of the given vibration (characterized by the normal coordinate Q) describing the displacement of all nuclei of the atoms in the molecule during vibration about their equilibrium positions, and $(\alpha_{ij})_0$ is the value of $\alpha_{ij}$ at the equilibrium positions of the nuclei.

The normal coordinate varies as:

$$Q_\nu = A_\nu \cos(2\pi\nu t) \tag{2.41}$$

where $A_\nu$ is the amplitude of the given normal vibration of frequency $\nu$. Combining Eqs. 2.41 and 2.40 we can write (in matrix notation)

$$\alpha = \alpha_0 + \left(\frac{d\alpha}{dQ}\right)_0 A_\nu \cos(2\pi\nu t) \tag{2.42}$$

If we substitute Eq. 2.42 into Eq. 2.39 we obtain an expression for the induced dipole moment of the molecule vibrating with the frequency $\nu$ acted upon by an electromagnetic wave of frequency $\nu_0$:

$$\mu_{ind}(t) = \alpha_0 \mathbf{E}_0 \cos(2\pi\nu_0 t) + \left(\frac{d\alpha}{dQ}\right)_0 A_\nu \mathbf{E}_0 \cos(2\pi\nu_0 t)\cos(2\pi\nu t). \tag{2.43}$$

Using a simple trigonometric identity we finally arrive at the generally accepted equation for the induced dipole moment:

$$\mu_{ind}(t) = \alpha_0 \mathbf{E}_0 \cos(2\pi\nu_0 t) + \frac{1}{2}\left(\frac{d\alpha}{dQ}\right)_0 A_\nu \mathbf{E}_0 \left[\cos(2\pi(\nu_0 - \nu)t) - \cos(2\pi(\nu_0 + \nu)t)\right] \tag{2.44}$$

The scattered radiation contains, along with the elastic contribution of $\nu_0$ known as the Rayleigh scattering, terms known as Raman bands with the frequencies $\nu_0 \pm \nu$. The scattering with decreased energy (relatively to the Rayleigh scattering) $h\nu_{R(St)}$ is called Raman Stokes scattering and the scattering with increased energy $h\nu_{R(aSt)}$ is called Raman anti-Stokes scattering. The classical theory does not explain the observed difference in Stokes/anti-Stokes intensities: the Stokes component is usually much higher than anti-Stokes. In order to explain that we need to employ quantum-mechanical approach.

In terms of quantum mechanics the Raman effect is an interaction of a molecule and photon of light with an energy lower than the energy difference between the first excited ($\Sigma_1$) and ground ($\Sigma_0$) electronic levels in the molecule as shown on Fig.2.4.

Ordinary Raman scattering is a two-photon process. The energy levels shown on Fig. 2.4 by a dashed line are virtual levels of the molecule. The photon of initial energy $h\nu_0$ interacting with the molecule in the ground state $v_{00}$ may raise the molecule to a

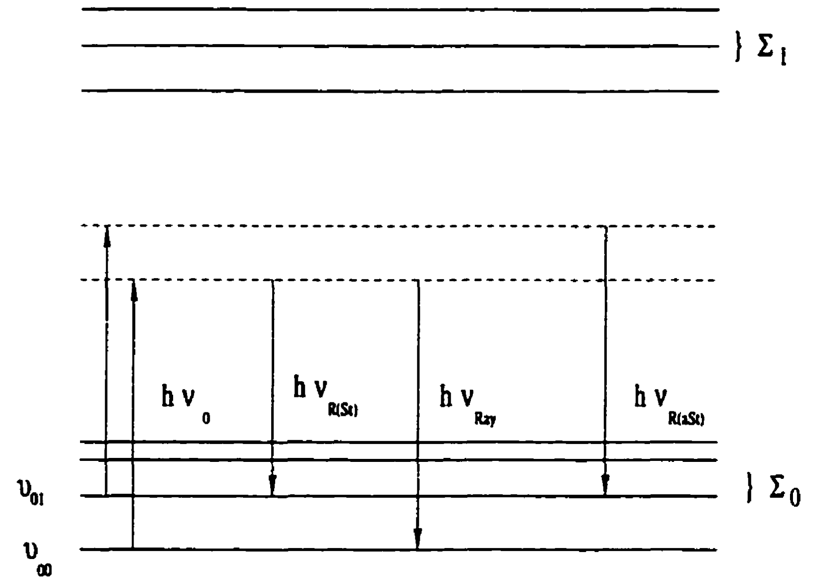

Figure 2.4: Rayleigh and Raman Scattering

higher energy level, or virtual state which is not stable. The molecule can then leave and come back to the ground level $v_{00}$. In this case the scattered photon will have the same energy as the exciting photon and the Rayleigh scattering occurs. On the other hand, if the molecule returns to an excited vibrational state $v_{01}$ the energy of the scattered photon will be equal to the energy of the incident photon minus the difference in energy between $v_{00}$ and $v_{01}$. The energy of the scattered photon in this case is smaller than the energy of the incident one and Raman Stokes scattering occurs. Anti-Stokes scattering occurs when a molecule in a vibrationally excited state $v_{01}$ rises to a higher virtual level by interacting with the incident light and then returns to the ground $v_{00}$ state. In this case, the energy of scattered photon is equal to the energy of the incident photon plus the energy difference between $v_{00}$ and $v_{01}$. According to the Boltzmann's law most of the molecules will always be in the vibrational ground state $v_{00}$. It can be consequently shown [123] that the intensity ratio of anti-Stokes to Stokes radiation is given by:

$$\frac{I^{aSt}}{I^{St}} = \frac{(\nu_0 + \nu)^4}{(\nu_0 - \nu)^4} e^{\frac{-h\nu}{kT}} \tag{2.45}$$

where $\nu_0$ and $\nu$ are wave numbers ($cm^{-1}$) corresponding to the frequencies of the exciting radiation and the molecular vibration, and T is the absolute temperature of the sample. It can be seen that the higher the temperature of the sample, the higher is the intensity of the anti-Stokes component.

# Chapter 3

# Experimental Apparatus and Technique

## 3.1 Brillouin Apparatus

### 3.1.1 Optical setup

The experimental apparatus used in the present experiment is essentially the same as described elsewhere [124, 125]. A schematic representation of the experimental apparatus is shown on Fig. 3.1. In this figure only the part used in the Brillouin experiment is shown. Later, the Raman spectrometer was installed and some modifications were made in order to conduct two experiments simultaneously. The part used in the Raman experiment will be described later in this chapter.

The laboratory frame of reference is defined by two beams perpendicular to each other. The laboratory $y$-axis is defined by the helium-neon laser beam directed along the axis of the Fabry-Perot interferometer. A laser beam from a single-mode argon laser (Spectra Physics Series 2000) is incident vertically along the axis of the cell and defines the $z$-axis. This beam is used as the excitation source. Its bandwidth is about 10 MHz and is centered at a nominal wavelength of 514.5 nm. It was set at power ~20 mW through all the experiments. As it is seen in Fig. 3.1, this beam is filtered by a narrow-pass filter $F_1$ and then focused by the lens $L_3$ (f=30 cm) in the center of the cryostat cell containing the sample.

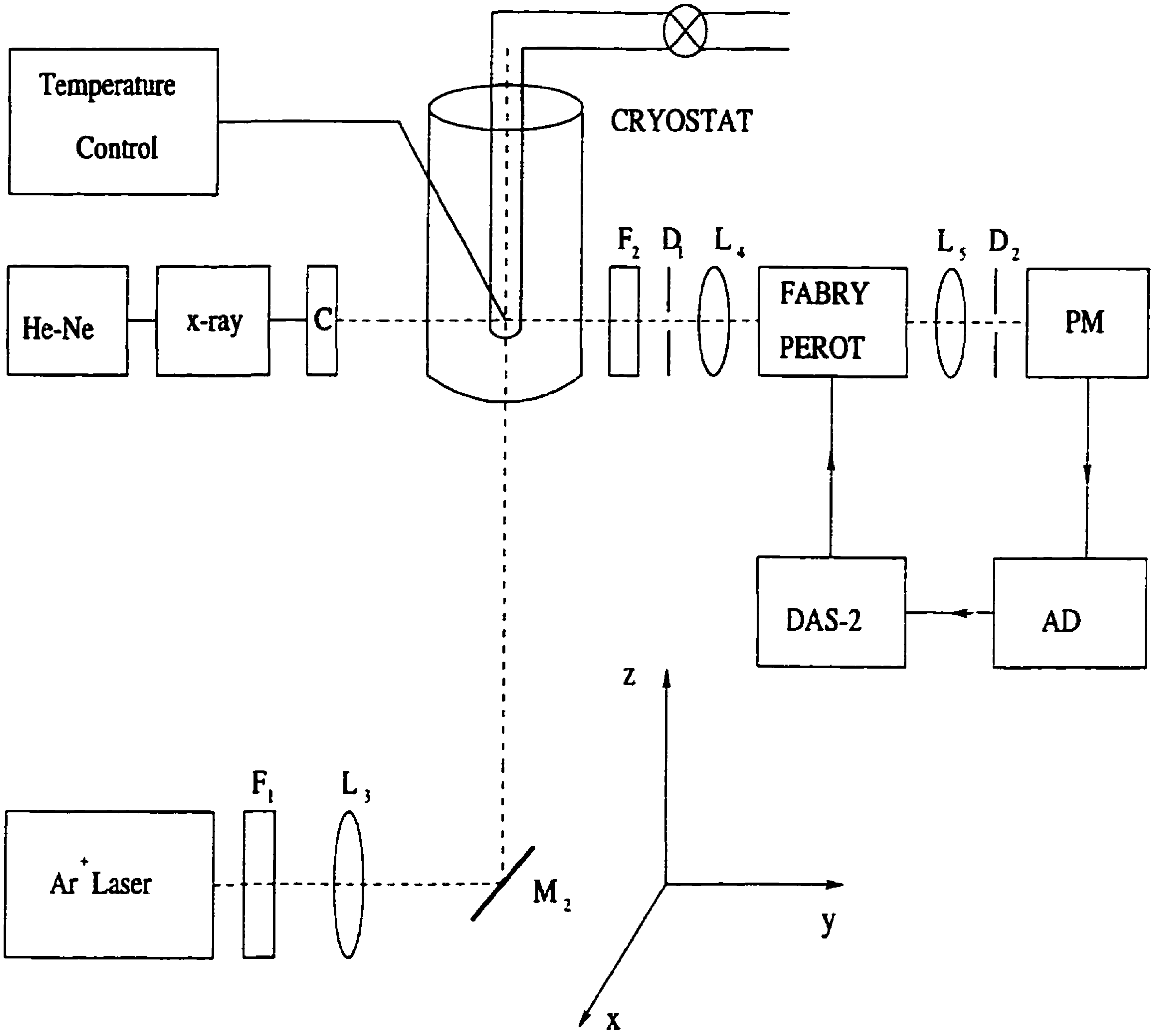
Temperature Control
CRYOSTAT
He-Ne
x-ray
C
F₂
D₁
L₄
FABRY PEROT
L₅
D₂
PM
DAS-2
AD
z
y
x
F₁
L₃
Ar⁺ Laser
M₂

Figure 3.1: Experimental optical setup for Brillouin experiment: $F_1$ - narrow band pass filter, $L_3$ - focusing lens, He-Ne - alignment laser, $M_2$ - mirror, C - collimator, $Ar^+$ - argon laser. PM - photomultiplier tube, AD - amplifier discriminator, $F_2$ - narrow band pass filter, $L_4$, $L_5$ -lenses, $D_1$, $D_2$ - pinholes, DAS-2 - data acquisition system.

The direction of the $Ar^+$ laser beam and the axis of the Fabry-Perot (as determined by the reference beam of the He-Ne laser) define the $90^0$ scattering geometry. Light scattered at $90^0 \pm 0.5^0$ is filtered by a narrow-pass filter $F_2$ centered on the laser line in order to prevent any frequencies other then needed ones from entering the Fabry-Perot. The scattering cone is defined by a diaphragm $D_1$ (d=0.8cm). Light is collected by lens $L_4$ (f=20 cm) and passed to a Brillouin spectrometer. The spectrometer consists of a piezoelectrically-scanned Fabry-Perot interferometer (FP) (Burleigh RC 110), a cooled photomultiplier tube (PM) (ITT FW 130) set in photon counting mode, an amplifier discriminator (AD) (Princeton Applied Research, SSR 1120) with the threshold of the discriminator set in such a way that only peaks produced by the photomultiplier tube above certain level would pass, and a data acquisition and stabilization system (DAS-2: personal computer with custom software). The DAS controls the voltage on the piezoelectric elements scanning the Fabry-Perot, stores the spectrum in a 1280 multichannel memory and displays the spectrum on the screen.

The x-ray machine, used to determine the orientation of the crystal and its quality, is aligned with the optical axis of He-Ne laser to ensure that the radiation passes through the crystal.

### 3.1.2 Fabry-Perot Interferometer

Probably the most important instrument in laser spectroscopy is the interferometer, because it is applicable in its various modifications to numerous problems. As was mentioned above the experimental confirmation of the Brillouin theory came a few years later owing to experimental difficulties such as the lack of a strong source of monochromatic light and a reliable detection technique. In modern Brillouin spectroscopy the sources are usually $Ar^+$ lasers and Fabry-Perot interferometers are the devices used to analyze the scattered light. In order to investigate the Brillouin components, which are shifted from

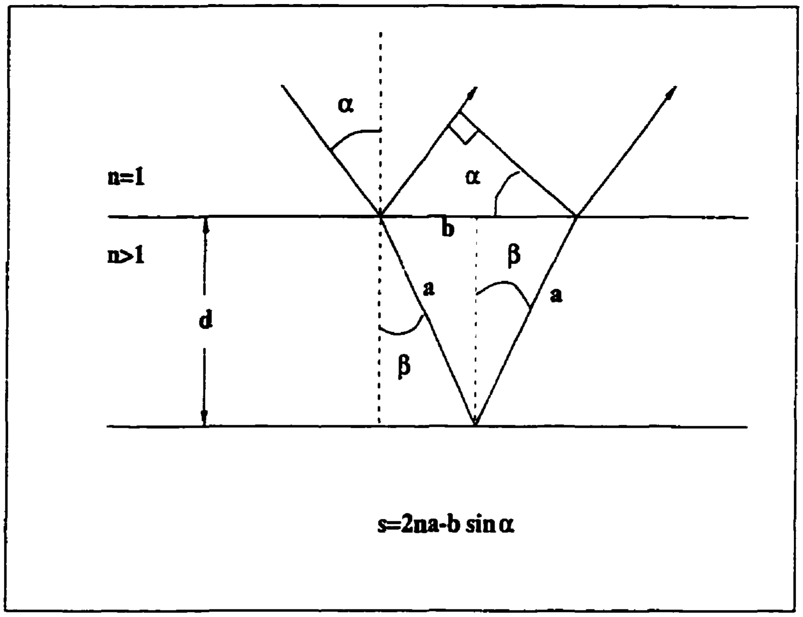

Figure 3.2: Optical path difference, s, between two reflected beams.

the Rayleigh peak by 5-10 GHz and are thousands of times weaker than the unshifted light, an instrument of very high resolution and contrast is needed. The Fabry-Perot interferometer meets all the requirements and the simple theory explaining how it works will be given here.

Assume that a plane wave of wavelength $\lambda$ is incident at the angle $\alpha$ on a plane transparent plate of width $d$ with two parallel partially reflecting surfaces as in Fig. 3.2. For two successive waves reflected from the two surfaces the path difference is given by:

$$s = (\frac{2nd}{\cos\beta}) - 2d\tan\beta\sin\alpha. \tag{3.1}$$

Because sin$\alpha$=n sin$\beta$ it can be reduced to

$$s = 2nd\sqrt{1 - \sin^2\beta}. \tag{3.2}$$

This path difference corresponds to the phase difference of

$$\Delta\,\phi = \frac{2\pi s}{\lambda}. \tag{3.3}$$

If the coefficient of reflectivity (R) is known the intensities of reflected and transmitted waves can be calculated [126]. They are (for reflected intensity)

$$I_R = I_0 R \frac{4\sin^2(\Delta\phi/2)}{(1-R^2)+4R\sin^2(\Delta\phi/2)} \tag{3.4}$$

and for transmitted intensity

$$I_T = I_0 \frac{(1-R^2)}{(1-R^2)+4R\sin^2(\Delta\phi/2)}. \tag{3.5}$$

The equations 3.4, 3.5 are known as Airy formulae. It can be seen that, for example, the maximum transmittance $I_T$=1 is for $\Delta\phi = 2m\pi$, where $m$ is an integer which specifies the "order of interference". The frequency range between two successive interference orders ($m \longrightarrow m+1$) is called the *free spectral range* (FSR) of interferometer. Using Eq. 3.3 and $\lambda = c/\nu$, the FSR can be written as

$$FSR = \frac{c}{s} = \frac{c}{2d\sqrt{n^2 - sin^2\alpha}}. \tag{3.6}$$

In most cases the angle $\alpha$=0, so the FSR becomes simply $c/2nd$, and it is $I_T$ that is normally of interest.

The full width of the transmitted maxima at the half height points can be calculated from Eq. 3.5 by setting $I_T$=$I_0$/2. The width turns out to be

$$\delta = \frac{2(1-R)}{\sqrt{R}}. \tag{3.7}$$

The ratio of the free spectral range to the halfwidth $\Delta\nu = (\delta/2\pi)$FSR is called the *finesse* (F) of the interferometer. The finesse can be written as

$$F = \frac{FSR}{\Delta\nu} = \frac{2\pi}{\delta} = \frac{\pi\sqrt{R}}{1-R} \tag{3.8}$$

Another important characteristic of the interferometer is its resolving power, which is defined as $\nu / \bigtriangleup \nu$ or $\lambda / \bigtriangleup \lambda$, and is determined by the free spectral range and finesse. The peaks with frequencies $\nu$ and $\nu + \Delta\nu$ are said to be resolved if their maxima are separated by $\delta$. It can be obtained using the Airy formulae for transmitted intensity, replacing the phase shift $\Delta\phi$ with FSR, and using the relation $\Delta\phi = 2\pi\nu/FSR$. The transmitted maxima of $\nu$ and $\nu + \Delta\nu$ will be resolved if $\Delta\nu$=FSR/F. So, the resolving power can be expressed as

$$\frac{\nu}{\Delta\nu} = \frac{\nu}{FSR}F = F\frac{s}{\lambda}. \tag{3.9}$$

The piezoelectrically-scanned Fabry-Perot interferometer (finesse around 30-40 and FSR around 18.20 GHz) used in this experiment is essentially two parallel plates with reflectivity ~90% which are flat to within $\lambda/200$, and are separated by distance d, which changes during the scan. The second major difference from the case of the parallel plate is that the light was reflected three times in the Fabry-Perot interferometer by displacing the successive passes laterally using retro-reflectors. This operation enormously improves the contrast of interferometer, which is defined as the ratio of maximum intensity to minimum. From the Airy formulae the contrast $C=1+4F^2/4\pi^2$, where F is the finesse. The theoretical Airy functions for the multipass interferometer can be found by raising the Airy function to the power of m, where m is number of passes. The contrast of the multipass interferometer is $C_m=C^m$ and finesse $F_m=F/(\sqrt{(2^{1/m}-1)}$ [126].

### 3.2 Raman Apparatus

The experimental apparatus used in the present Raman experiment is a standard one, which employs a laser beam as the excitation source, a spectrometer driven by data acquisition system and a photomultiplier used as the detector of the signal. The present work was started as a Brillouin investigation of methane; the apparatus was later modified in order to conduct the Raman spectroscopy experiment as well. The same laser beam which is used in Brillouin experiment is being used to collect the Raman spectra at the same time as the Brillouin spectra.

The measurements were made using a cooled RCA C31034 photomultiplier tube and a Spex model 1401 double grating spectrometer, which was modified for computer control and data acquisition. A schematic optical diagram for Raman spectroscopy is shown in Fig. 3.3. The optic axis of the spectrometer and the $y$-axis of the laboratory reference frame were coincident and were both defined by a He-Ne laser beam. The incident (vertical) beam of the argon laser defined the laboratory $z$-axis. The scattered light was collected horizontally through a polarizer, P, by a collecting lens, $L_1$. Then, the light was focused by the lens $L_2$ onto the entrance slit of the spectrometer after passing through a polarization scrambler S, which was required to compensate for the different polarization sensitivities of the spectrometer. The frequency calibrations were done with a hollow-cathode thorium/neon discharge tube.

## 3.3 Cryogenic Setup and Sample Preparation

### 3.3.1 Helium Cryostat

A modified commercial liquid helium cryostat (Janis Research Co. Model 10DT) used in the experiments was the same as in Ref. [127, 128]. The outer body of the cryostat was made of stainless steel. It contained two reservoirs: a five liter reservoir for liquid nitrogen, which was automatically refilled every 5-6 hours from a liquid nitrogen tank and controlled by a liquid level sensor and a seven liter reservoir for liquid helium which was manually filled every 1.5-2 days from a liquid helium tank and monitored by a liquid helium indicator.

Crystals of sample gas were grown in a cell mounted in the cryostat. The cell (Fig.

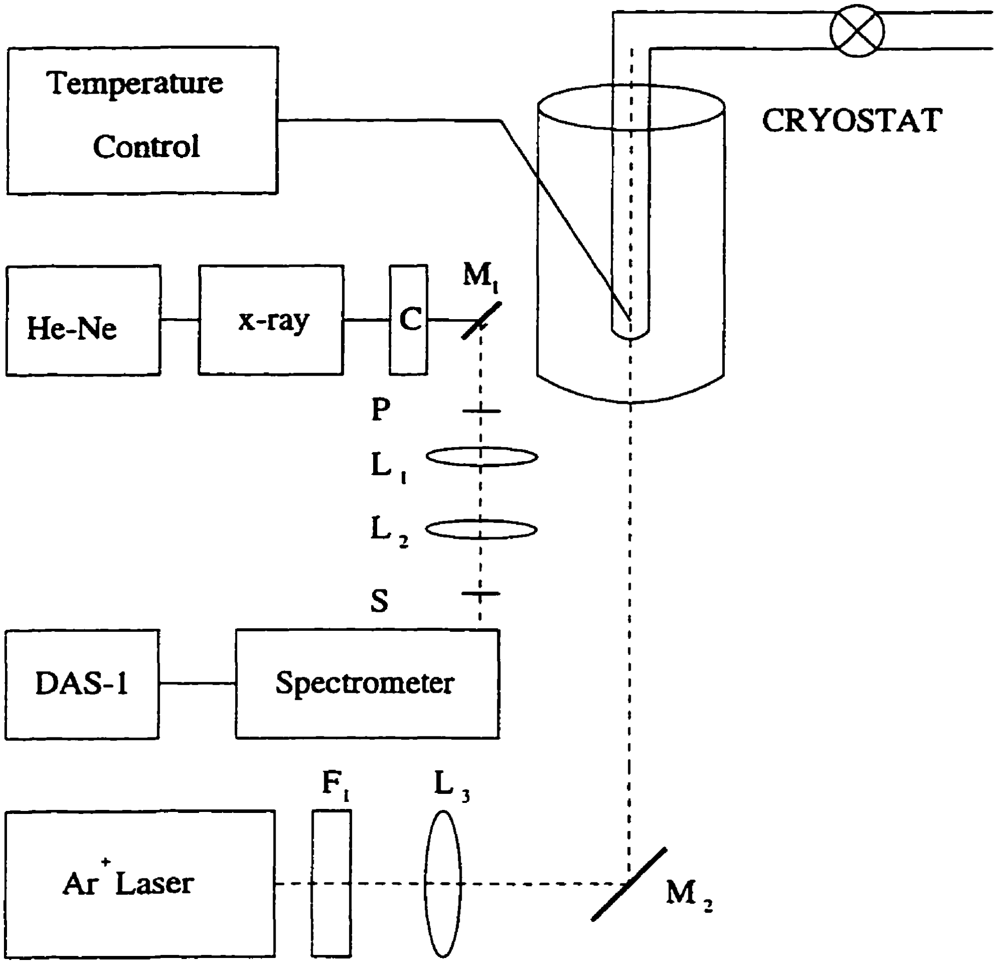
Temperature Control
CRYOSTAT
He-Ne
x-ray
C
$M_1$
P
$L_1$
$L_2$
S
DAS-1
Spectrometer
$F_1$
$L_3$
$Ar^+$ Laser
$M_2$

Figure 3.3: Experimental setup for Raman experiment: $F_1$ - narrow band pass filter, $L_3$ - focusing lens, He-Ne - alignment laser, $M_2$ - mirror, C - collimator, $Ar^+$ - argon laser, $L_1$, $L_1$ - lenses, DAS-1 - data acquisition system, P - polarizer, S - scramble.

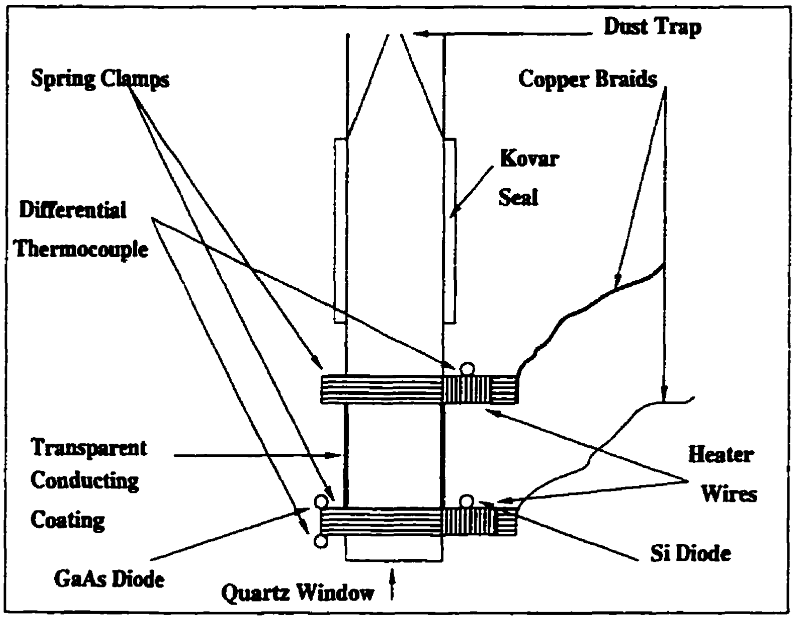
Dust Trap
Spring Clamps
Copper Braids
Kovar
Seal
Differential
Thermocouple
Transparent
Conducting
Coating
Heater
Wires
Si Diode
GaAs Diode
Quartz Window

Figure 3.4: The cryostat quartz cell.

3.4), was attached to a long stainless steel tube, and was suspended in the central bore of the cryostat. The top part of the tube was connected to a supply of sample gas, a rotary vacuum pump and a pressure gauge. The cell could be rotated through the rotary seals. The low temperatures were maintained by a flow of liquid helium into a heat exchanger through a capillary tube. The helium flow is adjusted by a valve which is controlled by a temperature control unit.

The heat exchanger was connected to the copper braids shown in Fig. 3.4. These braids were soldered to phosphor-bronze clamps, attached to the lower and upper part of the cell. The lower clip had GaAS and Si temperature sensors mounted on it. Another side of the clamp had a differential thermocouple. Another clamp had the second junction of the thermocouple. This allowed for creation and maintenance of a temperature gradient between the bottom and top of the cell by using heaters that were attached to each clamp. By controlling the current through these heaters a fine control of the temperature was achieved.

The cell was made from a quartz tube of inner diameter 3 mm, outer diameter 5 mm and length of about 2 cm, and was fitted with quartz-to-Kovar seal at the top. A dust trap between the cell and the inlet tube prevented dust particles from settling on the bottom of the cell. The bottom of the cell was closed by a polished fused quartz plug with epoxy resin. There were two aluminum shields around the cell. The inner shield was maintained at the same temperature as the heat exchanger and the outer one at liquid nitrogen temperature. Plexiglas windows on these shields reduce radiative heating effects and prevent the occurrence of higher temperature spots inside the cell. The outside windows through which the scattered light passed were made of Plexiglas to allow x-ray transmission. The window on the bottom of the cryostat tail through which the laser beam passed was made of quartz.

The unique feature of the cell was the deposition of a thin, optically transparent, electrically conducting coating on the cell body between the clamps. The film has about a 70% optical transmission coefficient and 10 ohms electrical resistance, and was about 1 cm high. Two thin brass clamps were used for electrical contact with the film. Teflon rings were used to isolate these clamps from the phosphor bronze cooling clamps. This film is crucial in the cooling procedure. It melts the crystal away from cell walls and provides heat to keep the crystal from re-growing during the cooling period.

The cell temperature was controlled in different stages, starting with the valve which regulated the helium flow into the heat exchanger. The temperature at the bottom of the heat exchanger was controlled at $\sim$ 4 K below the cell temperature by a GaAs diode in conjunction with a temperature controller (Lake Shore Cryotronics Inc., Model DTC-550) and heater wires (the heat exchanger, the heat exchanger's GaAS diode and the heater wires are not shown in Fig. 3.4). The temperature controller provides a constant current of 10 $\mu$A through the diode. The forward voltage of GaAs diodes increases with decreasing in temperature; the temperature controller compares the voltage across the diode with a very stable set-point voltage. The resulting difference is amplified by the controller and is used to regulate the current through the heater wires. The temperature of the bottom of the cell (which was taken as the temperature of the sample) was controlled by a similar proportional electronic unit to within ±0.01 K. The temperature on the top of the cell, which creates the temperature gradient in the cell, measured by Keithley Instrument microvoltmeter, was controlled via a differential thermocouple and heater proportional control system. The current to the cell heater wires was unequally divided between the heaters at the top and bottom of the cell by the means of a potentiometer with top hotter than bottom. This current was adjustable and was usually set to provide a gradient of ~1 K/cm.

### 3.3.2 Single Crystal Growth and Cooling

The single crystals were grown by Bridgman's method [129]. The method involves solidification from the liquid at the triple point in the presence of a temperature gradient. The cell was filled with the gas after several flushes and then the cryostat was precooled with liquid nitrogen. This procedure usually took about one day. After the cryostat was precooled, liquid helium was transferred into the helium reservoir and the sample was cooled to temperature slightly higher than the triple point. Then the liquid was left for 3-4 hours to come to equilibrium. The crystals were generally grown by lowering the temperature of the cell very slowly by 0.005-0.1 K per hour in the presence of the temperature gradient between the top and the bottom of the cell until a small seed was formed on the bottom. This procedure usually took around 10-12 hours. X-ray diffraction photographs were then taken to ensure that the crystal seed was single and of good quality. Polycrystalline samples are identified by twin or multiple Lauē spots. The mechanically strained crystals are identified by distortions of the Lauē spots. These photographs were also used to determine the orientation of the crystal. The orientation procedure was completely computerized and based on the technique of stereographic projection. The measured coordinates of the Lauẽ spots were put into the program and a set of Euler angles was obtained as an output. The crystal was then rotated about the cell axis and an x-ray picture was taken again. Rotation about the $z$-axis must change the angle $\phi$ by the same amount and leave $\theta$ and $\chi$ unchanged. When consistent orientations were obtained the crystals were then ready for cooling.

Cooling a van der Waals solid is a difficult procedure because of its high coefficient of thermal expansion. Also, because of the difference between coefficients of thermal expansion of the crystal and cell walls crystals prefer to stick to the walls and hence shatter easily on cooling. Therefore not too many Brillouin scattering experiments on cooled single crystals of this type have been done in the past.

In the present experiment in order to get a good crystal while cooling, one has to achieve a fine balance between the rate of pumping, the rate of cooling and the rate at which film voltage is increased. The film voltage is raised and the proper rate of pumping is established in order to melt the solid away from the sides of the cell and minimize the effects of melting. The result is a crystal standing freely on the bottom of the cell. Once the crystal is released from the sides, the temperature of the cell is lowered automatically by about 10 K per hour to any desired value. It is desirable to regrow the crystal against the walls of the cell, in order to prevent the parasitic scattering of light between the crystal and the walls but this is extremely difficult to achieve. After the crystal was cooled to the desired temperature an x-ray photograph was taken to check if crystal had become strained or changed its orientation. X-ray pictures were also taken after the crystal had gone through the phase transition. To the author's knowledge this is the first experiment where single and unstrained crystals were successfully taken through the solid-solid phase transition and Brillouin data were collected.

# Chapter 4

# Raman Measurements

There is an abundance of Raman spectroscopy results for liquid [25, 22] and polycrystalline [27, 28, 29, 30] methane at different pressures and temperatures but there is a relative scarcity of Raman scattering data pertaining to phase transitions at low temperatures and RT coupling in single crystals.

It is very well known that a methane-like five-atomic tetrahedral molecule has four fundamental bands (1-0 transitions) [117]: a totally symmetric $\nu_1(A_1)$, a doubly degenerate $\nu_2(E)$ and two triply degenerate $\nu_3(F_2)$ and $\nu_4(F_2)$. All four fundamentals are Raman active but only the two triply degenerate vibrations $\nu_3$ and $\nu_4$ are infrared active. The fundamental modes of $CH_4$ and $CD_4$ are summarized in Table 4.1.

Attempts to detect the lattice external modes in phase II of $CH_4$ and phases II and III of $CD_4$ were unsuccessful. Only the two lines $\nu_1$ and $\nu_3$ were consistently observed over the investigated temperature range, the ones which change the most as the crystals go through their phase transitions.

## 4.1 $CH_4$

The typically observed Raman spectra of $CH_4$ without the polarizer and scrambler are shown in Fig. 4.1. These are unprocessed spectra as observed on the display screen of the data acquisition system. Fig. 4.2 shows the spectra of $\nu_1$ and $\nu_3$ in both phases obtained with the polarizer and after the spectra were filtered by a numerical three-point

Table 4.1: Fundamental frequencies[1] of gaseous $CH_4$ and $CD_4$. Adapted from Ref. [117].

| Molecule | $\nu_1(A_1)$ | $\nu_2(E)$ | $\nu_3(F_2)$ | $\nu_4(F_2)$ |
|---|---|---|---|---|
| $CH_4$ | 2914.2 R. | 1526 I$^*$. R$^*$. | 3020.3 R. | 1306.2 I. |
| $CD_4$ | 2087.7 R. | 1054 R$^*$. | 2258.2 I. R. | 995.6 I. |

smoothing procedure.

Occurrence of the transition is confirmed by observing the splitting of $\nu_1$ and enormous narrowing and splitting of $\nu_3$ which takes place within a very narrow temperature range. The spectra of these lines were collected at different crystal orientations but within the errors of the measurements no differences were observed.

The full-width at half-maximum (FWHM) of $\nu_1$ was determined by employing a deconvolution process to correct for the finite spectrometer resolution. In this process the observed profiles for both the Raman line and the laser (instrumental) line were first fitted with Lorentzian functions. In both cases the quality of the fits was excellent and the primary effect was one of smoothing. The Fourier (cosine) coefficients were then determined for each fitted function and deconvolution was achieved by simply dividing the corresponding coefficients. The corrected spectrum was then obtained as the inverse Fourier transform [130]. The resulting profiles were then fitted to a Lorentzian lineshape and the position of the peak and its FWHM were deduced. The results for the $\nu_1$ line are shown in Fig. 4.3. The points for liquid $CH_4$ from Ref. [131] were measured using Fabry-Perot interferometry and are consistent with the present measurements. The Raman shift values (Fig. 4.3) are consistently higher by $\sim 3\ cm^{-1}$ than those of Ref. [24]. There is little change in the shift throughout the temperature range of phase I, but there is a distinct downshifting effect on entering phase II. The most interesting effect is the widening of the main peak of $\nu_1$ when the crystal goes through the phase transition. The width of the peak changes from 1.6 to 0.87 $cm^{-1}$ through the temperature range of phase I. On passing through the phase transition at 20.5 K it jumps to 1.57 $cm^{-1}$ and continues to rise as the temperature is further reduced. Assuming, as suggested elsewhere (Ref. [132]), that the principal broadening mechanism in phase I is fast-modulation dephasing, it is likely that the increased width in phase II is due to an inhomogeneous broadening contribution arising from the ($Fm3c$) ordering.

---

[1] R./I. indicate whether band was observed in Raman or infrared spectrum. R$^*$ refers to fundamentals obtained from observed overtones in the Raman spectra.

In order to calculate the linewidth of $\nu_3$ it is necessary to eliminate the line $2\nu_2$. Because $\nu_3$ is completely depolarized and $2\nu_2$ is completely polarized this can be achieved by employing a polarizer (compare Fig. 4.1 and 4.2). The width of the $\nu_3$ feature averages about 70 $cm^{-1}$ in phase I, and instrumental linewidth contributions were not significant in this case. The changes in $\nu_3$ are the most obvious ones observed in this experiment (Fig. 4.4). The Raman shift changes from 3026 $cm^{-1}$ at 90 K to 3016.9 $cm^{-1}$ at 20.5 K and then it downshifts to 3014.5 $cm^{-1}$ in phase II. The $\nu_3$ linewidth changes by a factor of 3 from 90 K to 20.5 and when the crystal goes through the phase transition it suddenly decreases from 34 $cm^{-1}$ to 4.6 $cm^{-1}$. This latter effect was a sensitive test of whether the phase transition had actually occurred. In some cases a distinct "overcooling" effect was observed when the temperature was well below the normal phase transition temperature but the linewidth and height of $\nu_3$ clearly indicated that the phase transition had not occurred. A light tapping on the cryostat would then initiate the phase transition which would be complete within a few minutes. An attempt was made to observe the associated hysteresis effect in the behavior of linewidth corresponding to that demonstrated in the enthalpy measurements of Ref. [14]. The single point at 18.5 K in Fig. 4.4 suggests the existence of such an effect but more precise measurements of the sample temperature are needed in order to confirm it.

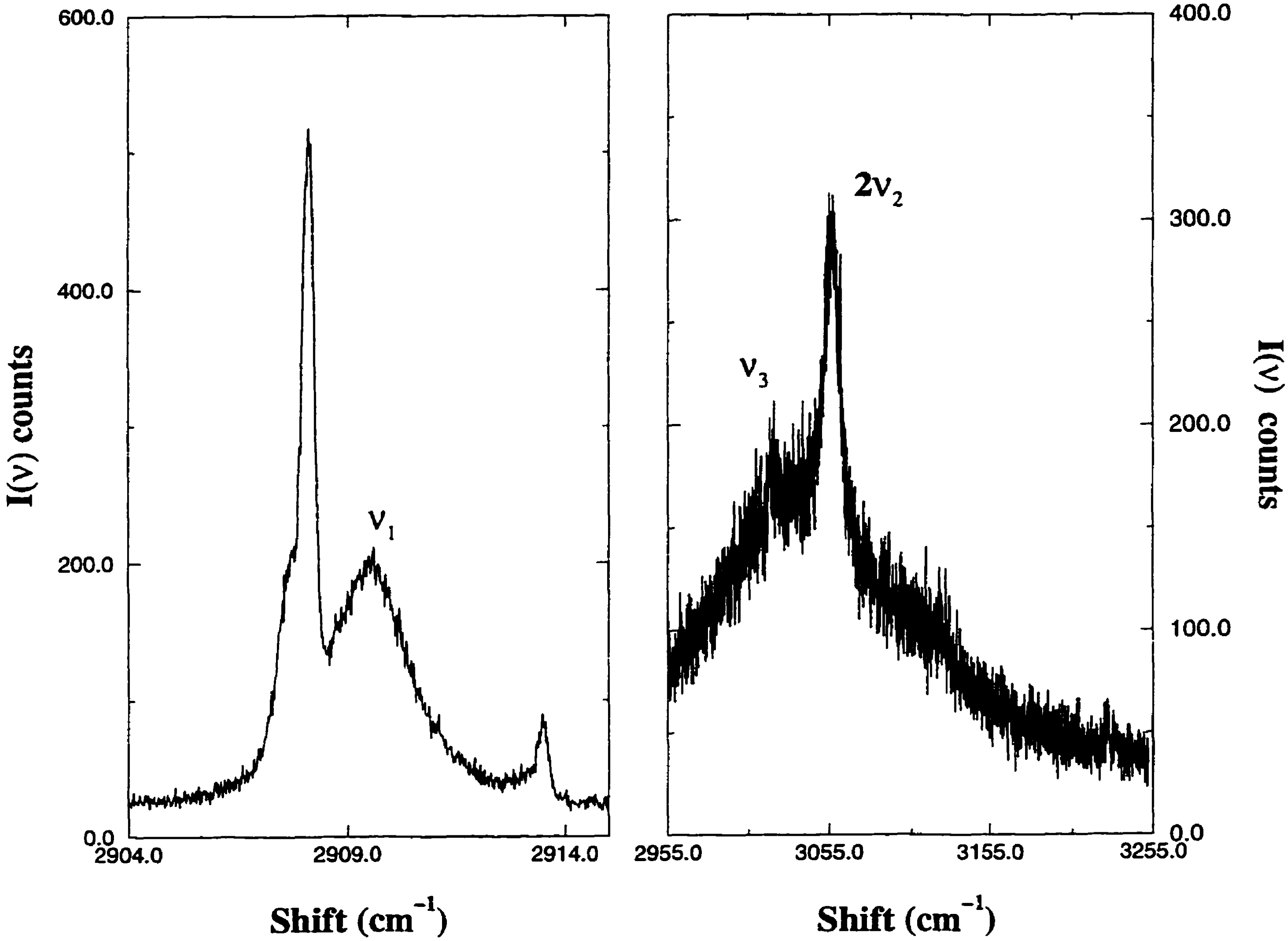

Figure 4.1: The Raman spectra of $\nu_1$ and $\nu_3$ and $2\nu_2$ of $CH_4$ at T=89 K. The sharp peaks around $\nu_1$ are the peaks from the thorium/neon calibrating lamp. The spectra were collected without polarizer and scrambler.

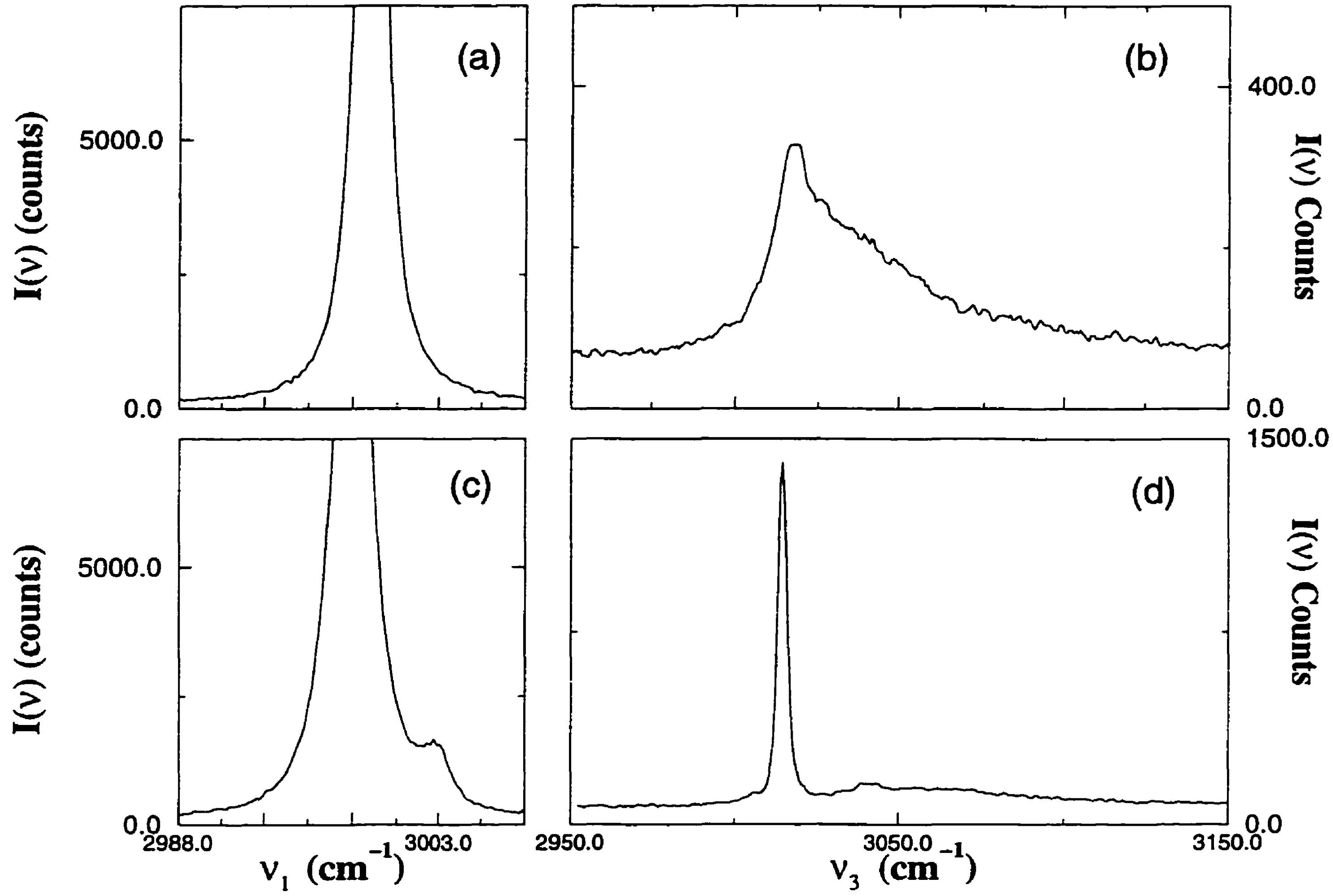

Figure 4.2: Typical Raman spectra of $\nu_1$ and $\nu_3$ of $CH_4$. (a) and (c) show the $\nu_1$ spectrum in phases I and II, respectively, and (b) and (d) are corresponding spectra for $\nu_3$. $\nu_3$ was recorded with the polarizer axis perpendicular to the polarization vector of the scattered light.

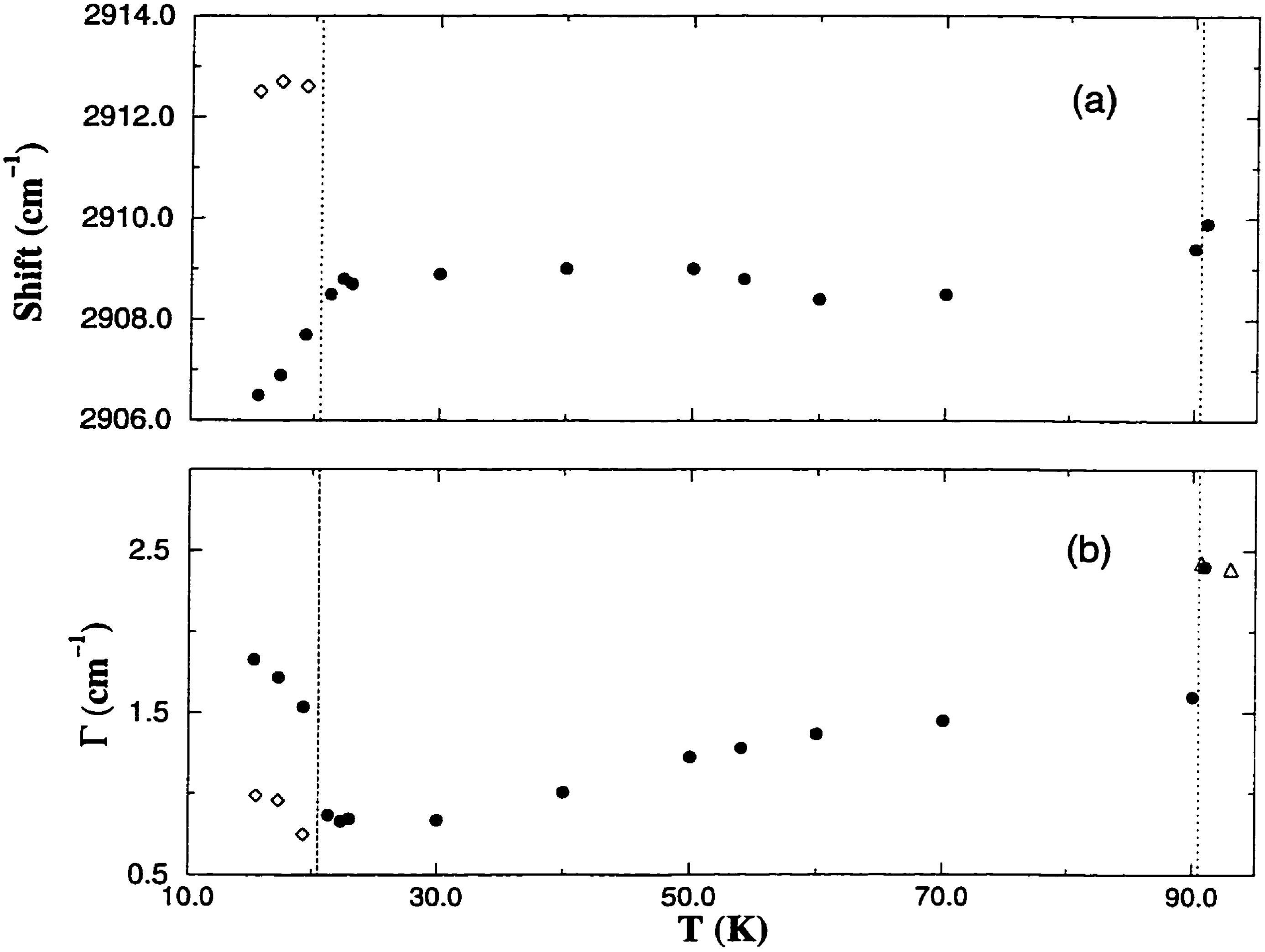

Figure 4.3: The shift (a) and full width (b) at half height of $\nu_1$ of $CH_4$ as a function of temperature. (◇) indicate the second peak which appeared after the phase transition. (△) are from Ref. [131]. The errors in measurements of shift are of the size of the symbols. The errors in measurements of FWHM are estimated to be ~ 2%. The dashed line is positioned at the phase transition temperature of 20.5 K and at the liquid-solid phase at 90.67 K.

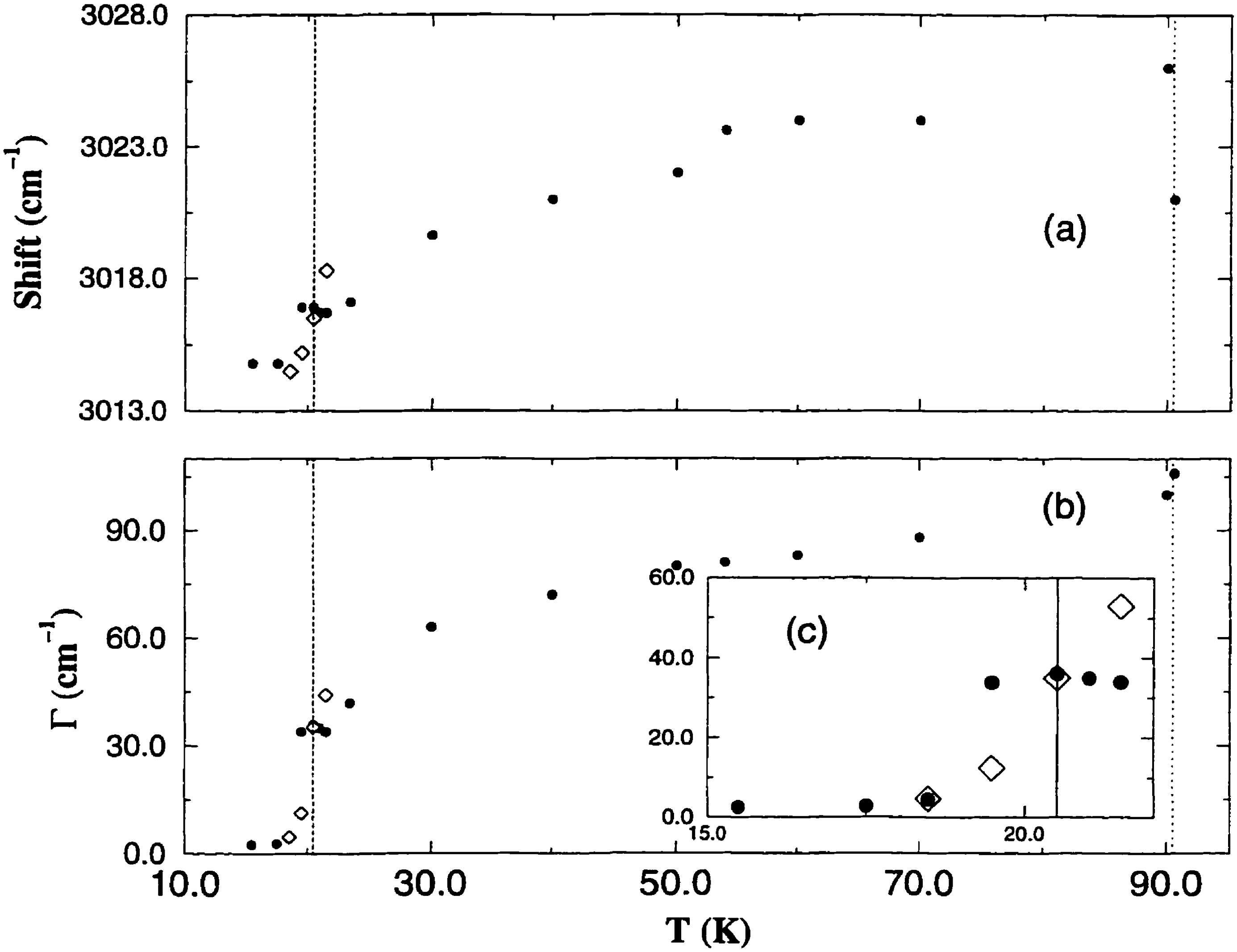

Figure 4.4: The shift (a) and full width at half height (b) of $\nu_3$ of $CH_4$ as a function of temperature. The (•) are for decreasing and (◇) for increasing temperatures. The inset (c) shows a magnified view of the FWHM around the phase transition temperature. The errors in measurements of shift are of the size of the symbols. The errors in measurements of FWHM are estimated to be ~ 2%. The dashed line is positioned at the phase transition temperature of 20.5 K and at the liquid-solid phase at 90.67 K.

## 4.2 $CD_4$

The features of Raman spectra of deuterated methane are similar to those of methane. Because of the mass difference between $CH_4$ and $CD_4$ the two fundamental modes $\nu_1$ and $\nu_3$ and the overtones $2\nu_2$ and $2\nu_4$ of $CD_4$ are more closely spaced than in $CH_4$. The proximity of both overtones and $\nu_3$ to the $\nu_1$ line gives rise to Fermi resonance causing these relatively weak lines to appear much more strongly than they otherwise would. The unprocessed Raman spectra of $CD_4$ are shown in Fig. 4.5. It can be seen that there are some common features between $CD_4$ and $CH_4$ in phases I and II such as narrowing of the $\nu_3$ as temperature decreases and splitting of the $\nu_1$ as the temperature drops below the first phase transition, as shown in Fig. 4.6(a) and (c). Phase III manifested itself not only by the splitting of the $\nu_3$ line (see Fig. 4.6(d) and (f)) but by the changes in intensity and polarization of the $\nu_1$ line. The ratio of intensities $I_{\nu_1}/I_{\nu_3}$ in the phase II is 3/1. When the crystal went through the II-III phase transition this ratio changed to 1/1.1. This change was accompanied by a change in polarization as well: in phases I and II $\nu_1$ is completely polarized. In phase III it becomes completely depolarized.

The full-width at half-maximum of $\nu_1$ was determined by the same procedure described above for $CH_4$. The Raman shift values and FWHM for $\nu_1$ are shown in Fig. 4.7. There is little change in the shift through the temperature range but it downshifts on entering phase II from $\sim$ 2096 to 2094.5 $cm^{-1}$ and there is no significant change of shift when the crystal enters phase III. The second peak, which was easily seen in phase II, was not observed in phase III, most probably because of the intensity decrease described above.

The behavior of the $\nu_1$ line width is quite different from its counterpart in $CH_4$. First, it is much wider (approximately by a factor of 2) at higher temperatures. When the liquid solidifies the line broadens (the effect is better seen in the $\nu_3$ line) and upon entering phase II the line becomes narrower. Exactly the opposite of the latter effects was observed in $CH_4$.

The $\nu_3$ Raman shift varies more throughout phase I than does $\nu_1$, (Fig. 4.8). It jumps from $\sim$ 2258 to 2264 $cm^{-1}$ when the liquid solidifies and then for about 40 K stays the same. Below $\sim$50 K it slowly downshifts to 2257 $cm^{-1}$ and on entering phase II it drops to 2256 $cm^{-1}$. In phase III a new peak appears (see Fig. 4.7(f)). The width of the $\nu_3$ line averages $\sim$ 60 $cm^{-1}$ from the melting point to about 50 K, where it rapidly decreases to about 10 $cm^{-1}$ at T=28 K. A further decrease of temperature by 1 K initiates the first phase transition and the linewidth jumps to $\sim$2 $cm^{-1}$. After the first phase transition takes place it becomes possible to fit the line to a Lorentzian profile. After the crystal goes through the II-III phase transition the width stays approximately the same but the shape of the line becomes Gaussian.

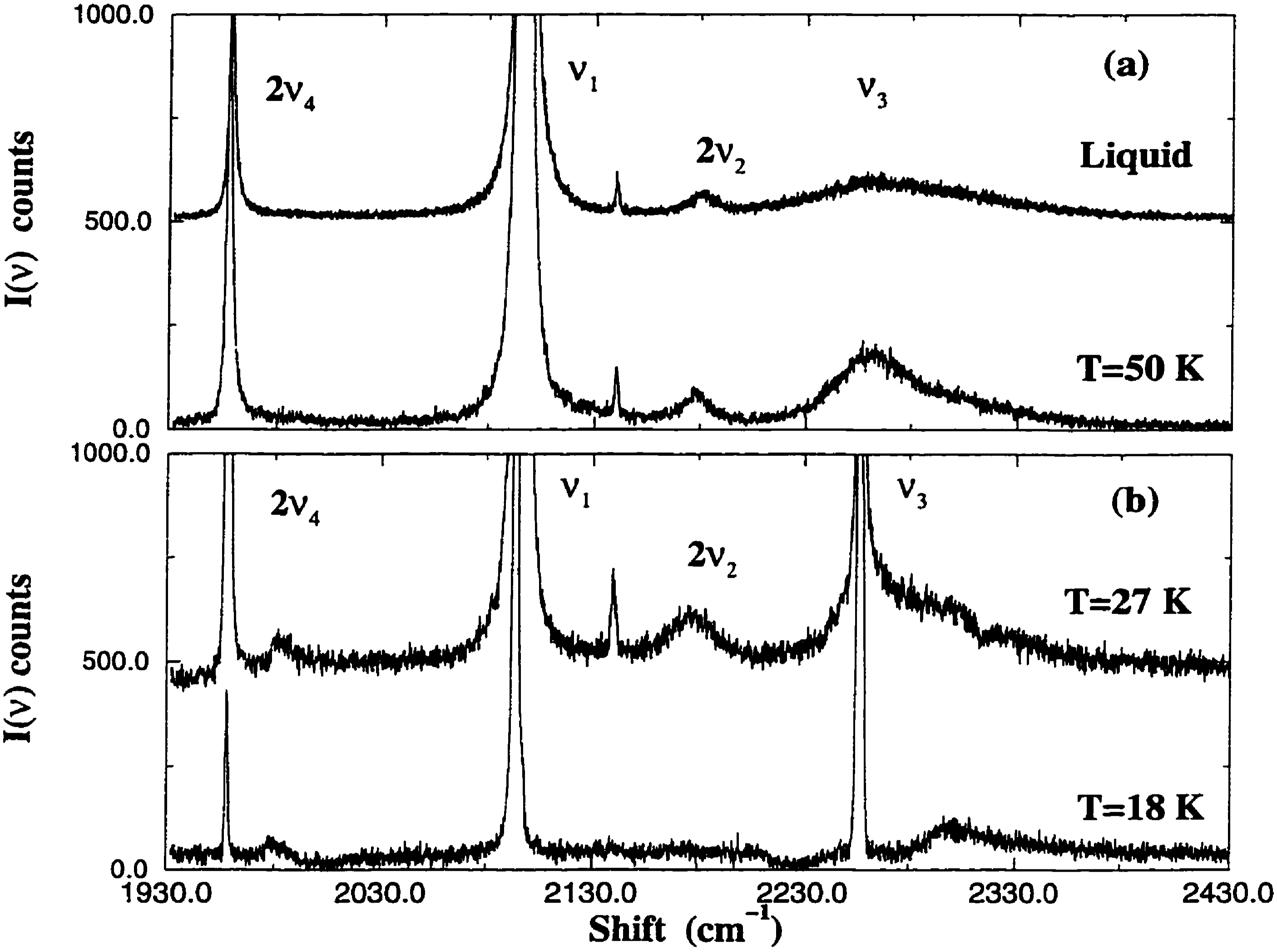

Figure 4.5: Unprocessed representative Raman spectra of $CD_4$. All spectra but the one at T=18 K are collected without polarizer. The spectrum at T=18 K was collected with the polarizer axis perpendicular to the polarization vector of the scattered light. The small peak between $\nu_1$ and $2\nu_2$ is the $\nu_1$ line of $CD_3H$.

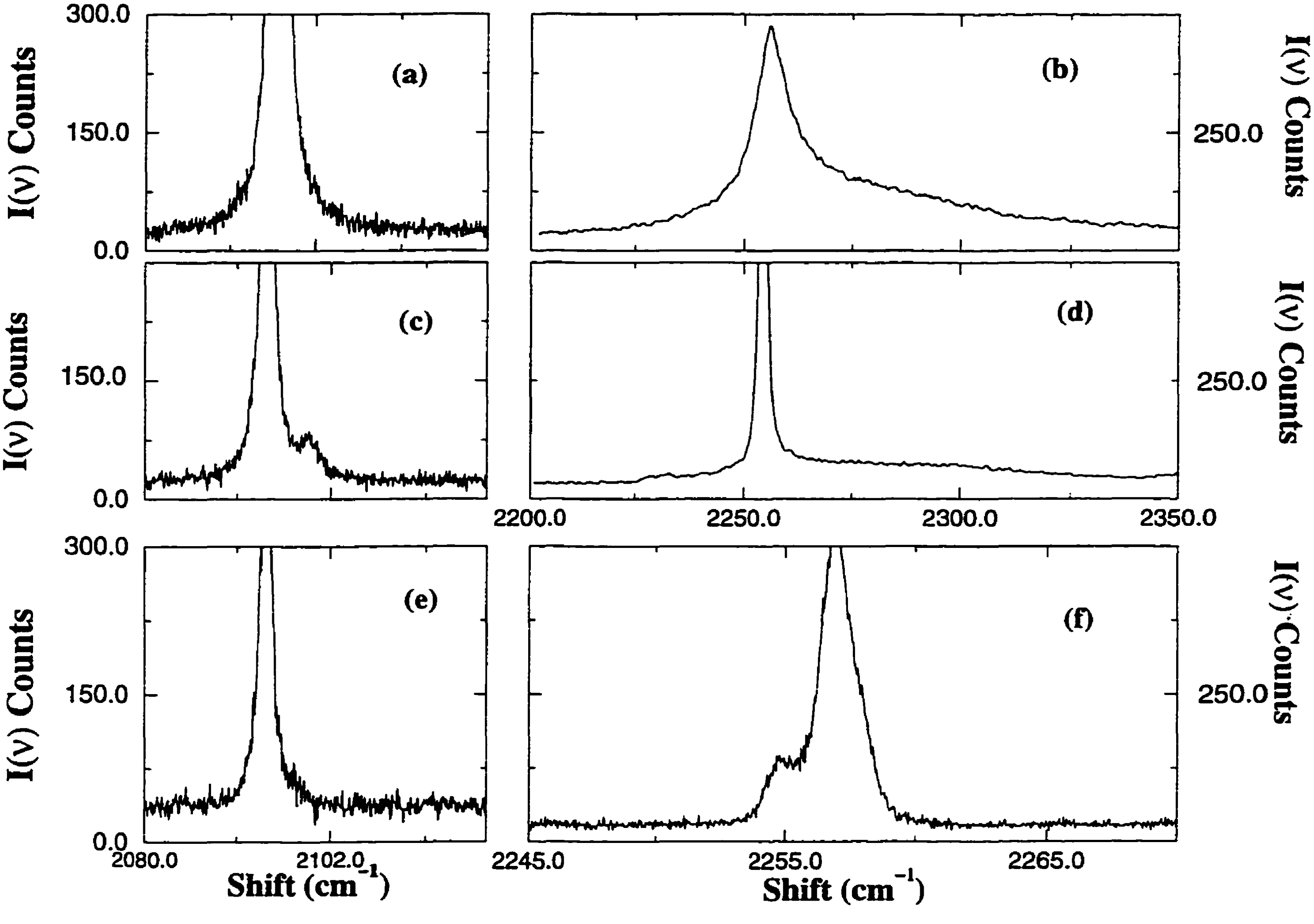

Figure 4.6: Smoothed spectra of $\nu_1$ (a, c, e) and $\nu_3$ (b, d, f) of $CD_4$ in three phases with phase I at the top. $\nu_1$ was recorded with the polarizer axis parallel to vector of the scattered light and $\nu_3$ with the axis perpendicular.

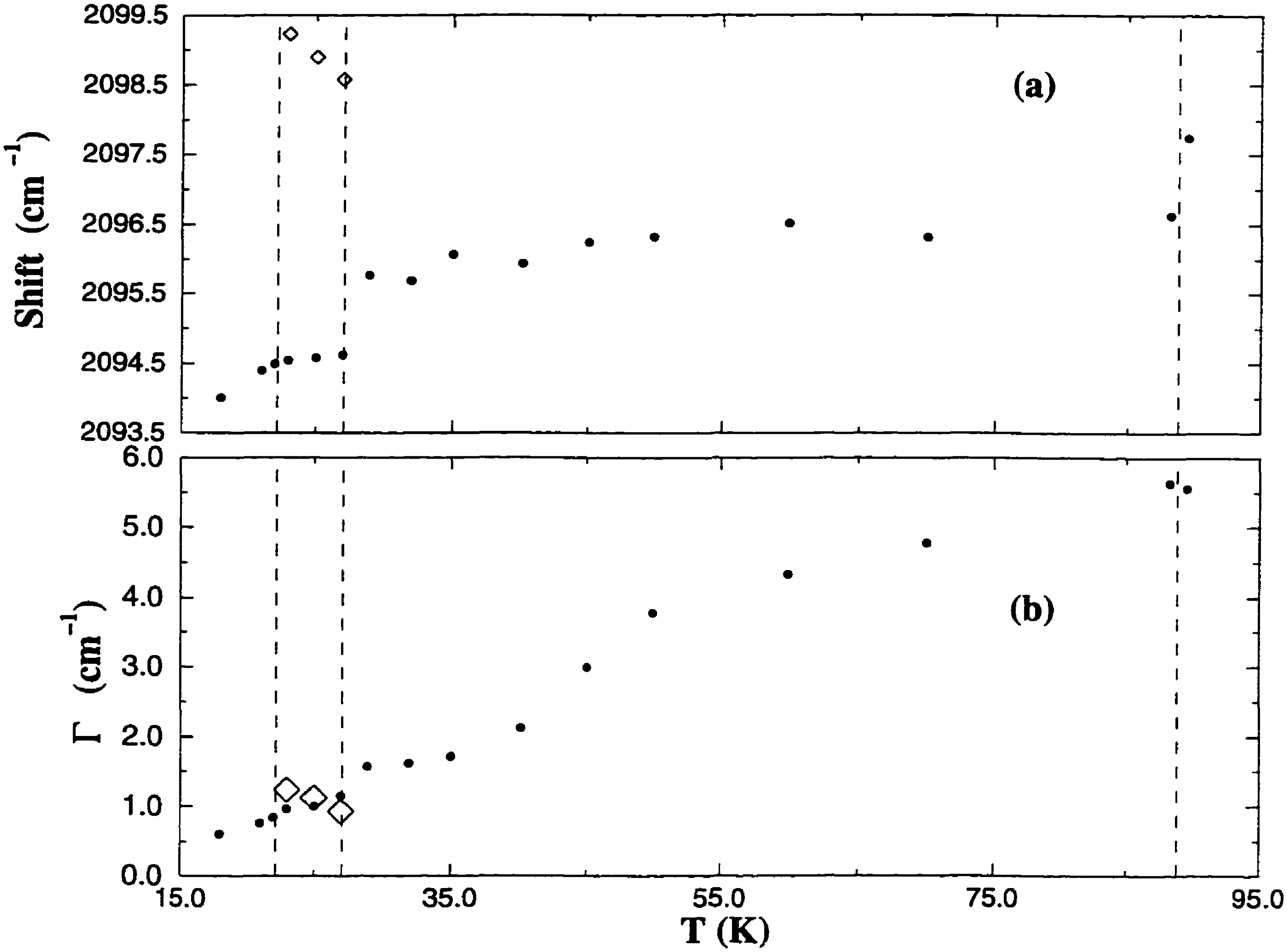

Figure 4.7: The shift (a) and full width at half height (b) of $\nu_1$ of $CD_4$ as a function of temperature. (◇) indicates the second peak which appeared after the first phase transition. The errors in measurements are comparable to the symbol size. The errors in measurements of FWHM are estimated to be ~ 2%. The dashed lines are positioned at the phase transition temperatures $T_c$=27.1 K and 22.1 K and at the liquid-solid phase boundary at 88.78 K.

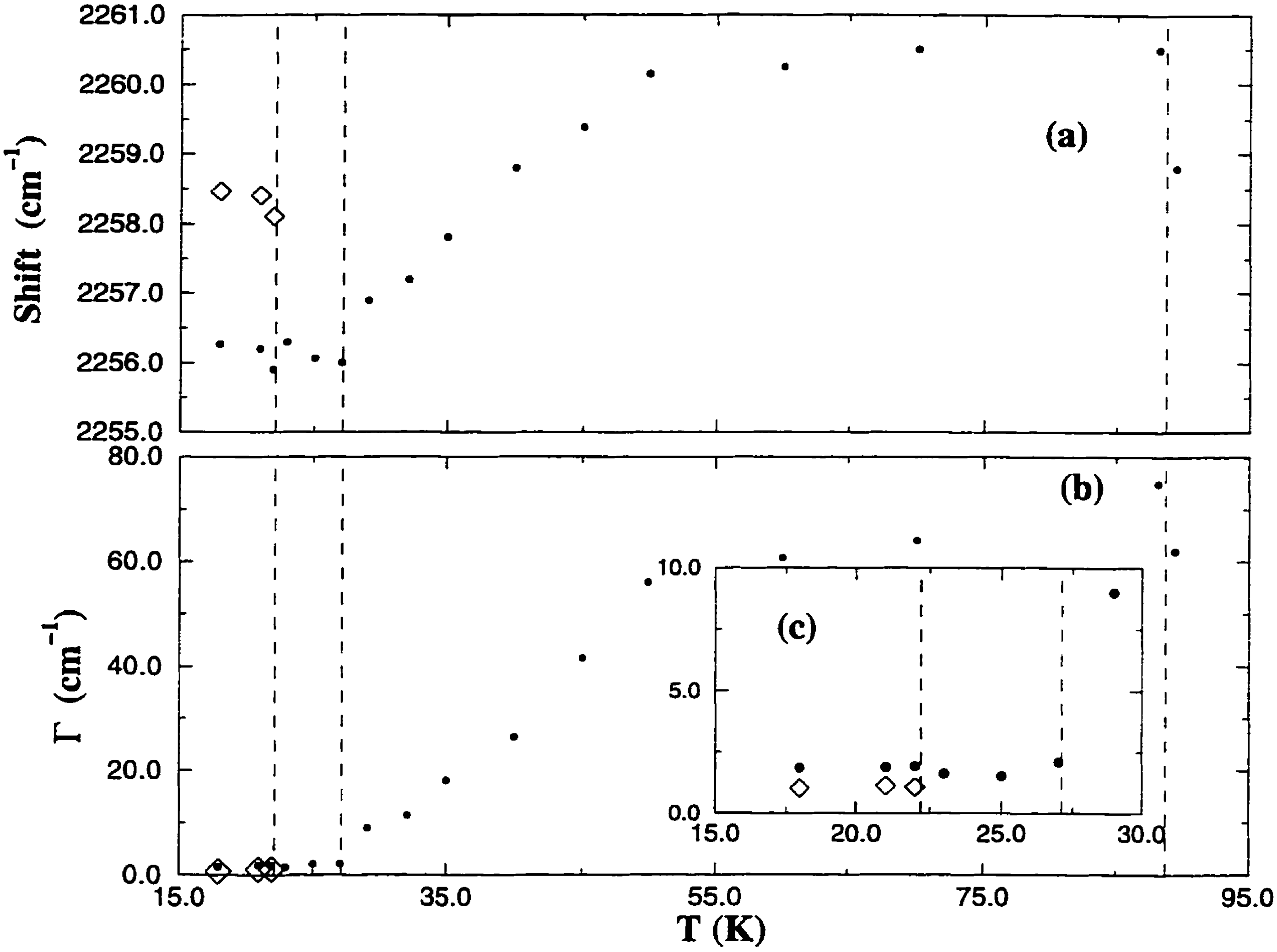

Figure 4.8: The shift (a) and full width at half height (b) of $\nu_3$ of $CD_4$ as a function of temperature. (◇) indicates the second peak which appeared after the second phase transition. The inset (c) shows a magnified view of FWHM around the phase transition temperature. The errors in measurements are comparable to the symbol size. The errors in measurements of FWHM are estimated to be ~ 2%. The dashed lines are positioned as in Fig. 4.7.

# Chapter 5

# Brillouin Measurements and Analysis for $CH_4$

## 5.1 Crystal Orientation and Refractive Indices

In order to conduct Brillouin experiments it is necessary to obtain information about crystal orientation, its density and refractive index. The crystal orientation can be obtained using x-ray scattering. This method utilizes a collimated polychromatic x-ray beam which, after diffraction within the crystalline sample, reveals the orientation of crystallographic planes in the laboratory reference frame. The crystals grown in this experiment have arbitrary orientation with respect to the laboratory coordinates but the scattering vector $\vec{q}\,(011)$ in the laboratory frame is defined by the geometry of the experiment. The orientations of the crystal axes usually are expressed in terms of Euler angles $(\theta, \phi, \chi)$. These angles are found by analyzing Lauē x-ray photographs. The x-ray source used in the experiment was a water-cooled Philips MO 100/Be 100 kv beryllium window tube operated at 70 kV and 10 mA. The x-ray beam is incident along the $y$-axis. The x-ray film was placed behind the cell, perpendicular to the $y$-axis. The photograph consists of a central round spot corresponding to the incident beam, for which the $x$-$y$ position on the photograph is assigned to be (0,0), and several small elliptical spots corresponding to the interference maxima of the diffracted x-ray from a set of Bragg planes, whose coordinates relative to the central spots are measured. Having measured the coordinates of the diffraction spots, the method of stereographic projection [133, 134, 135] can be used to determine the Euler angles. This method is based on projecting the relationship among the crystal planes in 3 dimensions onto two dimensions. The computerized procedure used for orientation was developed by Gammon [136]. The input of the program consists of the spots coordinates, the vectors determining the structure of the crystal and specified maximum error for calculating the interplanar angles. The output of the program consists of the Euler angles, the Miller indices and the errors associated with the least squares method applied to the orientation equation [136].

A rotation of the cryostat about its vertical axis corresponds to changing the $\phi$ angle while keeping $\theta$ and $\chi$ unchanged (within $\sim 1^0$ due to a small wobbling effect). After obtaining the orientation angles at different $\phi$ the set of Euler angles corresponding to all different $\phi$ can be determined .

Solid methane at low temperatures was studied using monochromatic x-ray scattering by at least two different groups [19, 137, 16]. These investigations revealed the lattice parameters of methane over a wide temperature range. With known lattice parameters the density could be easily calculated. The refractive index of solid methane at the triple point is known [18] and equal to 1.323. In order to calculate the refractive index at lower temperatures the Lorentz-Lorenz relation (obtained from the Clausius-Mosotti equation [110]) was used:

$$\frac{n^2-1}{n^2+2} = \frac{4}{3}\pi\alpha\frac{N_a}{V}. \tag{5.1}$$

Here $n$ is refractive index, $\alpha$ - polarizability, $N_a$ - Avogadro's number and V - molar volume. Multiplying both sides of this equation by the molar mass $M$, and assuming that polarizability $\alpha$ is constant over the investigated temperature range, Eq. 5.1 can be rewritten as

$$\frac{n_{tr}^2 - 1}{n_{tr}^2 + 2} = \frac{\rho_{tr}(n_x^2 - 1)}{\rho(n_x^2 + 2)} \tag{5.2}$$

where the subscript $_{(tr)}$ refers to the known density and refractive index at the triple point temperature , $_{(x)}$ refers to the temperature at which the refractive index is to be determined and $\rho$ is the density. Equation 5.2 was consequently used to determine the refractive index over the required wide temperature range.

## 5.2 Determination of Elastic Constants

Once the orientation, density and refractive index are known it is possible to calculate the acoustic velocity and frequency shifts in the directions corresponding to the scattering vector. The procedure starts with an initial guess for the elastic constants. The values of elastic constants are put into the Christoffel determinant Eq. 2.24 and then the determinant is solved, yielding the values for $\rho V^2$. The value for V is used to calculate the frequency shift using the Brillouin equation 2.15 and the calculated frequency is compared with the measured one. A least square fitting routine is applied to minimize the difference between the calculated and measured frequency shifts and as a result a set of elastic constants is obtained. The quantity $\chi^2$ which is minimized by the parameter searches through the elastic-constant space is determined by

$$\chi^2 = \frac{1}{N}\sum_{i=1}^{N}\left(\frac{\nu_i^{calc} - \nu_i^{obs}}{\sigma_i}\right)^2 \tag{5.3}$$

where N is the number of the observed shifts and $\sigma_i$ is the experimental uncertainty associated with each measurement. The number of observed shifts would usually vary from 18 to 25 depending on the number of different crystal orientations investigated (usually 7-10) and the number of transverse modes which were visible.

The minimizing was done by using standard computer subroutine libraries. Calculation of non-systematic errors, arising from the uncertainties in the Brillouin peaks, requires the knowledge of $\sigma_i$. The $\sigma_i$ was assumed to be between 0.01 to 0.09 GHz.

The systematic errors arise from uncertainties in the density, refractive index and the scattering angle. The systematic errors in $\rho V^2$ are calculated from the Brillouin equation and found to be $\sim$ 1%. The quoted errors in the elastic constants represent the standard deviation in the best fit parameters and uncertainties in the frequency shift and crystal orientation.

## 5.3 Results

### 5.3.1 Elastic Moduli

In phase I more than 15 independent crystals were studied. Only 3 were successfully cooled below the phase transition temperature. Because of the internal shattering the quality of spectra deteriorate with decreasing temperature. Also, because some orientations give better spectra than others, the spectra were measured in 5 or $10^0$ intervals through $70^0$ degrees in $\phi$. Typical Brillouin spectra of methane in both phases are shown in Fig. 5.1. The spectrum in phase I at 90 K (in Fig. 5.1(a)) was collected in 30-35 minutes. Both transverse peaks are visible and marked as $T_{(s,f)i}$, where $s$ stands for slow transverse peak and $f$ for fast and $i$ refers to which Rayleigh peak a given transverse peak belongs. The longitudinal peaks are marked $L_{(1,2)}$, where indices indicate the Rayleigh peak to which a given longitudinal peaks belongs. As temperature was decreased the intensity of Brillouin peaks would slightly decrease as well but the parasitic scattering coming from the internal cracks in the crystal would increase by the few orders of magnitude, thereby making the detection of the Brillouin peaks very difficult.

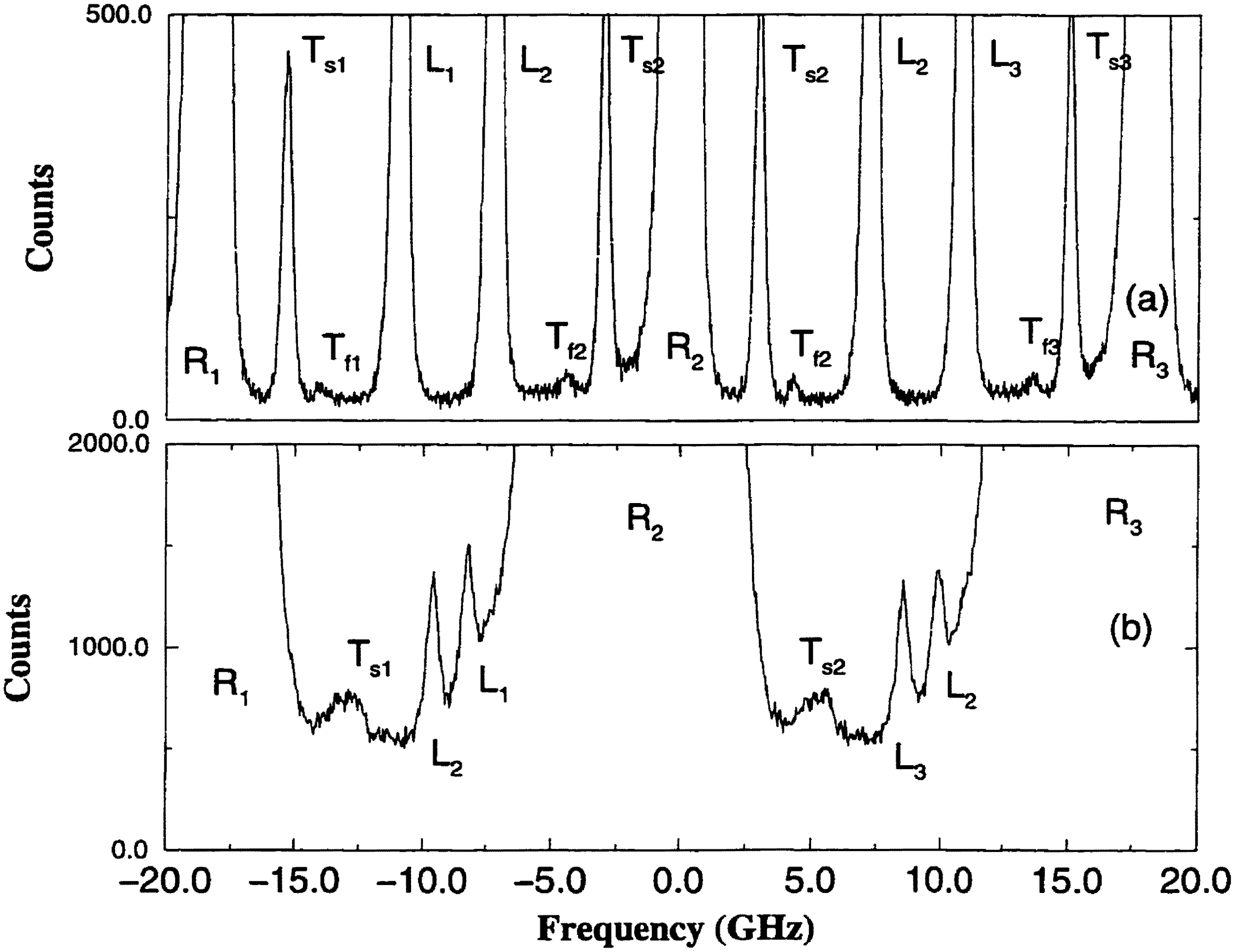

Figure 5.1: Representative Brillouin spectra of $CH_4$ in phases I (a) and II (b). The Rayleigh peaks are labeled $R_i$, longitudinal $L_i$, where $i$ is the number of corresponding Rayleigh and longitudinal peak. Transverse modes are labeled $T_{(s,f)i}$ where $s$,$f$ stand for slow and fast transverse modes and $i$ shows the Rayleigh peak to which a given transverse peak belongs.

A consequence of that is the time needed to collect Brillouin spectra in phase II (as in Fig. 5.1(b)) was usually on the order of 24-36 hours and very often the second transverse mode would not be visible at all.

After a final set of elastic constants was obtained, the frequencies of the acoustic modes versus rotation angle were calculated and compared with the measured ones. Figure 5.2 shows the difference between measured and calculated shifts.

The elastic constants of solid methane in both phases are listed in Table 5.1 and plotted vs. temperature in Fig. 5.3. The elastic constants around the phase transition are shown in Fig. 5.4. The solid circles are measured values of elastic constants which were fitted to the linear expressions shown as solid lines. It is interesting to notice that $C_{44}$ and $C_{11}$ have steeper slopes then $C_{12}$. As a result $C_{44}$ becomes comparable with $C_{12}$ at temperatures close to the phase transitions and in phase II. In phase II the slopes and values of $C_{12}$ and $C_{44}$ are almost equal although no firm conclusions can be made owing to the small number of experimental points. The functional dependencies of the elastic constants with temperature in phase I are:

$$C_{11}(T) = -0.15T + 34.02 \tag{5.4}$$

$$C_{12}(T) = -0.06T + 20.93 \tag{5.5}$$

$$C_{44}(T) = -0.13T + 20.41 \tag{5.6}$$

The combinations of elastic constants corresponding to the $< 110 >$ direction are shown in Fig. 5.5. The $\frac{1}{2}$($C_{11}$-$C_{12}$) and $C_{44}$ correspond to two shear moduli in the cubic phase [91].

With elastic constants known, the bulk modulus was calculated as:

$$B = \frac{1}{3}(C_{11} + 2C_{12}). \tag{5.7}$$

Table 5.1: Elastic constants of $CH_4$ in phase I and II in kbars. Temperatures are accurate to within ±0.2 K.

| T (K) | $C_{11}$ | $C_{12}$ | $C_{44}$ |
|---|---|---|---|
| | | Phase I | |
| 90.0 | 19.6 ± 0.2 | 14.8 ± 0.1 | 9.2 ± 0.1 |
| 70.0 | 23.8 ± 0.3 | 16.9 ± 0.3 | 11.5 ± 0.2 |
| 60.0 | 25.4 ± 0.2 | 17.7 ± 0.2 | 12.6 ± 0.2 |
| 54.0 | 26.7 ± 0.2 | 18.2 ± 0.2 | 13.3 ± 0.1 |
| 50.0 | 27.2 ± 0.2 | 18.3 ± 0.2 | 13.9 ± 0.1 |
| 48.1 | 26.7 ± 0.2 | 18.3 ± 0.2 | 14.1 ± 0.1 |
| 38.0 | 28.9 ± 0.3 | 19.4 ± 0.2 | 15.6 ± 0.2 |
| 30.0 | 29.7 ± 0.3 | 18.8 ± 0.2 | 15.8 ± 0.2 |
| 26.1 | 29.5 ± 0.3 | 19.4 ± 0.2 | 16.9 ± 0.2 |
| 25.0 | 30.2 ± 0.3 | 19.4 ± 0.2 | 16.7 ± 0.2 |
| 24.8 | 30.1 ± 0.3 | 19.3 ± 0.2 | 18.2 ± 0.2 |
| 23.0 | 30.0 ± 0.3 | 19.2 ± 0.2 | 16.5 ± 0.3 |
| 22.3 | 31.1 ± 0.3 | 19.0 ± 0.2 | 18.1 ± 0.2 |
| 21.3 | 30.4 ± 0.3 | 19.5 ± 0.3 | 18.6 ± 0.2 |
| 20.5 | 31.4 ± 0.3 | 19.8 ± 0.2 | 18.8 ± 0.2 |
| | | Phase II | |
| 19.3 | 30.9 ± 0.3 | 18.1 ± 0.2 | 19.3 ± 0.3 |
| 17.3 | 33.9 ± 0.3 | 19.0 ± 0.3 | 18.7 ± 0.3 |
| 15.5 | 34.0 ± 0.3 | 19.3 ± 0.2 | 19.4 ± 0.2 |

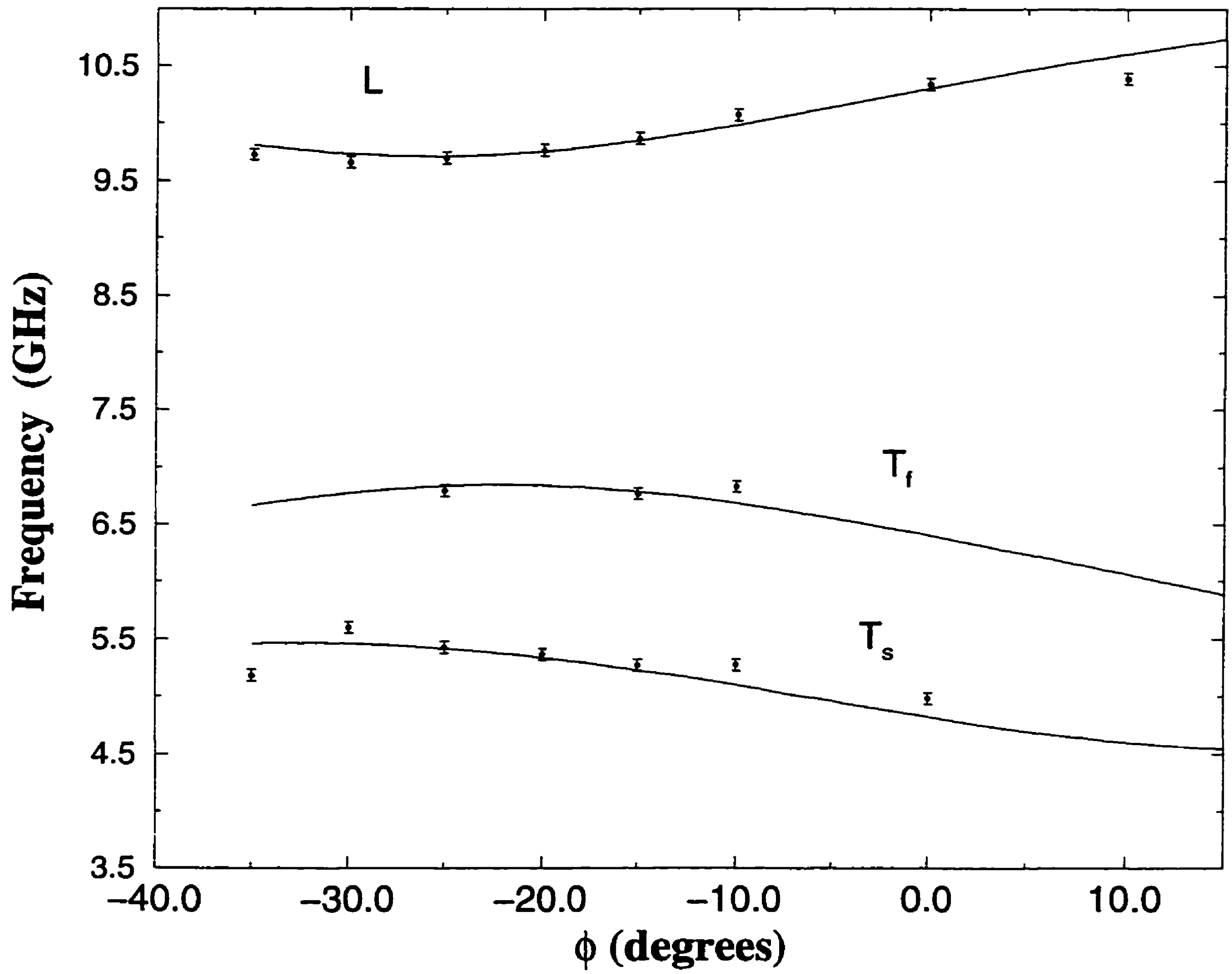

Figure 5.2: Calculated (solid lines) and measured (solid circles) frequency shifts of $CH_4$-I at 23 K.

The aggregate shear modulus (G) was obtained from the Voight-Reuss-Hill averaging method [138]. These parameters are shown in Fig. 5.6. The bulk modulus increases by a factor 1.5 and the shear modulus increases by a factor of $\sim 3$ within the investigated temperature range. There are no noticeable changes in the values of elastic moduli such as B, $(C_{11}-C_{12})/2$ and $C_{44}$ when the crystal goes through the phase transition (the phase transition was confirmed by the observation in changes of $\nu_1$ and $\nu_3$ of the vibrational Raman spectra of $CH_4$).

Lynden-Bell and Michel [76] have showed that softening of the elastic constants can happen by rotation-translation coupling at the $\Gamma$ point ($\vec{k}=0$) as a result of coupling to L=4 rotator function. They anticipated that the effect would be comparatively small due to the high values of L involved and it should not be affected by the phase transition. This is indeed what is observed in the present experiment, for example, relative to the RGS the softened elastic constants showed increasing values as temperature decreased and were not significantly dependent on the phase transition. It would be of particular interest to observe the behavior of the elastic constants close to the zone boundary where they should anomalously depend on the temperature.

The most profound changes happen to the anisotropy factor A,

$$A = \frac{2C_{44}}{C_{11} - C_{12}}, \tag{5.8}$$

and $\delta = (C_{12} - C_{44})/C_{12}$ (Fig. 5.7) which is a measure of the violation of the Cauchy relation $C_{44} = C_{12}$ [58]. The latter is a characteristic of central forces, and is usually well fulfilled for the rare gas solids. Across the measured temperature range both A and $\delta$ undergo large change from almost 0.4 and 4 for $\delta$ and A respectively, to $\pm 0.05$ and $\approx 2.5$. The anisotropy factor of $CH_4$ compared closely with the RGS after the phase transition takes place, and a small $\delta \approx 0$ suggests that the lattice dynamics can be represented by

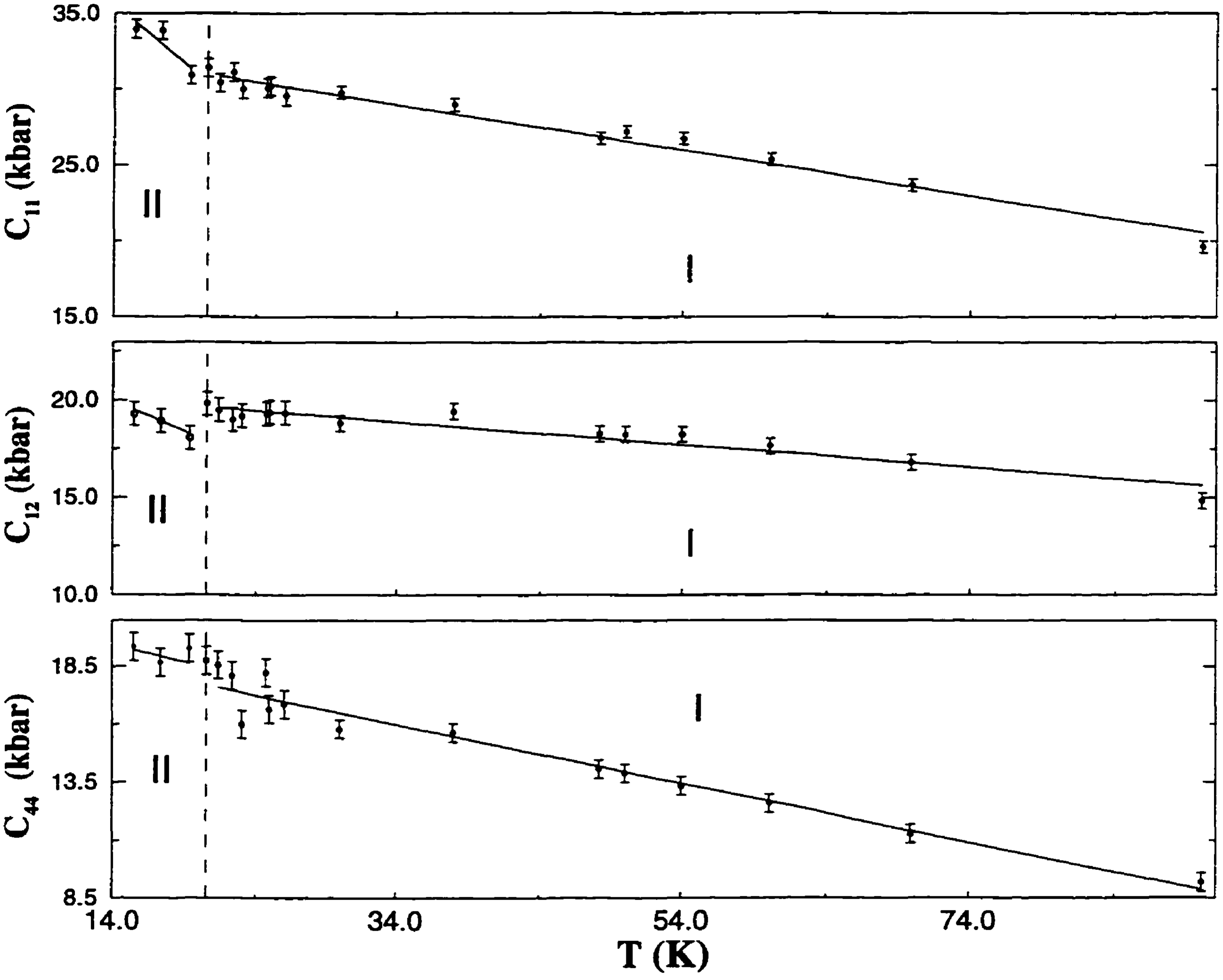

Figure 5.3: Elastic constants of $CH_4$ as a function of temperature over the investigated temperature range. The error bars shown represent the standard deviation in the best fit parameters and uncertainties in the frequency shift and crystal orientation. The dashed line is positioned at the phase transition temperature of 20.5 K. The solid lines in the phase II are drawn as guides to the eye only.

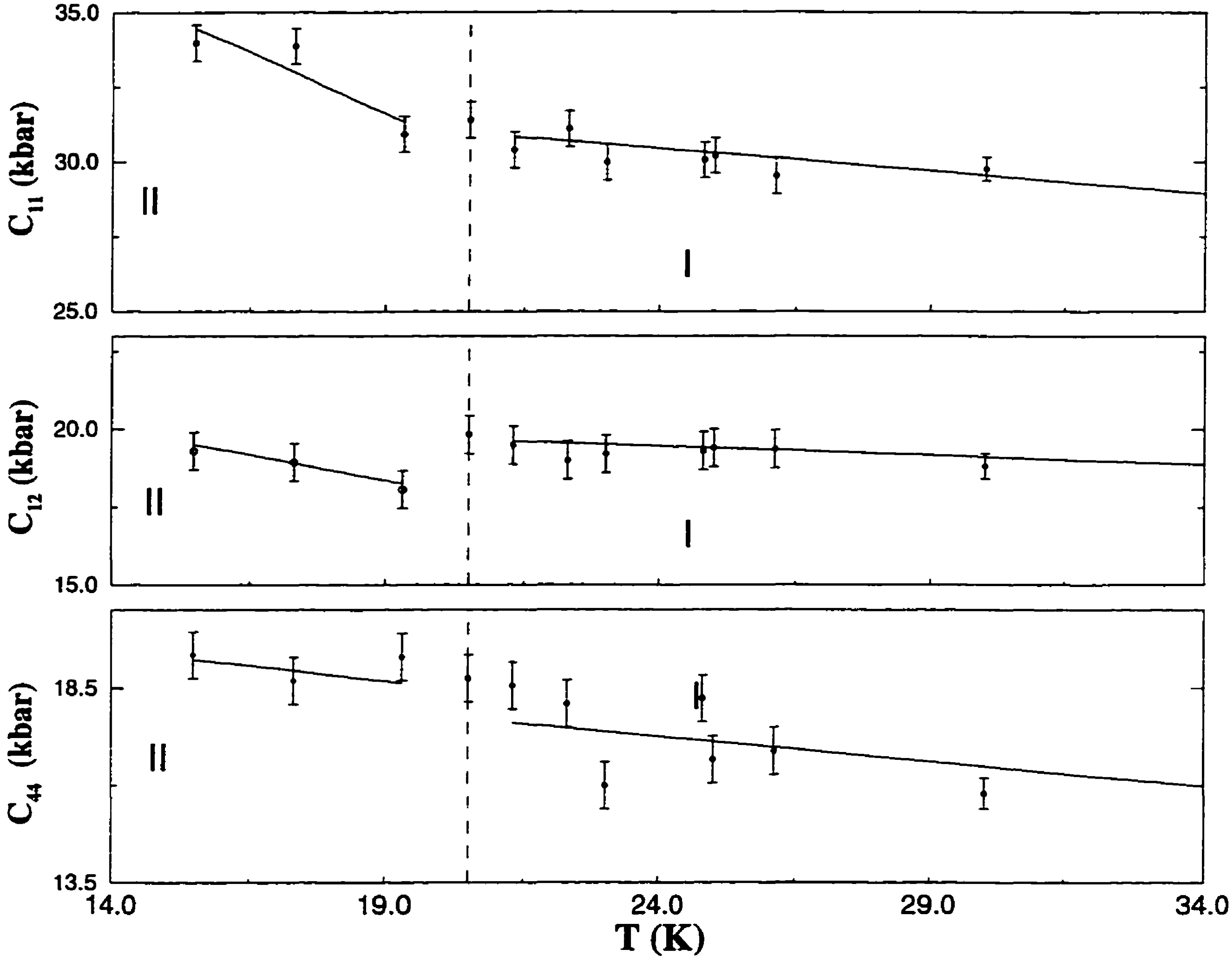

Figure 5.4: Elastic constants of $CH_4$ as a function of temperature around the phase transition temperature. The error bars shown are as in Fig. 5.3. The dashed line is positioned as in Fig. 5.3. The solid lines in the phase II are drawn as guides to the eye only.

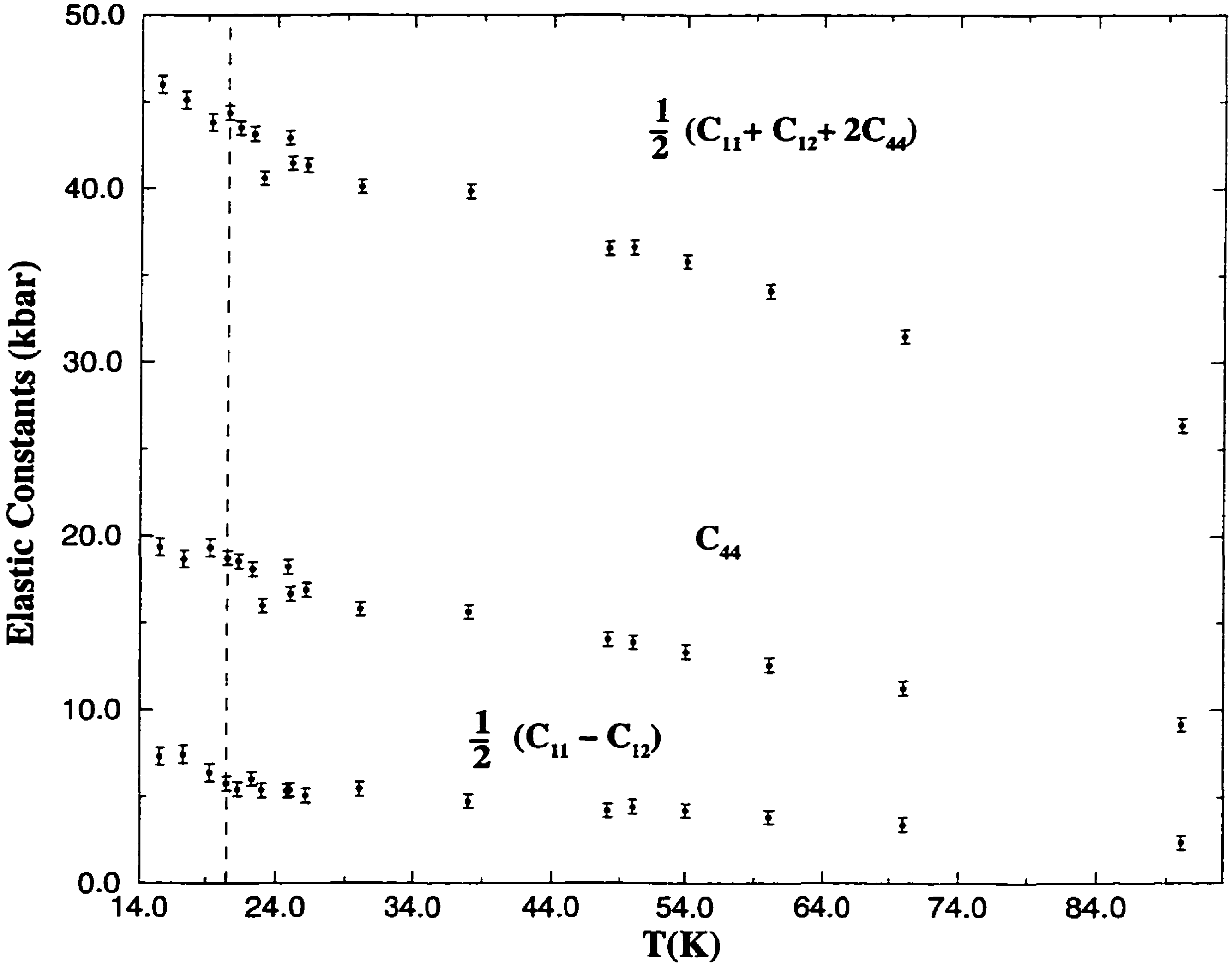

Figure 5.5: Elastic constants of $CH_4$ as a function of temperature. The combinations correspond to the longitudinal and two transverse waves in the < 110 > direction. The error bars shown are from the errors in elastic constants as in Fig. 5.3. The dashed line is positioned as in Fig. 5.3.

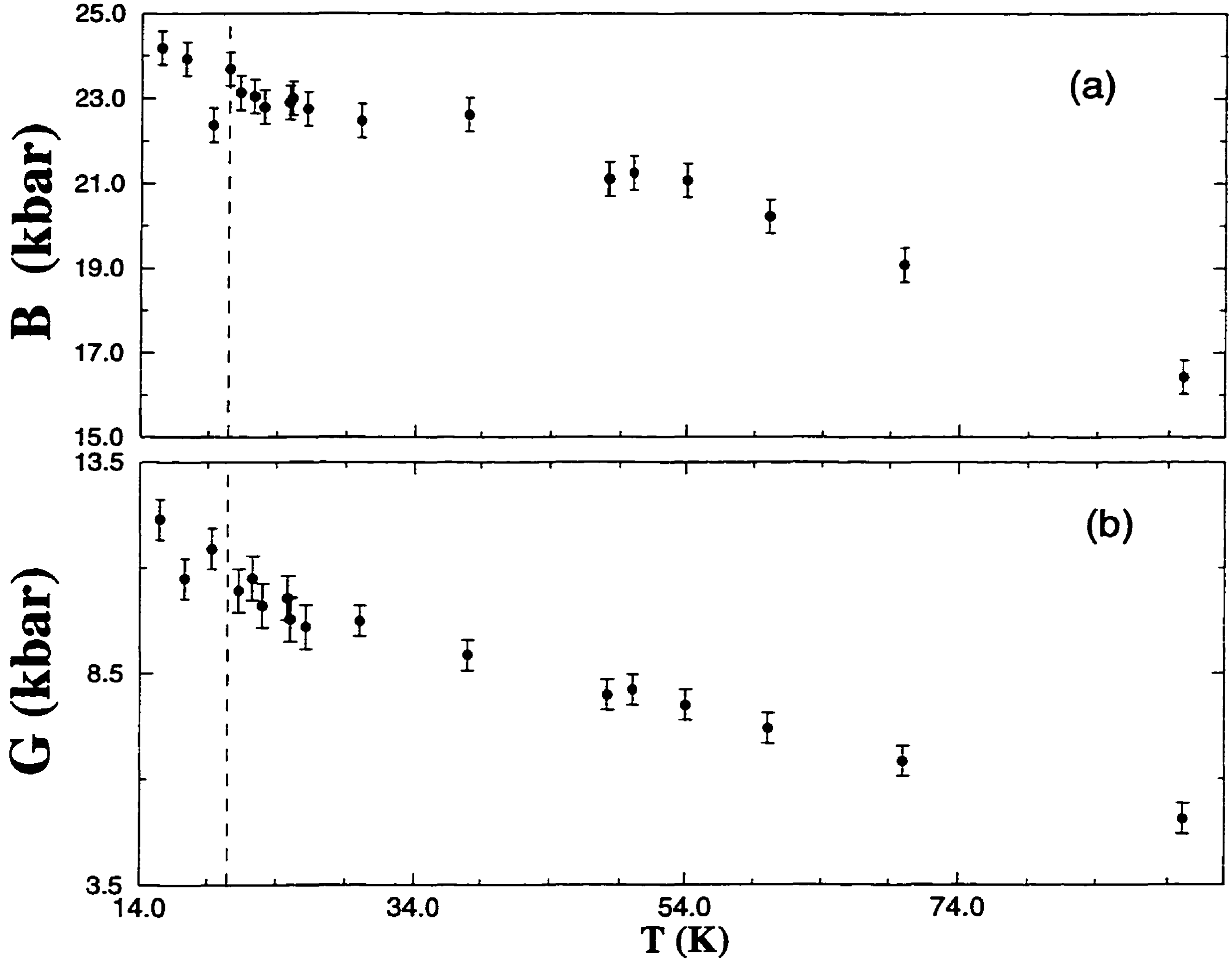

Figure 5.6: Elastic moduli of $CH_4$ as a function of temperature: bulk modulus (a), shear modulus (b). The error bars shown are from errors in elastic constants as in Fig. 5.3. The dashed line is positioned as in Fig. 5.3.

a nearest neighbor central forces.

With the whole set of elastic constants determined, acoustic velocity distributions can be calculated in any direction. The acoustic velocities in (100) and (110) planes in both phases are shown in the Fig. 5.8 and Fig. 5.9. Although $C_{44}$ becomes equal to $C_{12}$ the velocity distribution does not change too much but it becomes more isotropic in the phase II.

The Poisson ratio was calculated using the expression

$$\sigma = \frac{(V_l^2 - 2V_t^2)}{2(V_l^2 - V_t^2)} \tag{5.9}$$

where $V_l$ and $V_t$ are the values averaged over the reciprocal velocity surfaces. The temperature dependence of the Poisson ratio is shown in Fig. 5.10(a) and compared with Poisson ratio from Ref. [139].

### 5.3.2 Thermodynamic Properties

At each temperature, the mean velocity $V_{av}$ was computed by averaging over the three reciprocal velocity surfaces:

$$\frac{3}{V_{av}^3} = \int [\frac{1}{V_l^3} + \frac{1}{V_{t1}^3} + \frac{1}{V^3{}_{t2}}] d\Omega \tag{5.10}$$

where $\Omega$ is an element of solid angle. The Debye temperature is than obtained as

$$\theta_D = (\frac{6\pi^2 N}{V})^{\frac{1}{3}} \frac{\hbar V_{av}}{k_B}, \tag{5.11}$$

where h is Planck's constant, $k_B$ is Boltzmann's constant, N is the number of molecules in crystal and V is molar volume [140]. The Debye temperature vs. temperature is shown in Fig. 5.10(b). Also shown, is the Debye temperature obtained on the basis of x-ray measurements from Ref. [16]. The Debye model is usually applied to the harmonic crystals such as the RGS. Because of the similarities between methane and the

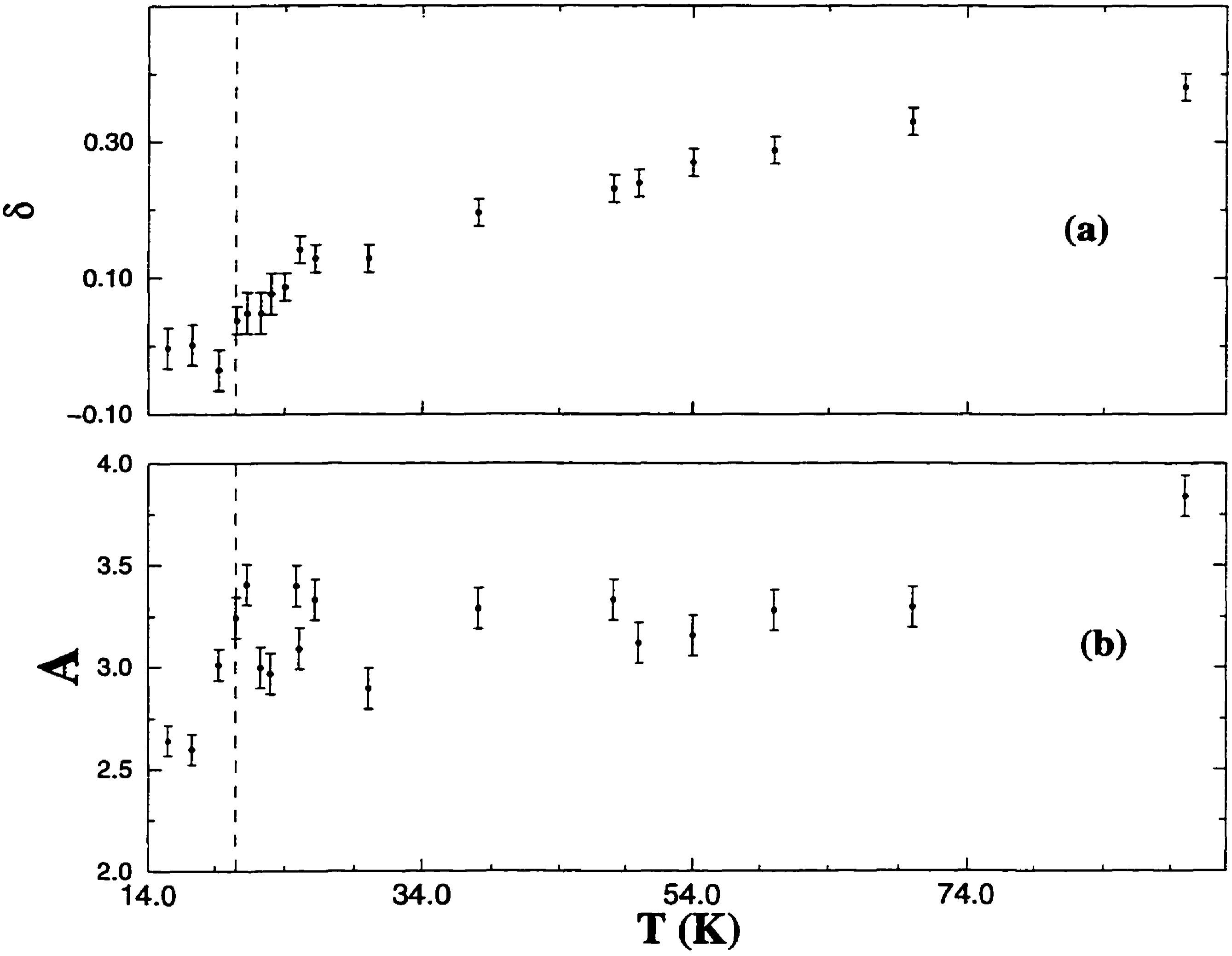

Figure 5.7: (a) $\delta=(C_{12}\text{-}C_{44})/C_{12}$ of $CH_4$ as a function of temperature. (b) Anisotropy factor A of $CH_4$ . The error bars shown are from the errors in elastic constants as in Fig. 5.3. The dashed line is positioned as in Fig. 5.3.

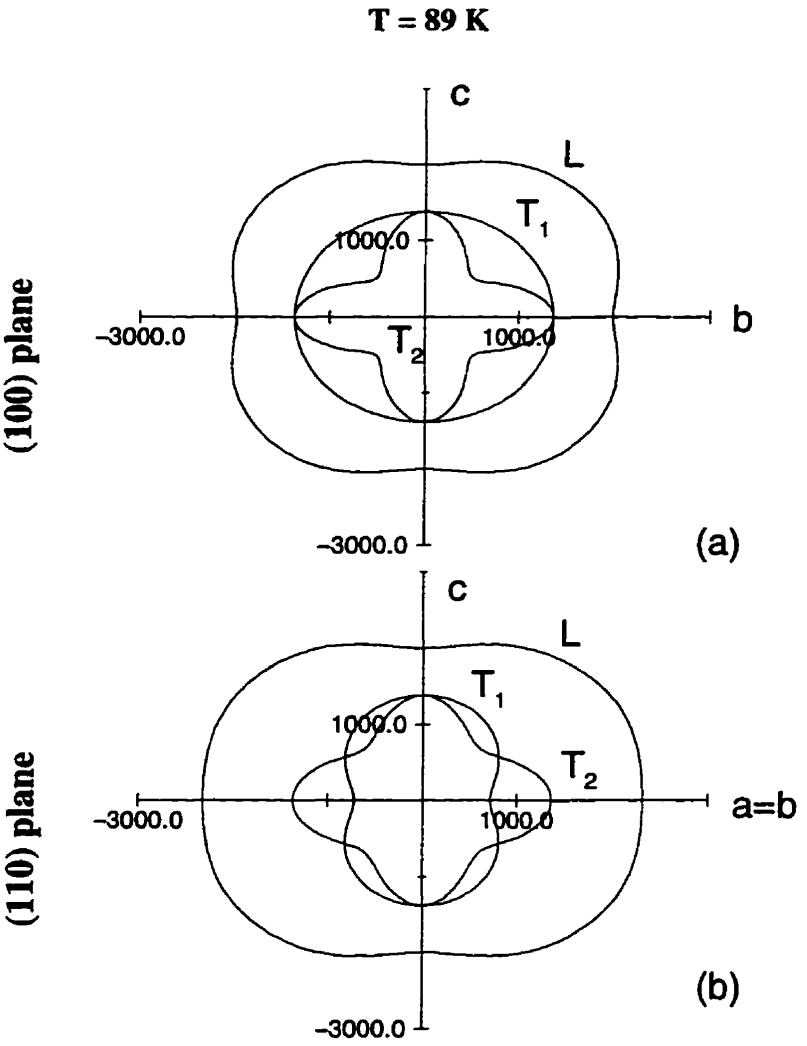

Figure 5.8: Acoustic velocities of $CH_4$ (in $ms^{-1}$) in high symmetry planes in phase I at 89 K. (a) (100) plane. (b) (110) plane.

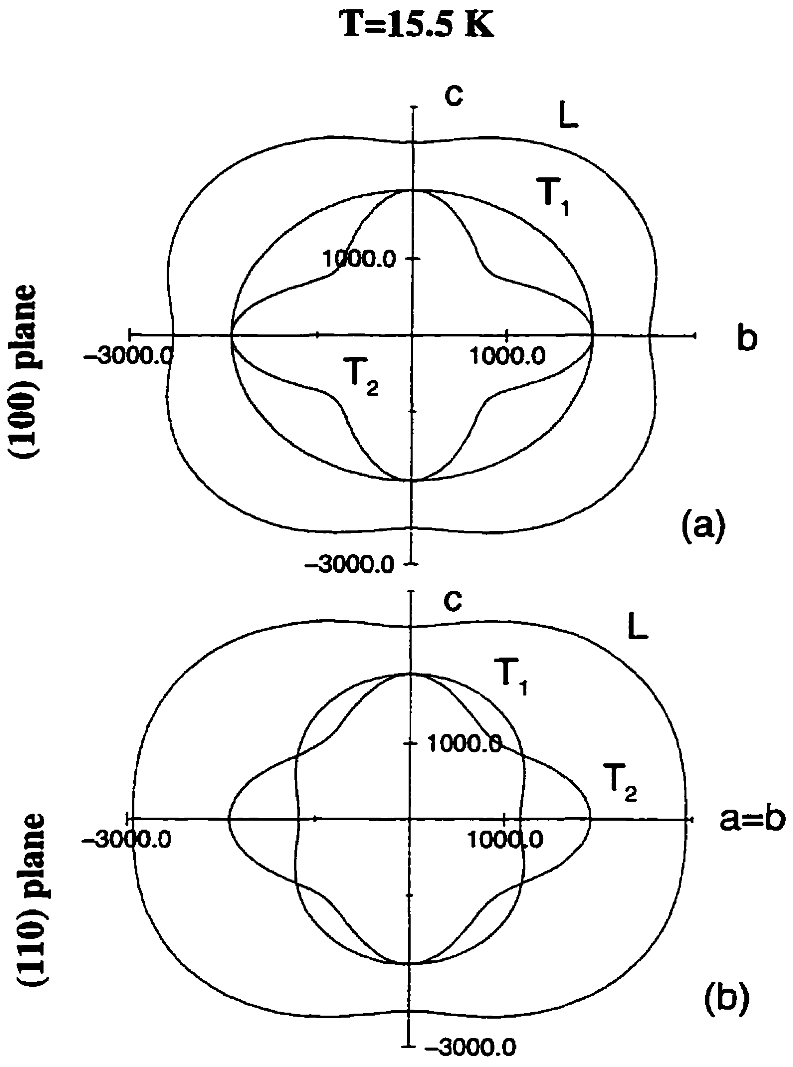

Figure 5.9: Acoustic velocities of $CH_4$ (in $ms^{-1}$) in high symmetry planes in phase II at 15.5 K. (a) (100) plane. (b) (110) plane.

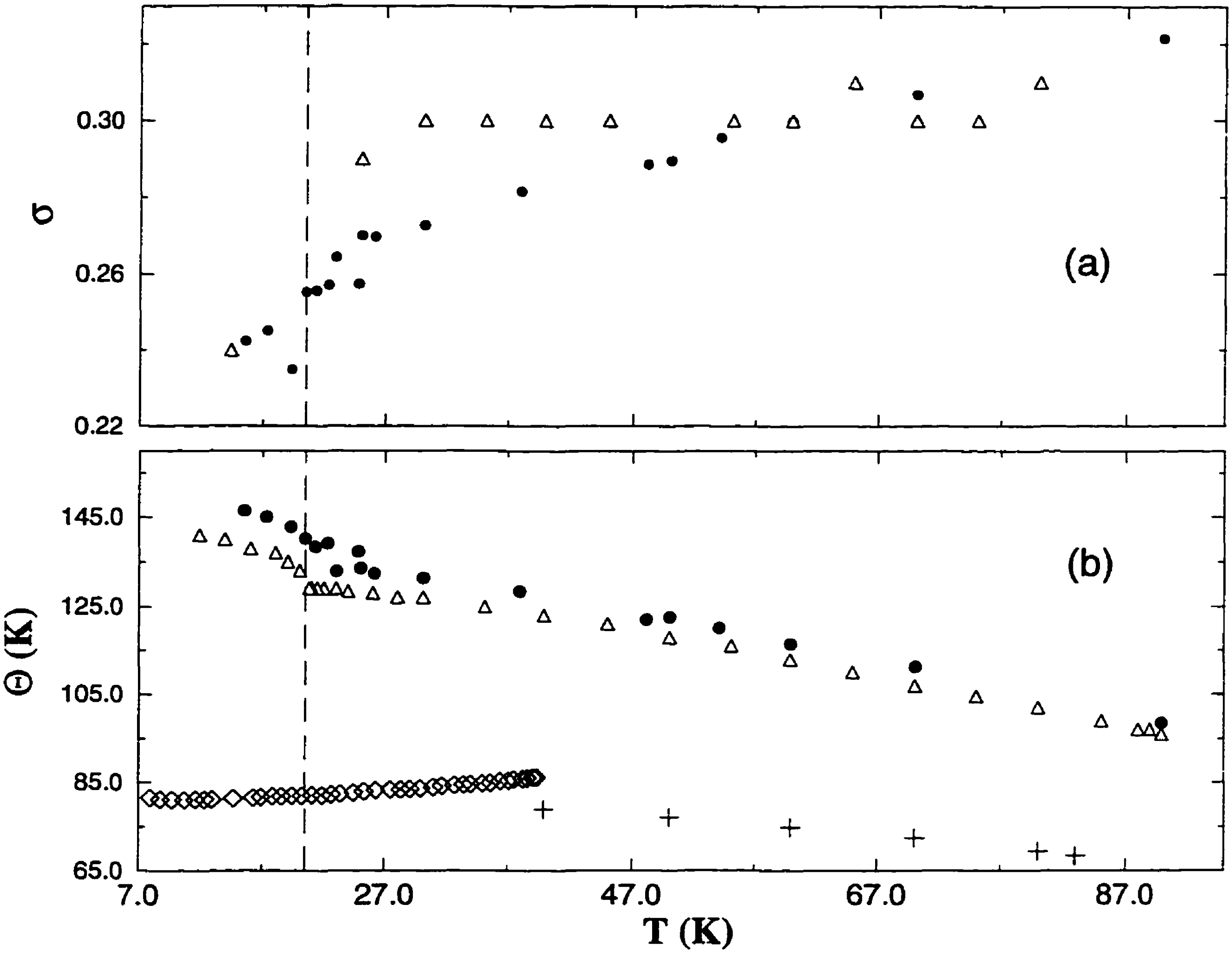

Figure 5.10: (a) Poisson ratio ($\sigma$) of $CH_4$. The ($\Delta$) are from Ref. [139]. (b) Debye temperature of solid $CH_4$ (●). Compared with results ($\Delta$) from Ref. [16] and (◇) Debye temperature of solid argon from Ref. [141] and (+) Ref. [142]. The dashed line is positioned as in Fig. 5.3.

RGS it is of interest to also apply the Debye model in the present case. It can be seen from Fig. 5.10 that the values of the Debye temperature obtained in this experiment are consistently higher then in Ref. [16] but follow the general pattern over the whole temperature range.

From the Debye temperature, the lattice specific heat at constant volume, $C_v$, was obtained by integrating the Debye function. The temperature dependency of the lattice specific heat is shown on Fig. 5.11 and compared with corresponding heats of argon and krypton.

With all the data available it is possible to calculate the Grüneisen parameter, $\gamma$, and the specific heat of rotational motion, $C_{rot}$, of the methane molecules. The specific heat at constant pressure, $C_p$, was directly measured by Colwell *et al.* (see Ref. [14]). The coefficients (linear and volume) of thermal expansion were measured as well (see Ref. [16].) Using thermodynamic relations such as:

$$\gamma = \frac{\beta B_s V}{C_p} \tag{5.12}$$

(where $\beta$ and $B_s$ are volume coefficient of thermal expansion [16] and adiabatic bulk modulus, respectively, as measured in the present work) and

$$C_p - C_v = \frac{\beta^2 V T}{\chi_T} \tag{5.13}$$

(where $\chi_T$ is the isothermal compressibility), $\gamma$ and $C_{rot}$ could be calculated. A plot of $\gamma$ vs. temperature is shown in Fig. 5.12. It can be seen that it is virtually independent of temperature in phase I and on average is equal $\gamma \sim 1.85$ which is in a good agreement with $\gamma \sim 1.82$ obtained in Ref. [18].

Figure 5.13 shows the temperature dependence of $C_{rot}$ obtained by subtracting $C_v$ of the lattice from the total specific heat. It should be noted however, that this procedure

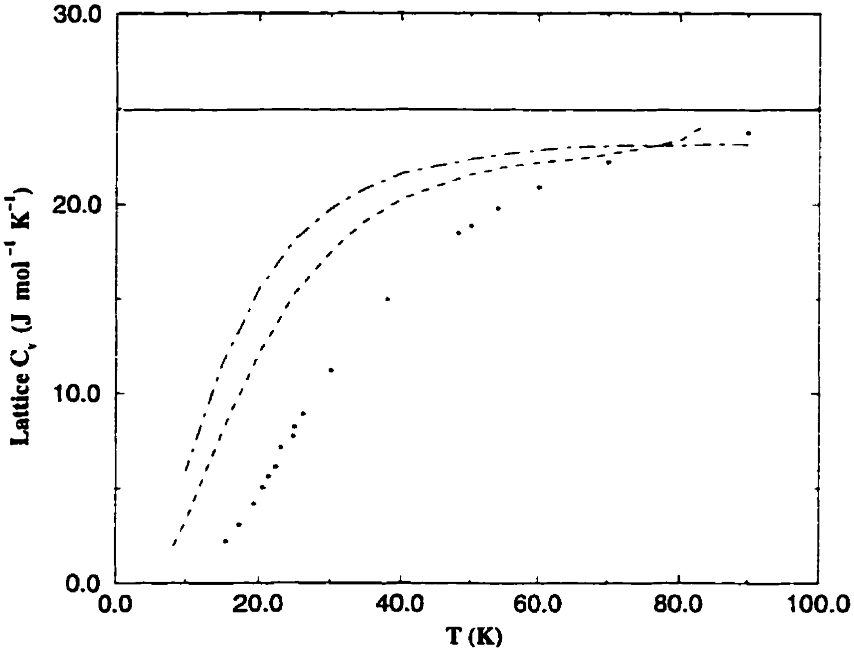

Figure 5.11: The lattice specific heat of $CH_4$ (●). Compared with $C_v$ of argon (- - -) and krypton (- ·- ·- ·) from Ref. [143, 144, 145]. The solid line is positioned at 3R.

assumes that there is no connection between rotational and translational movement of the molecules. But because of the RT coupling the rotational specific heat in most of phase I is lower then $\frac{3}{2}$R, which is characteristic of the free rotational specific heat.

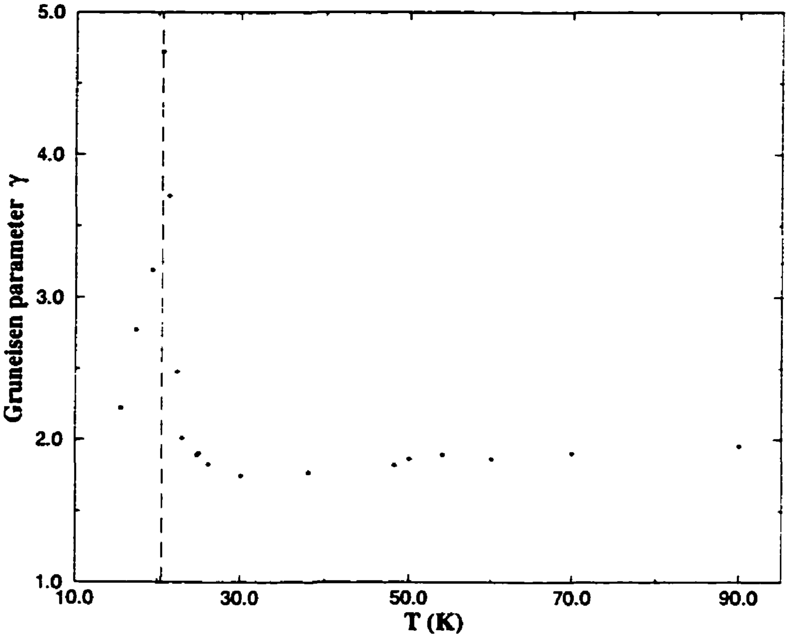

Figure 5.12: The Grüneisen parameter of $CH_4$. The dashed line is positioned as in Fig. 5.3.

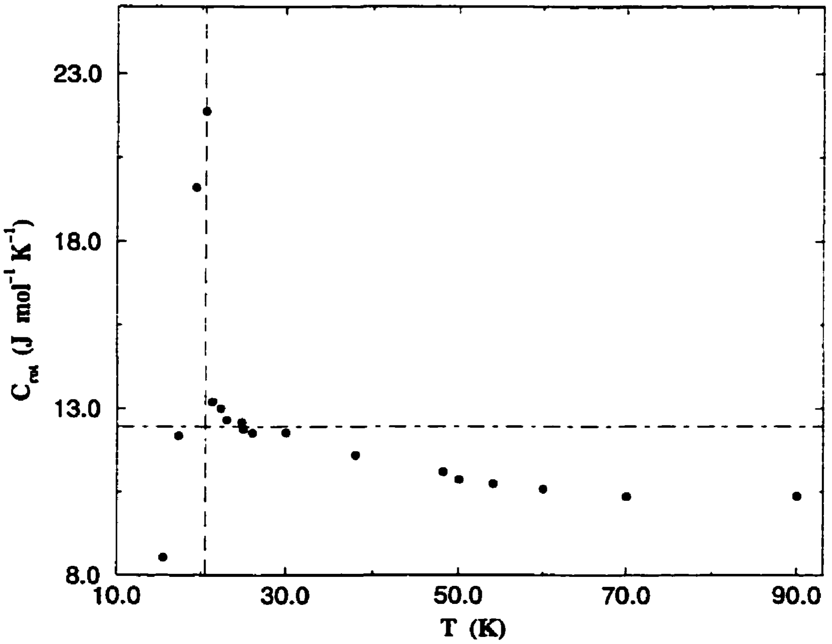

Figure 5.13: Rotational specific heat of $CH_4$ as a function of temperature. (- · - · - ·) line is positioned at $\frac{3}{2}$R. The dashed line is positioned as in Fig. 5.3.

# Chapter 6

# Brillouin Measurements and Analysis for $CD_4$

## 6.1 Crystal Growth of $CD_4$

The investigation on heavy methane was initiated after both phases of $CH_4$ were successfully studied [146, 147] and the technique allowing the cooling of single crystals below phase transition temperatures was developed and refined. Heavy methane presents a bigger challenge because of the existence of the second phase transition at $T_c$=22.1 K. This low temperature phase is tetragonal, meaning that some changes, needed to modify the cubic structure to tetragonal, are taking place. These changes are accompanied by a total volume change of $\sim$ 11% in the range from 10 to 89 K [17]. Such a change in volume will lead to mechanical strain and probably to a deterioration of the sample quality.

The apparatus and techniques used in the experiments with $CD_4$ are essentially the same as those described in chapter III. Over the course of the experiments more than 30 crystals were grown and cooled to the different temperatures, but only one was successfully cooled below the second phase transition temperature. All the problems mentioned above and described in chapter III also apply in this case. Crystals of deuteromethane tend to become "milky" if the gap between the surface of the crystal and the walls of the cell is too big, and they tend to change orientation more often than the crystals of $CH_4$ if the first stage of cooling is stopped at 60 K. In most cases, the change of orientation would lead to the polycrystallization of the sample. It was possible to get data between 60 and 70 K by collecting a few Brillouin spectra within several hours before the crystal

Table 6.1: Density and refractive Indices of $CH_4$ and $CD_4$

| T (K) | $CH_4$ | | $CD_4$ | |
|---|---|---|---|---|
| | $\rho$ ($g\ cm^{-3}$) [1] | n | $\rho$ ($g\ cm^{-3}$) [2] | n |
| 89.0 | 0.4906 | 1.323 [3] | 0.6169 | 1.321 [3] |
| 70.0 | 0.5031 | 1.332 | 0.6361 | 1.332 |
| 60.0 | 0.5087 | 1.336 | 0.6449 | 1.337 |
| 55.0 | 0.5112 | 1.338 | 0.6490 | 1.339 |
| 50.0 | 0.5136 | 1.340 | 0.6529 | 1.349 |
| 40.0 | 0.5178 | 1.343 | 0.6601 | 1.345 |
| 30.0 | 0.5213 | 1.346 | 0.6655 | 1.349 |
| 28.0 | 0.5219 | 1.346 | 0.6679 | 1.350 |
| 27.0 | | | 0.6706 | 1.352 |
| 25.0 | 0.5231 | 1.347 | 0.6731 | 1.353 |
| 23.0 | 0.5234 | 1.347 | 0.6745 | 1.354 |
| 22.0 | 0.5238 | 1.348 | 0.6793 | 1.357 |
| 21.0 | 0.5245 | 1.348 | 0.6800 | 1.357 |
| 19.0 | 0.5279 | 1.351 | | |
| 18.0 | | | 0.6816 | 1.358 |
| 17.0 | 0.5292 | 1.351 | | |
| 15.0 | 0.5296 | 1.352 | | |

changed orientation or became opaque. In order to collect spectra at lower temperatures the crystal had to be cooled from the triple point temperature to at least 50 K within 3-4 hours. The cooling to the lower temperatures was essentially the same as in the case of $CH_4$.

### 6.1.1 Density and Refractive Indices of $CD_4$

As in the case of $CH_4$ the orientation of the crystal relative to the laboratory frame, its density, and its refractive index are needed in order to calculate the elastic constants of heavy methane. The procedure for determination of orientation of the crystals of $CD_4$

---

[1] Ref. [16]

[2] Ref. [17]

[3] Ref. [18]

is exactly the same as described in the previous chapter and includes the taking of the x-ray photographs and calculating the Euler angles on the basis of the diffraction spot positions.

The density of solid $CD_4$ was measured and reported by others [20, 17]. Using these data and the Lorentz-Lorenz relation Eq. 5.1, the refractive indices for $CD_4$ were calculated over the needed temperature range. The values of density and refractive indices used in calculation of elastic constants, Debye temperature and specific heats of $CH_4$ and $CD_4$ are listed in Table 6.1.

## 6.2 Results

### 6.2.1 Elastic Moduli

After the best-fit set of elastic constants at every temperature was obtained it was used to generate theoretical curves of frequency shifts versus angle $\phi$. These curves were compared with the measured points as in Fig. 6.1. In the same crystal the frequency distribution pattern was the same at different temperatures in phases I and II. The phase transition between phases I and II was easily detected by comparatively big Brillouin shift changes for longitudinal and transverse modes and, as in case of $CH_4$, by analyzing the Raman spectra. These changes were more pronounced and could indicate that rotational-translational coupling is stronger in $CD_4$ than in $CH_4$, where the changes of Brillouin shifts were not so obvious and the occurrence of the phase transition could only be positively confirmed by the changes in the Raman shifts. The Brillouin shift pattern also changed slightly when the second phase transition took place. An interesting fact is that this happened ~0.9 K above the phase transition temperature of 22.1 K where the Raman spectra did not show that the transition had occurred. Consequently the elastic constants were first calculated at 23.0 K with the assumption that the structure was still cubic. However, the fits were not good and the values of the elastic constants were very different from the values at 25 K. The elastic constants were then calculated for 23 K and all temperatures below using fits corresponding to the tetragonal structure. Structures of tetragonal symmetry are known to have 7 elastic constants for classes 4, $\bar{4}, 4/m$ (lower symmetry) or 6 elastic constants for classes $4mm$, 422, $\bar{4}2m$ and $4/mmm$ (higher symmetry).

To the author's knowledge, however, no information exists on the space group of phase III. Therefore elastic constants have been calculated assuming both of the above possibilities with initial guesses for $C_{11}$, $C_{12}$ and $C_{44}$ equal to the values of corresponding constants at the higher temperatures and values of $C_{33}$, $C_{13}$ and $C_{66}$ equal to the values of $C_{11}$, $C_{12}$ and $C_{44}$ correspondingly. At all temperatures the fits for higher symmetry classes were better, and produced more consistent values for the resulting elastic constants. Figure 6.2 shows frequency shifts versus rotational angle $\phi$ at temperature T=23 K. The solid lines were calculated for the case of higher symmetry and the dotted lines for the case of lower symmetry. In both cases the agreement between calculated and measured shift is reasonably good for the range of angles where the measurements were taken. In both cases the theoretical shifts were calculated beyond the experimentally accessible range of angles and it could be seen that, in the case of lower symmetry, the angle distribution of the frequency of the slow transverse mode goes through an abrupt minimum, reaching almost zero at $\phi$ values of about $\sim -60^0$ and $105^0$. The curves shown in Fig. 6.2 were calculated with the elastic constants (in kbar) as follows:

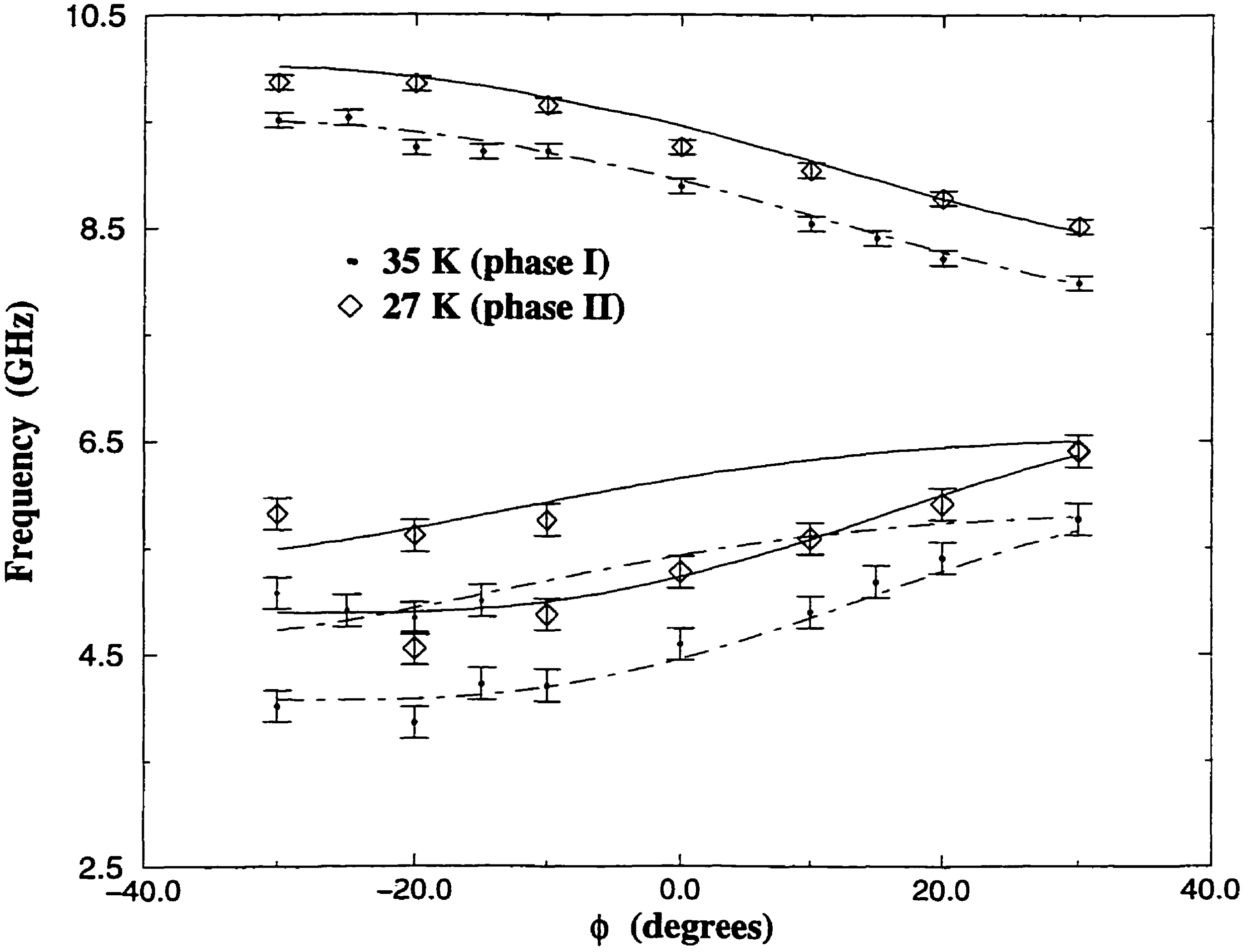

Figure 6.1: Frequency shifts in $CD_4$ as a function of temperature. The symbols show measured shifts as a function of angle $\phi$. Solid and dot-dashed curves are obtained from the best-fit elastic constants at each temperature.

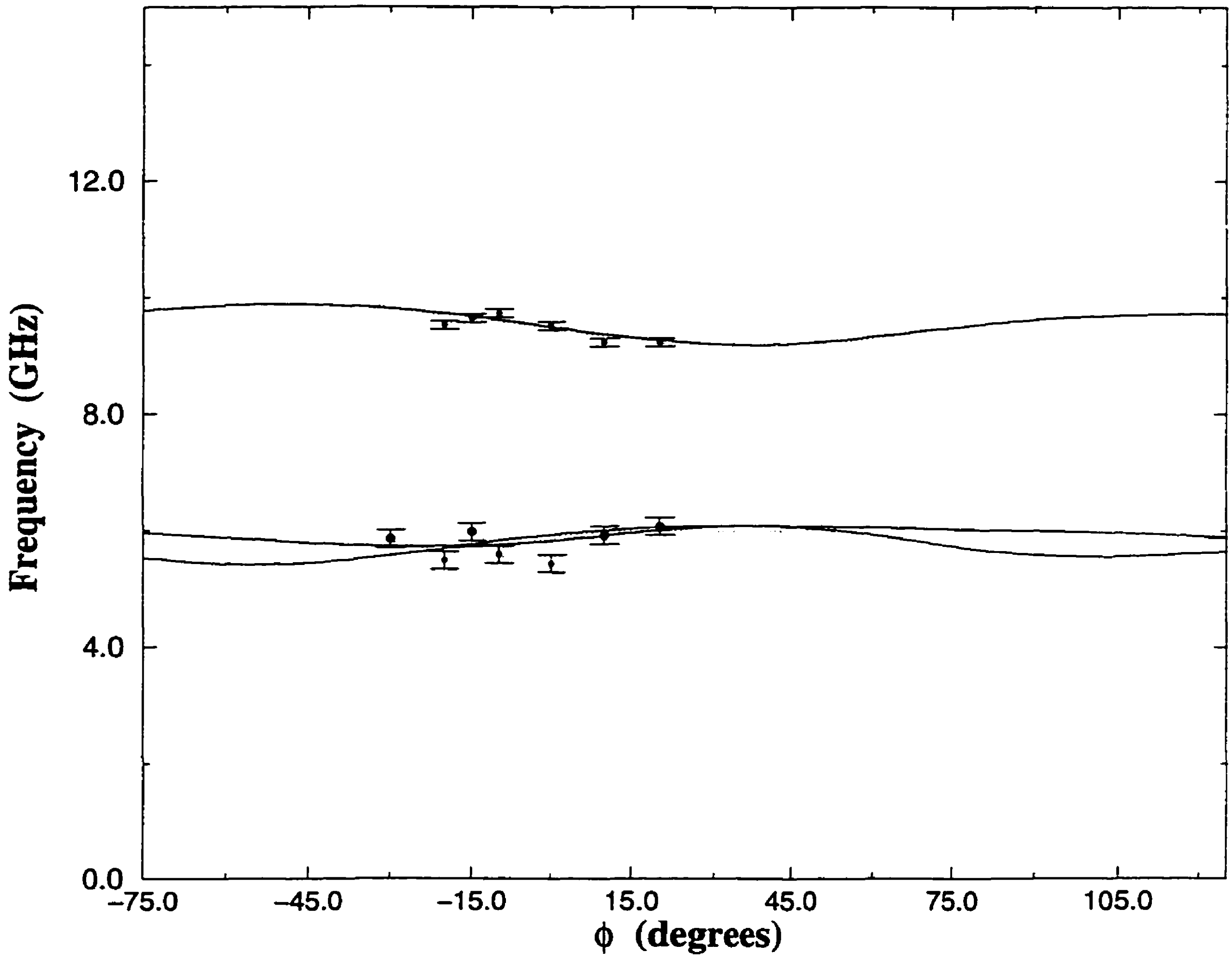

Figure 6.2: Frequency shifts in $CD_4$ - III versus rotational angle $\phi$ at T=18 K. The solid curves are for the symmetry classes $4mm$, 422, $\bar{4}2m$ and $4/mmm$. The dotted curves are for classes 4, $\bar{4}$, $4/m$.

| *Elastic const.* | $4mm, 422, \bar{4}2m, 4/mmm$ | $4, \bar{4}, 4/m$ |
|---|---|---|
| $C_{11}$ | 38.76 | 63.57 |
| $C_{12}$ | 19.87 | 41.38 |
| $C_{44}$ | 17.60 | 17.49 |
| $C_{33}$ | 39.55 | 39.91 |
| $C_{66}$ | 9.45 | −11.91 |
| $C_{13}$ | 12.33 | 11.24 |
| $C_{16}$ | – | −2.98 |

The values of such elastic constants as $C_{11}$ and $C_{12}$ in the case of lower symmetry are too high compared with the values in cubic phase at higher temperature of 25 K. Also, in the lower symmetry case, $C_{66}$ is negative which contradicts the stability condition [148]. It was consequently concluded that the higher symmetry classes are the appropriate choice.

The values of the elastic constants over the investigated temperature range are listed in the Table 6.2 and shown in Fig. 6.3, 6.4 and 6.5. The solid circles are measured values of elastic constants which were fitted to the linear expressions shown as solid lines. As in the case of $CH_4$, $C_{44}$ and $C_{11}$ have steeper slopes than $C_{12}$, and $C_{44}$ becomes comparable with $C_{12}$ at temperatures close to the first phase transition and in phases II and III. Although both phase transitions are clearly seen in the behavior of $C_{11}$ and $C_{44}$, the changes of these elastic constants are fairly small. The functional dependencies of the elastic constants with temperature in phase I are very close to those of $CH_4$ and equal to :

$$C_{11}(T) = -0.17T + 36.02 \tag{6.14}$$

$$C_{12}(T) = -0.05T + 20.81 \tag{6.15}$$

$$C_{44}(T) = -0.14T + 21.69 \tag{6.16}$$

Table 6.2: Elastic constants of $CD_4$ in phase I, II and III in kbars. Temperatures are accurate to within ±0.2 K.

| T | $C_{11}$ | $C_{12}$ | $C_{44}$ | $C_{33}$ | $C_{13}$ | $C_{66}$ |
|---|---|---|---|---|---|---|
| | | | Phase I | | | |
| 88.2 | 20.6±0.2 | 15.3±0.1 | 9.5±0.1 | - | - | - |
| 70.0 | 23.9±0.2 | 17.0±0.2 | 11.8±0.1 | - | - | - |
| 60.0 | 26.7±0.2 | 18.7±0.2 | 13.4±0.1 | - | - | - |
| 50.0 | 27.4±0.3 | 18.4±0.2 | 14.8±0.2 | - | - | - |
| 40.0 | 29.0±0.3 | 18.5±0.2 | 16.5±0.2 | - | - | - |
| 35.0 | 30.0±0.3 | 18.7±0.2 | 16.3±0.2 | - | - | - |
| 32.0 | 30.0±0.3 | 19.0±0.2 | 17.4±0.2 | - | - | - |
| 29.0 | 31.1±0.3 | 18.8±0.2 | 18.0±0.2 | - | - | - |
| | | | Phase II | | | |
| 27.0 | 34.2±0.3 | 17.3±0.2 | 19.7±0.2 | - | - | - |
| 25.0 | 36.8±0.3 | 18.8±0.2 | 19.5±0.2 | - | - | - |
| 23.0[1] | 38.8±0.4 | 19.9±0.3 | 17.6±0.3 | 39.6±0.4 | 12.3±0.4 | 9.5±0.4 |
| | | | Phase III | | | |
| 22.0 | 44.0±0.5 | 18.0±0.4 | 16.6±0.4 | 42.0±0.5 | 10.0±0.4 | 10.1±0.4 |
| 21.0 | 44.3±0.5 | 19.3±0.4 | 18.1±0.4 | 41.2±0.5 | 13.7±0.4 | 12.5±0.4 |
| 18.0 | 44.4±0.5 | 19.6±0.4 | 18.4±0.4 | 42.0±0.6 | 14.1±0.4 | 12.6±0.4 |

---

[1] The best fit elastic constants were first obtained for the cubic structure but the fit was not satisfactory and the values of elastic constants were not consistent with the values at the higher temperatures.

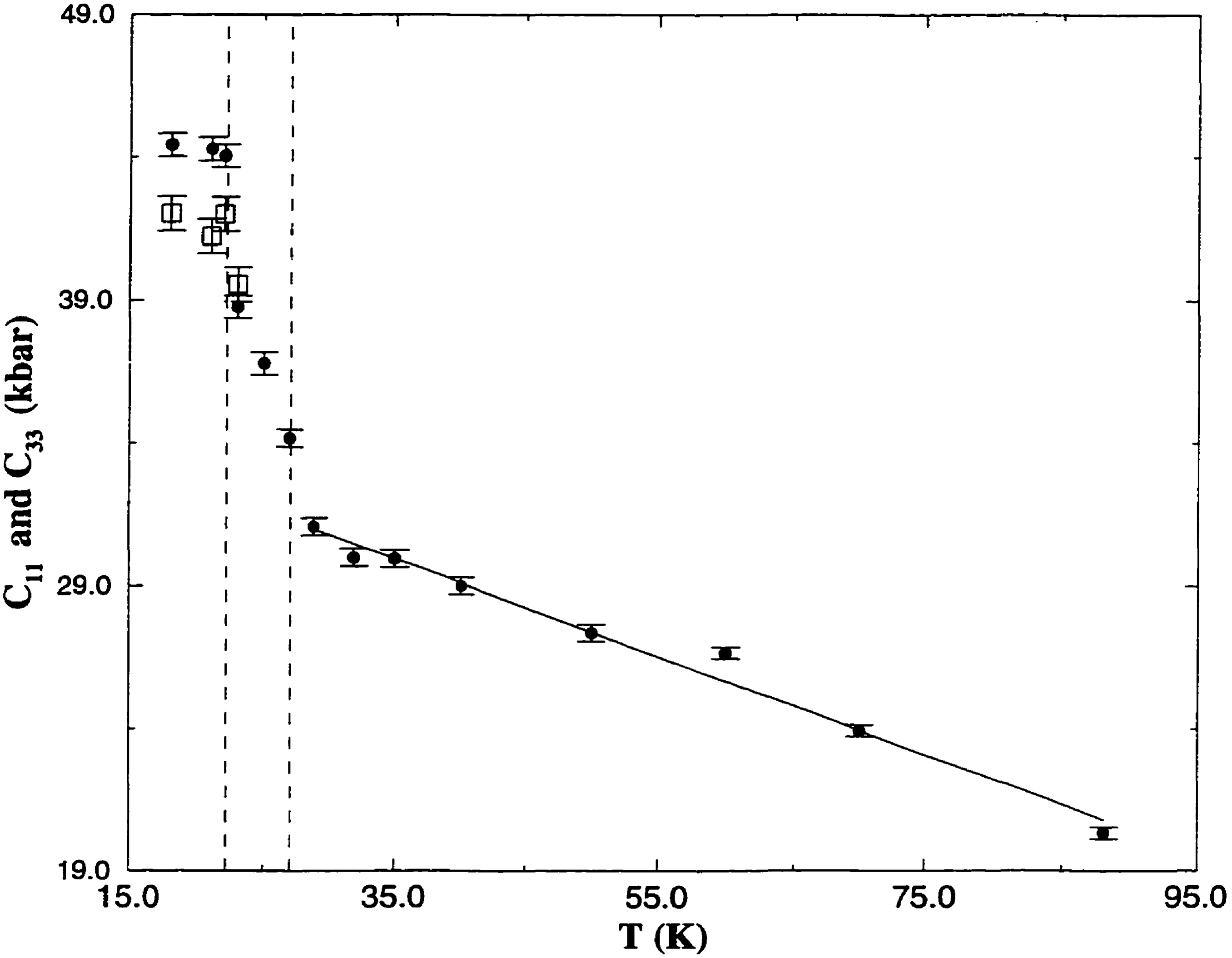

Figure 6.3: Elastic constants $C_{11}$ (●) and $C_{33}$ (□) of $CD_4$ as a function of temperature. The error bars shown represent the standard deviation in the best fit parameters and uncertainties in the frequency shift and crystal orientation. The dashed lines are positioned at phase transition temperatures of $T_{c1}$=27.1 K and $T_{c2}$=22.1 K

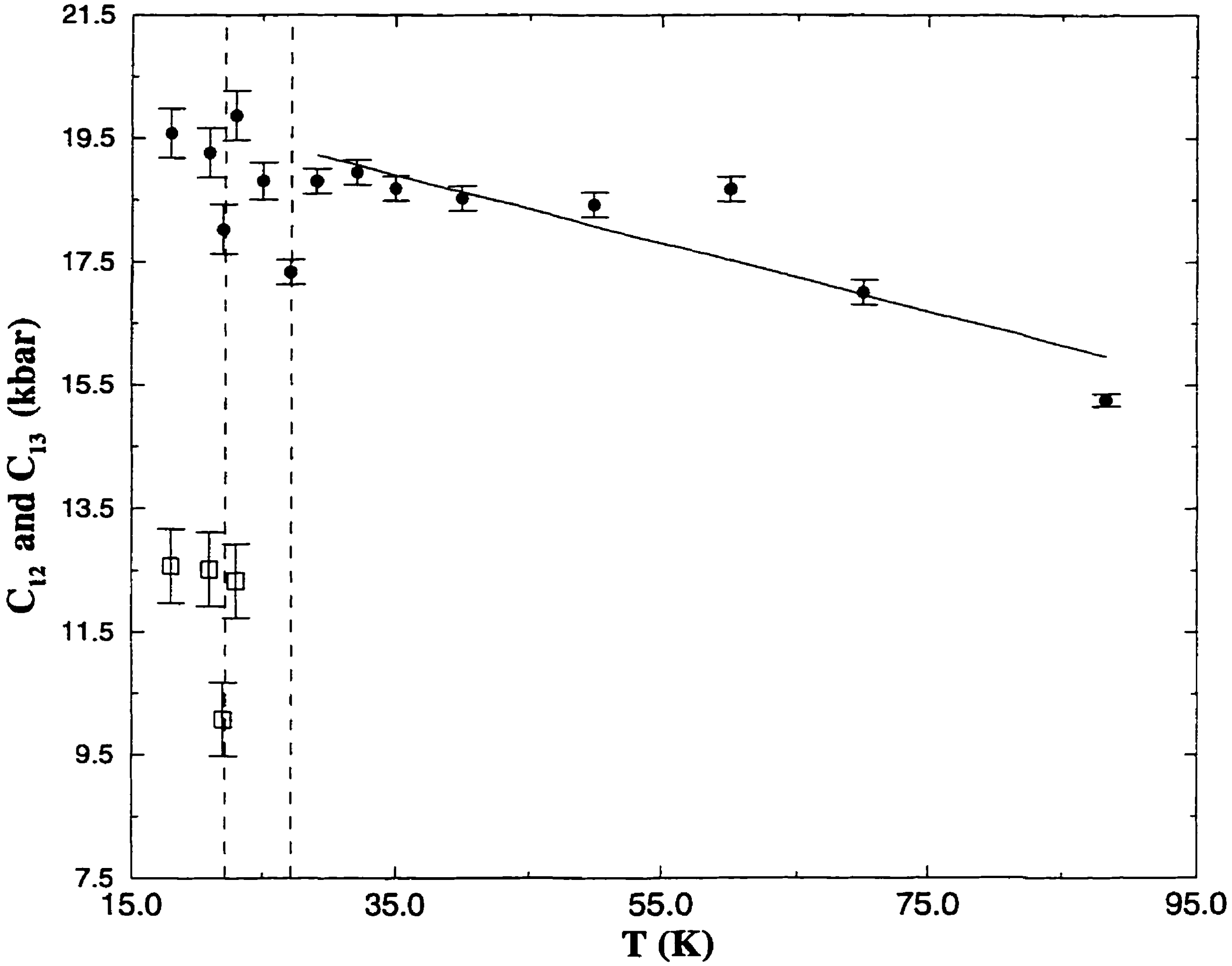

Figure 6.4: Elastic constants $C_{12}$ (●) and $C_{13}$ (□) of $CD_4$ as a function of temperature. The error bars shown are as in Fig. 6.3. The dashed lines are positioned as in Fig. 6.3.

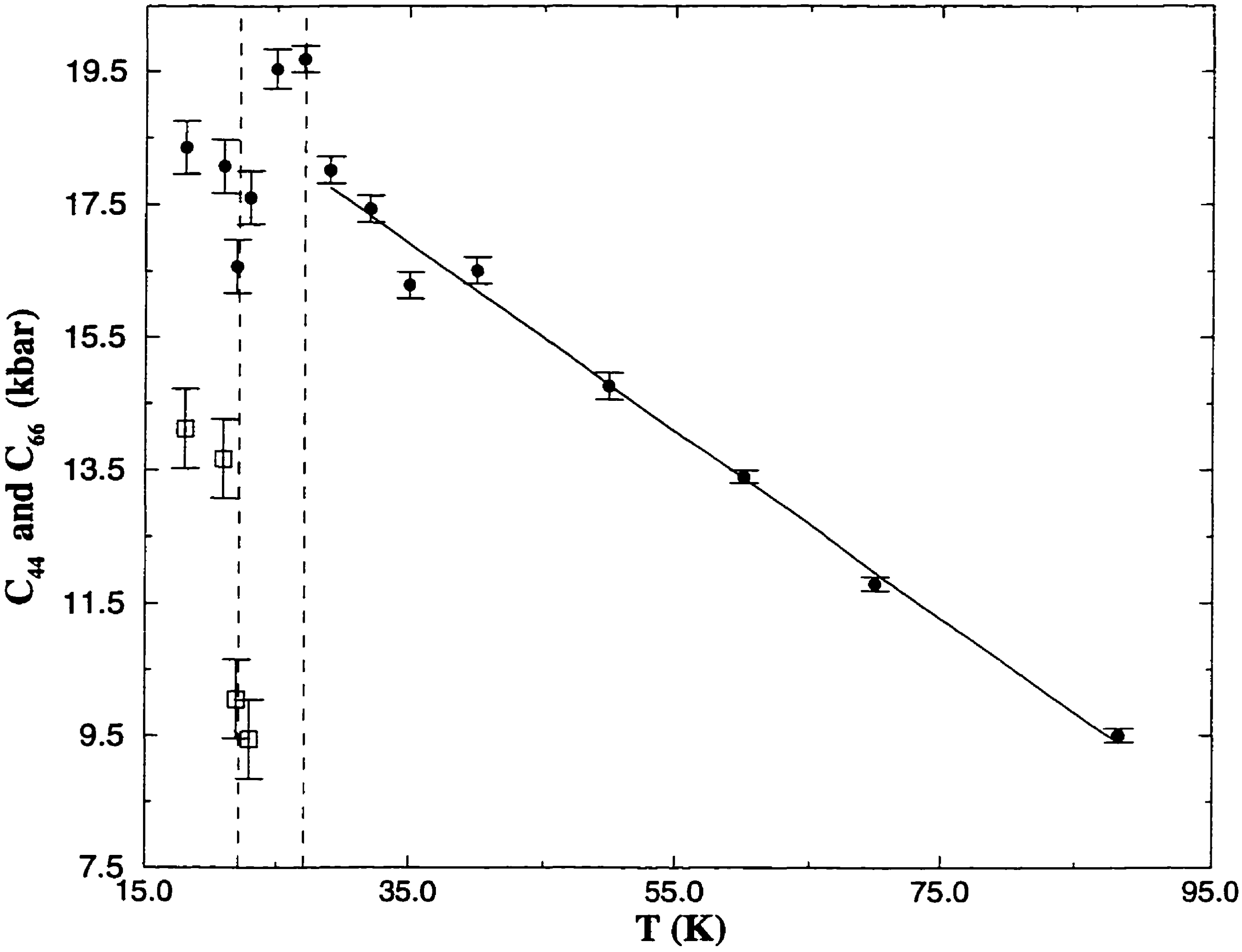

Figure 6.5: Elastic constants $C_{44}$ (●) and $C_{66}$ (□) of $CD_4$ as a function of temperature. The error bars shown are as in Fig. 6.3. The dashed lines are positioned as in Fig. 6.3.

The combinations of elastic constants corresponding to the < 110 > direction are shown in Fig. 6.6. The $\frac{1}{2}(C_{11}-C_{12})$ construction and $C_{44}$ correspond to two shear moduli in the cubic phase. The bulk modulus in the cubic phase was calculated using Eq. 5.7. The bulk modulus (B) in tetragonal phase and the aggregate shear modulus (G) in all phases were obtained from the individual elastic constants using the Voight-Reuss-Hill averaging method [138, 149] (shown in Fig. 6.7). The bulk modulus increases by a factor 1.5 and the shear modulus increases by a factor of 3 across the investigated temperature range.

The anisotropy factor (A) and the violation of the Cauchy relation ($\delta$) in phases I and II are plotted in Fig. 6.8. The values for both quantities are very similar to those of methane although $\delta$ starts to deviate from 0 as the temperature approaches $T_c$=22.1 K.

When all elastic constants are known it is possible to calculate the acoustic velocity and the Poisson ratio. The Poisson ratio is shown in Fig. 6.11(a). The acoustic velocities distribution in the high symmetry planes (100) and (110) for all three phases are shown in Fig. 6.9 and 6.10. The velocities in the phase III are shown in Fig. 6.10. The degree of anisotropy of $CD_4$ is nearly the same as in $CH_4$. It is interesting to notice that the distribution becomes more isotropic in the tetragonal phase.

### 6.2.2 Thermodynamic Properties

As in the case of $CH_4$, thermodynamic properties such as Debye temperature, lattice specific heat and Grüneisen parameter could be calculated. The Debye temperature of solid $CD_4$ is shown in Fig. 6.11(b) and compared with data from Ref. [17]. The values obtained in this experiment are higher, although the deviation becomes smaller as temperature decreases. In the present investigation the values of Debye temperature change more abruptly at the first phase transition and the change is bigger than in the case of methane. At the second phase transition the jump is much smaller but still visible.

By integrating the Debye temperature the lattice specific heat can be calculated (see

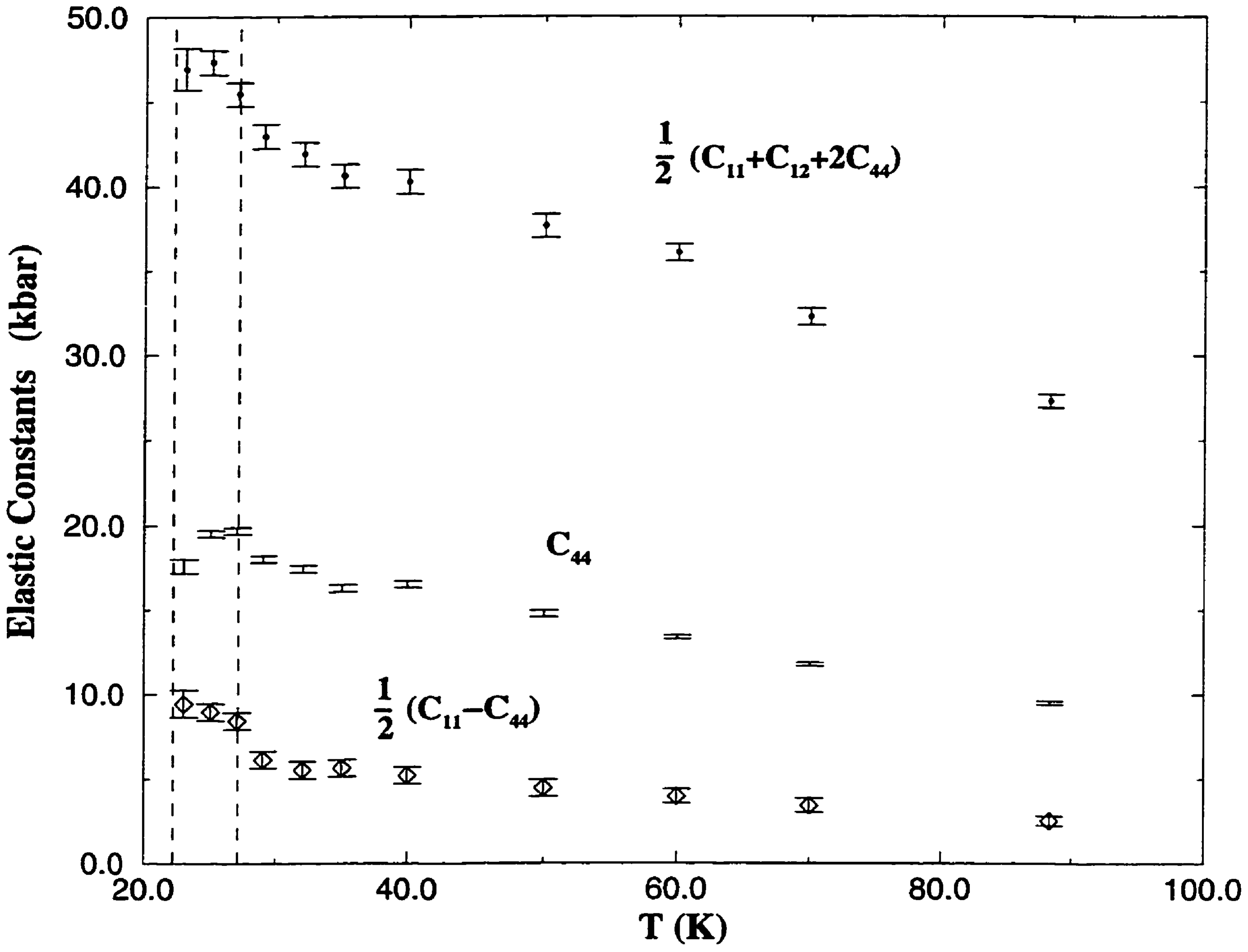

Figure 6.6: Elastic constants of $CD_4$ as a function of temperature in phases I and II. The combinations correspond to the longitudinal and two transverse modes. $\frac{1}{2}(C_{11}-C_{12})$ and $C_{44}$ also correspond to the shear moduli in cubic system. The error bars shown are from the errors in elastic constants as in Fig. 6.3, 6.4 and 6.5. The dashed lines are positioned as in Fig. 6.3.

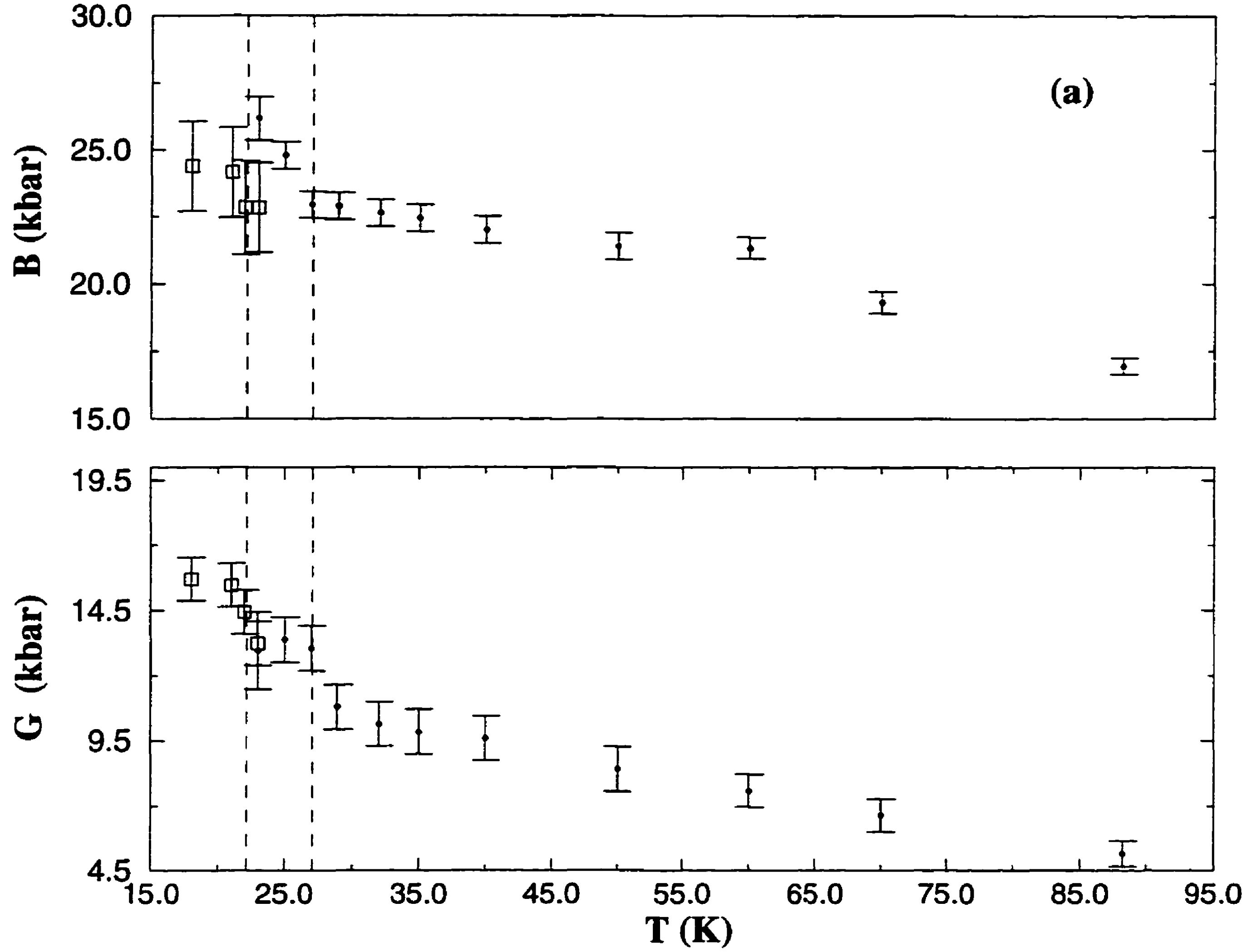

Figure 6.7: Elastic moduli of $CD_4$ as a function of temperature. The error bars shown are from the errors in elastic constants as in Fig. 6.6. The dashed lines are positioned as in Fig. 6.3.

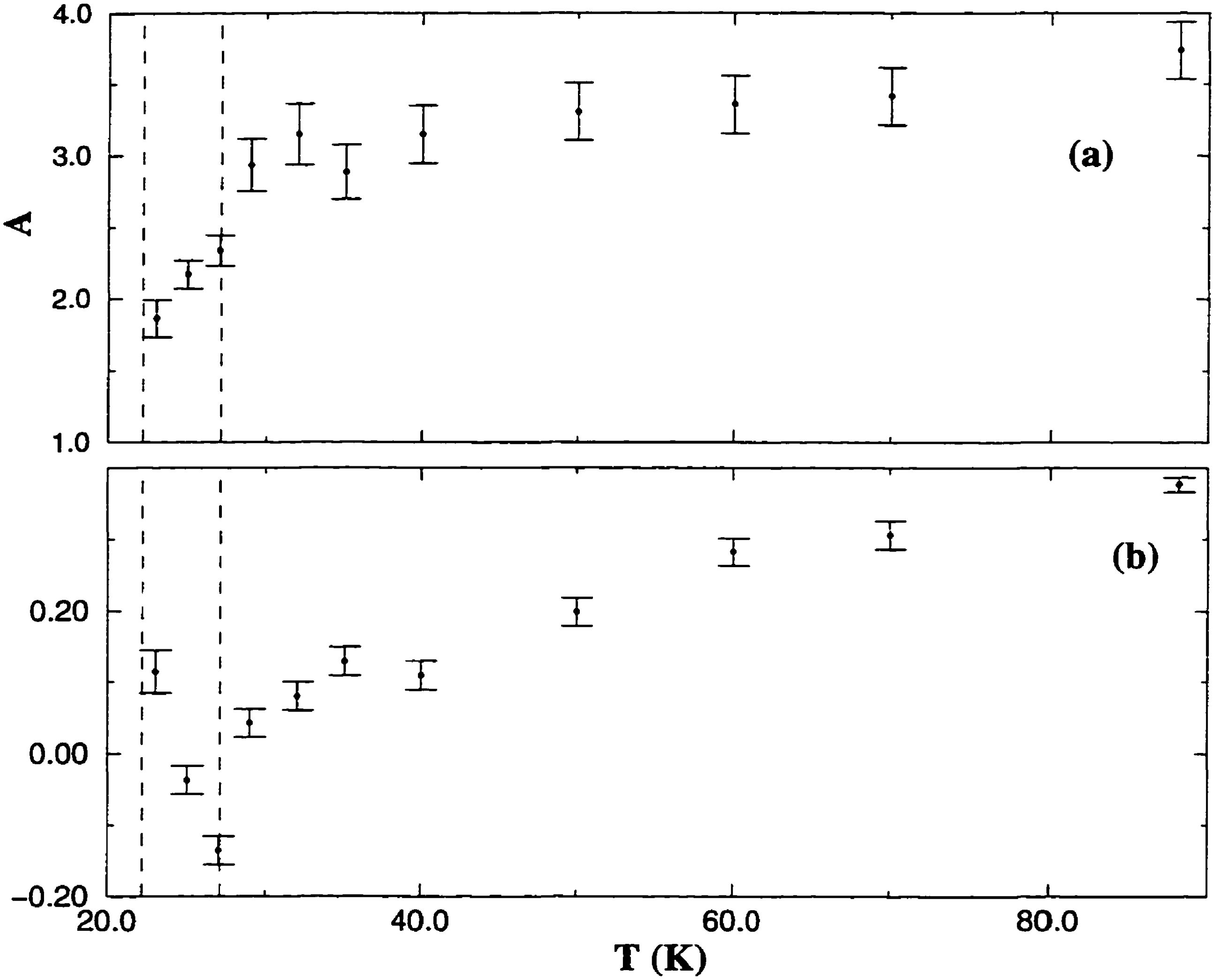

Figure 6.8: (a) Anisotropy factor and (b) violation of Cauchy relation of $CD_4$ as a function of temperature. The dashed lines are positioned as in Fig. 6.3.

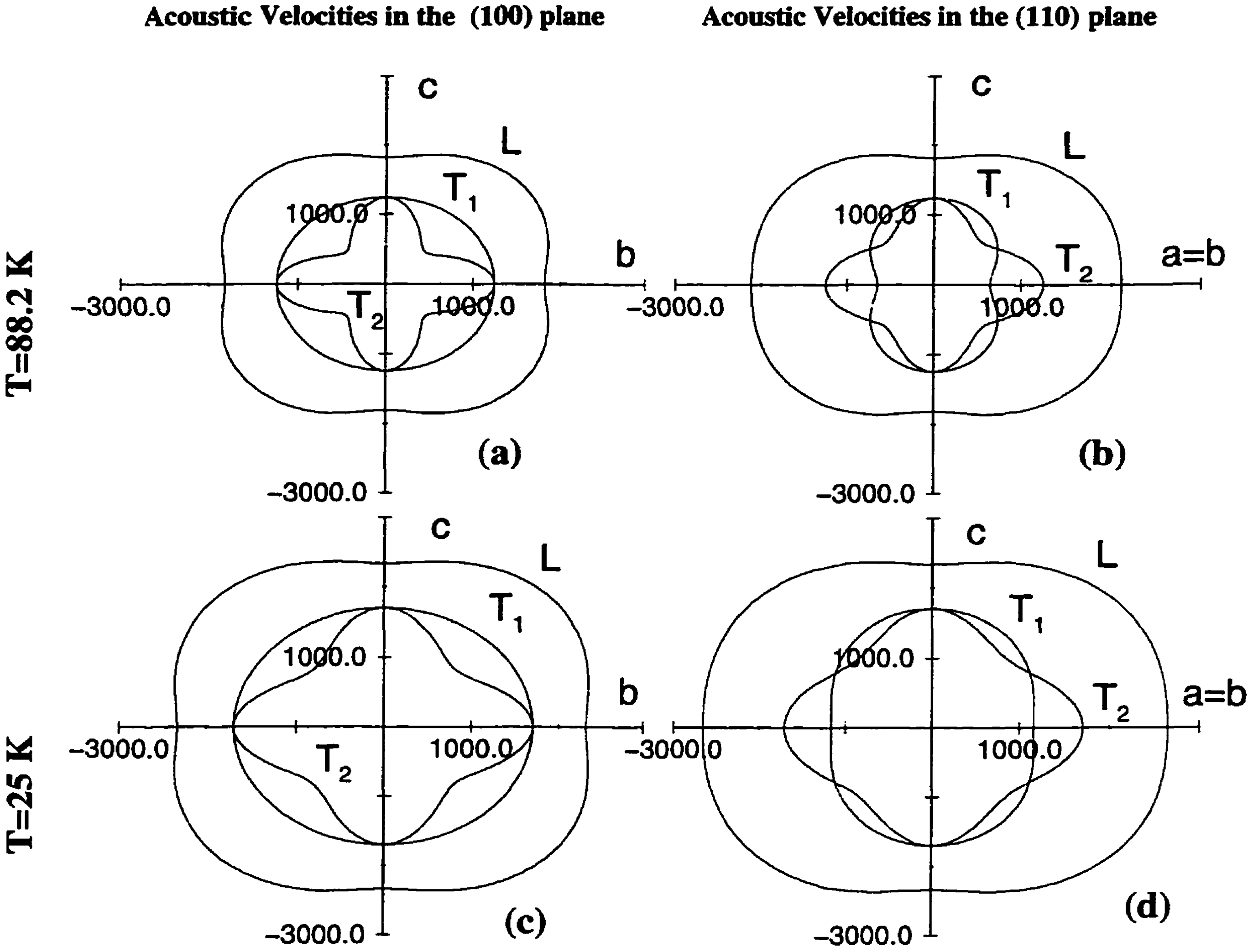

Figure 6.9: Acoustic velocities of $CD_4$ (in $ms^{-1}$) in high symmetry planes in phases I and II. (a) and (b) are at 88.2 K (phase II). (c) and (d) at 25 K (phase II). (a) and (c) are in the (100) plane, (b) and (d) are in the (110) plane.

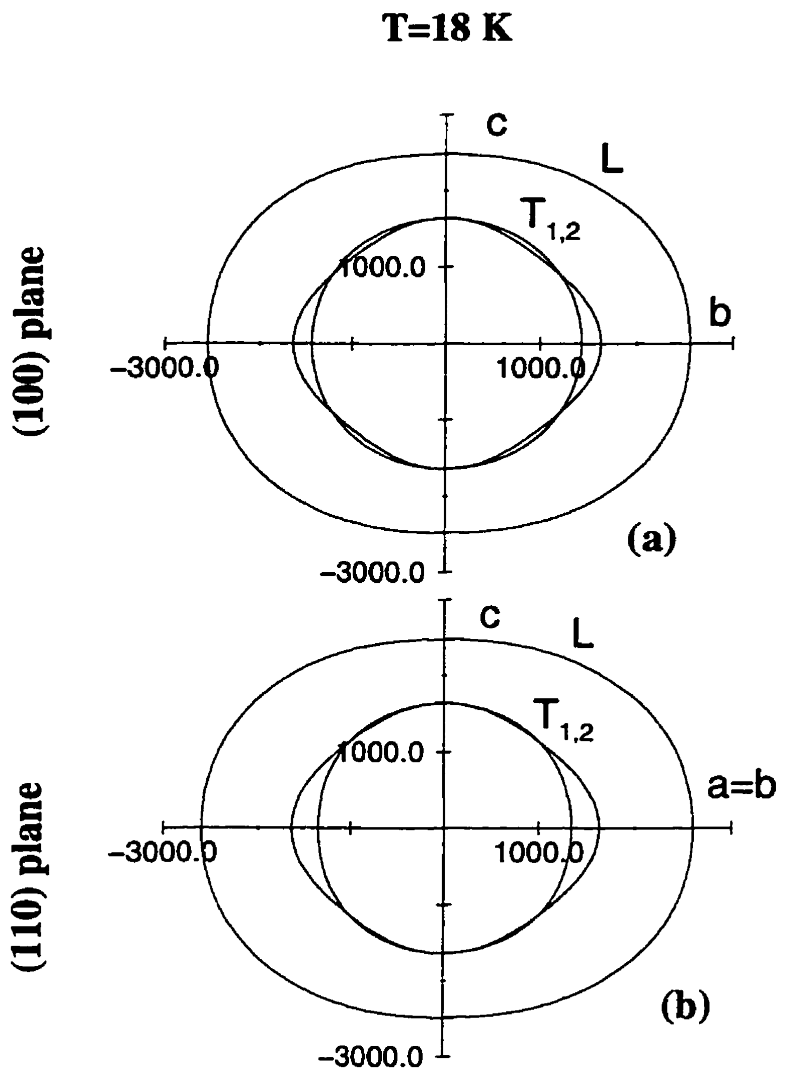

Figure 6.10: Acoustic velocities of CD$_4$ (in ms$^{-1}$ in phase III at 18 K. (a) is in the (100) plane and (b) is in the (110) plane.

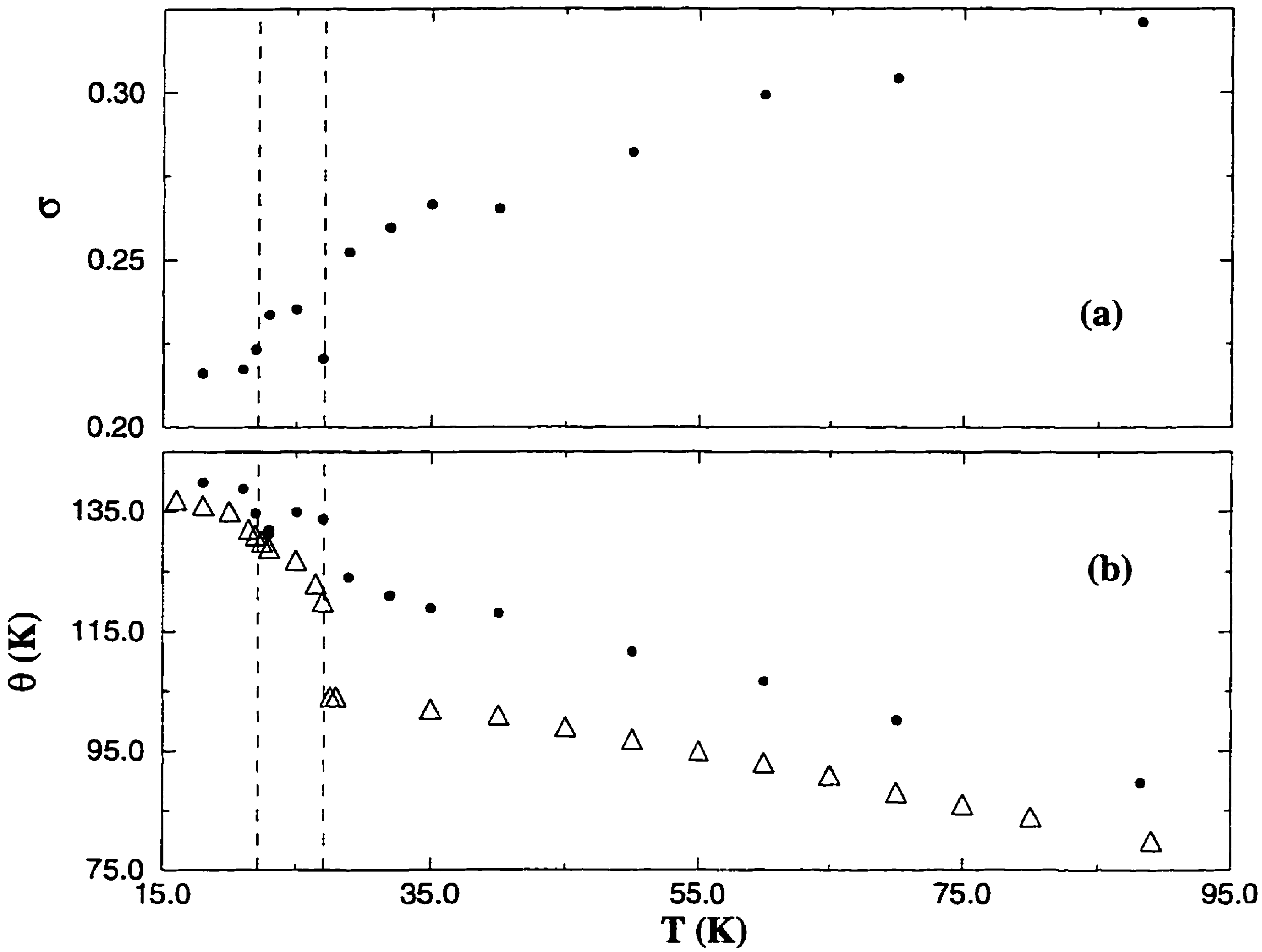

Figure 6.11: (a) Poisson ratio ($\sigma$) of $CD_4$ as a function of temperature. (b) Debye temperature of solid $CD_4$ (●). Compared with results (△) from Ref. [17]. The dashed lines are positioned as in Fig. 6.3

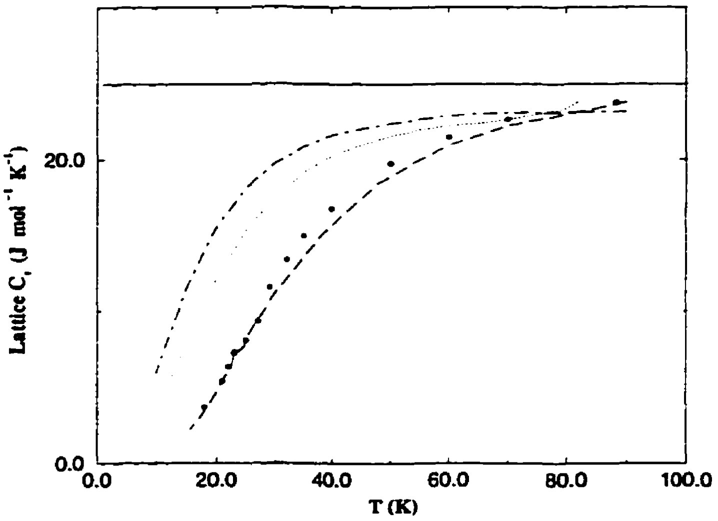

Figure 6.12: The lattice specific heat of $CD_4$ (●). Compared with $C_v$ of argon (· · ·), krypton (- -·- - ·) from Ref. [143, 144, 145] and $CH_4$ ( - - - -). The solid line is positioned at 3R.

Fig. 6.12. By combining the lattice specific heat with the known specific heat at constant pressure [14] and coefficient of volume expansion [17] the rotational specific heat can be separated and calculated. Again, as in the case of $CH_4$, this procedure is done with the assumption that the rotational motion is not affected by translation. The temperature dependence of the rotational specific heat is shown in Fig. 6.13. The most interesting result is that in the wide temperature range from the onset of the first phase transition to ~55 K the rotational specific heat is larger than $\frac{3}{2}$R. At temperatures higher than 55 K the rotational heat becomes lower than this free rotational value. This could be associated with a temperature dependent RT coupling mechanism.

The Grüneisen parameter of $CD_4$ in the high temperature phase is almost independent of temperature and higher than in methane. Its average value is approximately equal to 2.1. For all rare gas solids, at zero pressure, the Grüneisen parameters agree within ± 0.15 with the value 2.7 [72].

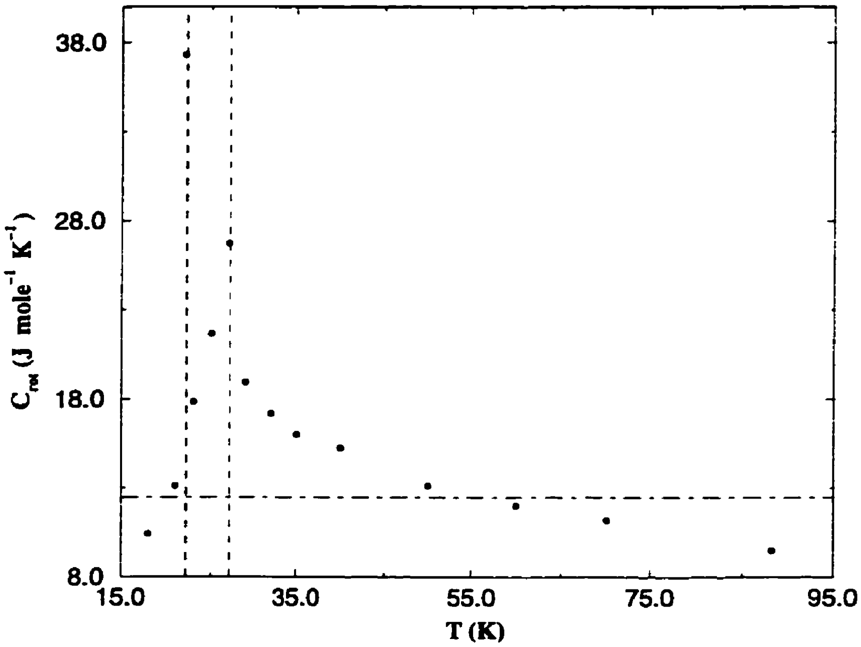

Figure 6.13: Rotational specific heat of $CD_4$ as a function of temperature. (- · · · · ·) line is positioned at $\frac{3}{2}$R. The dashed lines are positioned as in Fig. 6.3

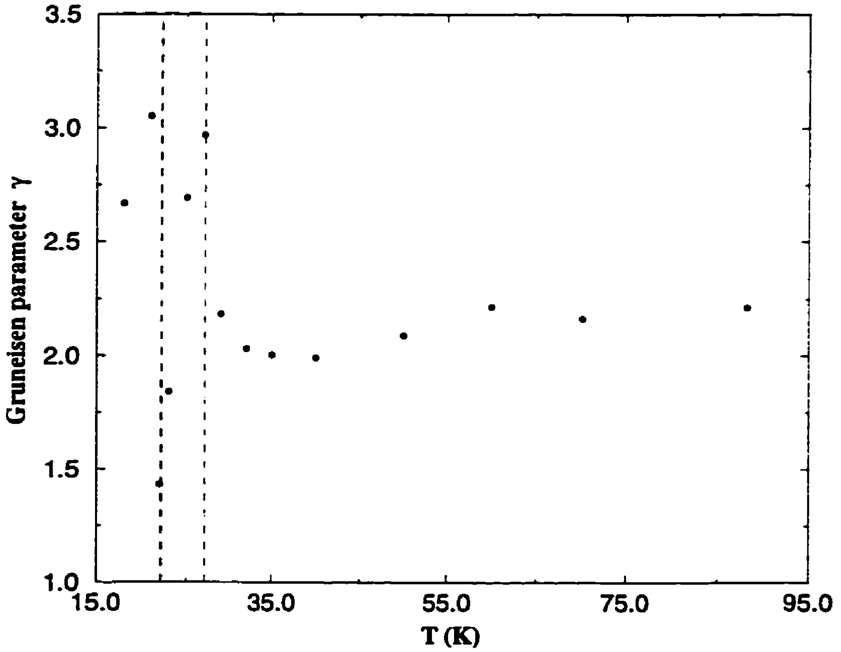

Figure 6.14: The Grüneisen parameter of $CD_4$. The dashed lines are positioned as in Fig. 6.3

# Chapter 7

# Discussion

Studies of acoustic properties of van der Waals solids, particularly around their phase transitions, have not been performed because of the difficulties in growing and cooling such solids within the required optical setups. The present work makes the first systematic attempt to cool single crystals of methanes over a sufficiently wide temperature range to include all phases, and to determine their elastic properties as a function of temperature.

The Brillouin data obtained in the phase III of $CD_4$ show that this phase belongs to one of the classes with 6 elastic constants: $4mm$, 422, $\bar{4}, 2m$ or $4/mmm$. To the author's knowledge this is the first attempt to determine the possible space group of $CD_4$-III by means of Brillouin spectroscopy.

The elastic data permit a determination of the distribution of acoustic velocities with respect to crystal directions and how this distribution changes with temperature. As mentioned in Chapter I, the rotational-translational coupling plays an important role in the dynamics of the solid methanes. The results of Brillouin spectroscopy in $CH_4/CD_4$ near their triple points indicate a strong coupling manifesting itself in very slow acoustic transverse phonons in the $< 110 >$ direction [18]. Table 7.1 includes the temperature dependences of the ratios of acoustic velocities $V_L/V_T$ for high symmetry directions for both methanes studied in the present work and in some other cubic lattices such as the rare gas solids. It can be seen that at the triple point temperatures the ratio $V_l/V_{t2}$ for the methanes is large compared with the same ratio in the RGS and as the temperature is decreased this ratio decreases to become equal to the ratio for the RGS at temperatures around 30 K. RT coupling therefore appears to decrease as the temperature is lowered. This is expected as the rotational motion decreases on approaching the order-disorder phase transition. It seems that the RT coupling is stronger in heavy methane and causes larger changes in the values of elastic constants and Debye temperature when the crystal goes through the I-II phase transition.

Table 7.1: Ratios of sound velocities in high symmetry directions of the rare gas solids compared with $CH_4$ and $CD_4$ at different temperatures

| Crystal | T (K) | $< 100 >$ | $< 111 >$ | $< 110 >$ | $< 110 >$ |
|---|---|---|---|---|---|
| | | $V_l/V_t$ | $V_l/V_t$ | $V_l/V_{t1}$ | $V_l/V_{t2}$ |
| RGS | | 1.44 | 2.24 | 1.65 | 2.71 |
| $CH_4$ | 90.0 | 1.46 | 2.48 | 1.69 | 3.31 |
| | 70.0 | 1.44 | 2.37 | 1.66 | 3.03 |
| | 60.0 | 1.42 | 2.34 | 1.65 | 2.98 |
| | 54.0 | 1.42 | 2.31 | 1.64 | 2.90 |
| | 30.0 | 1.37 | 2.21 | 1.59 | 2.71 |
| | 20.5 | 1.29 | 2.19 | 1.54 | 2.76 |
| | 15.5 | 1.34 | 2.12 | 1.56 | 2.54 |
| $CD_4$ | 89.2 | 1.47 | 2.45 | 1.70 | 3.22 |
| | 70.0 | 1.42 | 2.47 | 1.65 | 3.05 |
| | 60.0 | 1.41 | 2.34 | 1.64 | 3.00 |
| | 50.0 | 1.36 | 2.28 | 1.60 | 2.89 |
| | 32.0 | 1.31 | 2.20 | 1.55 | 2.76 |
| | 29.0 | 1.31 | 2.15 | 1.55 | 2.54 |
| | 25.0 | 1.37 | 2.01 | 1.56 | 2.29 |

A similar tendency is observed in the anisotropy factor and the violation of the Cauchy relation. These parameters are large at the triple point temperatures in both methanes but as soon as temperature is decreased they decrease in value in the phase II show some similarities between the methanes and the RGS.

Some inconsistency in the values of elastic constants presented in the present work e.g.

$C_{12}$ of $CH_4$ at 38.0 K and $C_{12}$ of $CD_4$ at 60 K could be attributed to the spin conversion effects. It must be noted that methane exhibits three spin species corresponding to the nuclear spin I=2,1,0 labeled as A,T,E species [150]. NMR studies of the spin lattice relaxation time in the plastic phase of methane have shown that the relaxation time can be different depending on the cooling history of the sample [151]. If the sample was cooled quickly from ~ 80 to 50 K, the spin lattice relaxation time is about two orders of magnitude smaller than if cooling is slow. This indicates that fast cooling to 50 K may produce a sample with higher structural disorder than in a case of slow cooling. The inconsistency in elastic constants may be related to the rate at which different samples were cooled and hence to the rate of spin conversion.

Difficulties associated with cooling of van der Waals solids include shattering on cooling, change of orientation on cooling and precise control of the cooling procedure. These difficulties could be reduced with the modification of the present apparatus.

1) A more precise pressure gauge, preferably situated closer to the cell, in order to control the sample pressure while cooling will increase the probability of obtaining high-quality crystals.

2) In the present experiment, the rotation of the cell about the $z$-axis is limited to $70^0$ because of the electrical wiring. As noted before, the intensities of transverse peaks are greatly reduced at the low temperatures and some crystal orientations do not have any transverse peaks at all. If the rotation could be extended to at least $180^0$ it would give much bigger choice of angle $\phi$, which can considerably reduce the time needed to collect the data, as well as reduce the errors associated with fitting routines.

3) But the most important modification could be the one which would allow the injection into the cell of gas for which the normal boiling point is at lower temperature than the triple point of the system under investigation. This would allow for creation of the liquid

layer acting as a cushion around the methane (or any van der Waals) crystal. A similar technique was successfully employed in high-pressure research [152] when the single crystal of hydrogen was grown in helium, which prevents the risk of fragmentation of the hydrogen crystal on increasing pressure.

The Raman measurements done in the present work supplement the Brillouin data. The wave numbers of two of the internal modes and their linewidth were measured by the Raman scattering which provides definitive evidence that the phase transitions took place. The analysis of the behavior of Raman lines in $CH_4$ shows that rotational motion is "freezing out", which is consistent with the measurements of acoustic velocities in the $< 110 >$ direction, but nevertheless it still exists and causes the $\nu_1$ mode to broaden in phase II.

Although the behavior of the Raman shifts in $CD_4$ is similar to $CH_4$, the existence of phase III makes it more complicated. Even the higher temperature phases show some differences between the two solids. The Raman shifts in $CH_4$ as well as the width of the $\nu_1$ line are virtually independent of temperature. The width of $\nu_3$ changes from $\sim$100 $cm^{-1}$ at the triple point to $\sim$40 $cm^{-1}$ at the phase transition and then, as temperature is decreased below the phase transition value the width goes through an enormous change and jumps down to $\sim$2 $cm^{-1}$. The shifts in $CD_4$ apparently are more temperature dependent. Both lines downshift at around 55 K and the width of these lines changes quite dramatically around the same temperature. The width changes much more over the high temperature phase from $\sim$ 75 $cm^{-1}$ at the triple point to 9 $cm^{-1}$ at 28 K and at 27 K it jumps to $\sim$2 $cm^{-1}$. Clearly, the change is not as big as in the case of $CH_4$. The measurements of rotational specific heat of $CD_4$ show (see Fig. 6.13) that $C_{rot}$ becomes greater than the specific heat of a freely rotating molecule at temperatures lower then 55 K when the crystal is still far from the first phase transition. In conjunction with the Raman results it suggests that the RT mechanism in $CD_4$ is more complicated than previously thought and not linearly dependent on temperature.

In conclusion, the present work may be complemented by conducting additional Raman and Brillouin spectroscopic studies on other isotopes of methane with $CH_2D_2$ being a primary candidate and comparing them with the existing results. Another interesting possibility would be the investigation of the methane family by changing pressure: the pressure induced phase transition (phase IV) in methane is easily reached and this phase is most probably orientationally disordered. This kind of experiment will show the dependency of rotation-translation coupling on pressure which would undoubtedly expand our understanding of these molecular crystals.

# Bibliography

[1] Lord Rayleigh and W. Ramsay, Proc. R. Soc. **57**, 265 (1895).

[2] D. Young, *Phase Diagrams of the Elements* (University of California Press, Berkeley, 1991).

[3] E. Wigner and B. Huntington, J. Chem. Phys. **3**, 764 (1935).

[4] S. Weir, A. Mitchell, and W. Nellis, Phys. Rev. Lett. **76**, 1860 (1996).

[5] F. Simon and C. von Simson, Z. Physik **21**, 168 (1924).

[6] J. Timmermans, J. Chim. phys. **35**, 331 (1938).

[7] J. Timmermans, J. Phys. and Chem. Solids **18**, 1 (1961).

[8] F. Zernike, Ned. Tijdschr. Natuurkunde **8**, 66 (1941).

[9] M. Buie *et al.*, Bull. Am. Astron. Soc. **21**, 985 (1989).

[10] D. Cruikshank *et al.*, Icarus **74**, 413 (1988).

[11] G. Lindal *et al.*, J. Geophys. Res. **92**, 14987 (1987).

[12] B. Smith *et al.*, Science **246**, 1422 (1989).

[13] *CRC Handbook of Chemistry and Physics* (CRC Press, Boca Raton, Florida, 1996).

[14] J. Colwell, E. Gill, and J. Morrison, J. Chem. Phys. **39**, 635 (1963).

[15] R. Prydz and R. Goodwin, J. Chem. Thermodynamics **76**, 127 (1972).

[16] A. Prokhvatilov and A. Isakina, Sov. J. Low Temp. Phys. **9**, 231 (1983).

[17] A. Prokhvatilov and A. Isakina, Phys. Stat. Sol. (a) **78**, 147 (1983).

[18] S. Rand and B. Stoicheff, Can. J. Phys. **60**, 287 (1982).

[19] D. Aadsen, Ph.D. thesis, University of Illinois at Urbana-Champaign, 1975.

[20] D. Baer, B. Fraass, D. Riehl, and R. Simmons, J. Chem. Phys. **68**, 1411 (1978).

[21] K. Clusius, Z. Physik. Chem. **B(3)**, (1929).

[22] M. Crawford, H. Welsh, and J. Harrold, Can. J. Phys. **30**, 81 (1952).

[23] A. Cabana, G. Savitsky, and D. Hornig, J. Chem. Phys. **39**, 2942 (1963).

[24] A. Anderson and R. Savoie, J. Chem. Phys. **43**, 3468 (1965).

[25] A. Rest, R. Warren, and S. Murray, Spectrochimica Acta Part A **52**, 1455 (1966).

[26] A. Cabana and N. Thé, Can. J. Phys. **55**, 3862 (1977).

[27] F. Medina, J. Chem. Phys. **73**, 77 (1980).

[28] D. Fabre, M. Thiery, H. Vu, and K. Kobashi, J. Chem. Phys. **71**, 3081 (1979).

[29] D. Fabre and M. Thiery, J. Chem. Phys. **76**, 4817 (1982).

[30] M. Thiery and D. Fabre, J. Chem. Phys. **83**, 6165 (1985).

[31] P. Hebert *et al.*, Phys. Rev. B **36**, 9196 (1987).

[32] P. Calvani, S. Cunsolo, S. Lupi, and A. Nucara, J. Chem. Phys. **96**, 7372 (1992).

[33] R. Bini, L. Ulivi, H. Jodl, and P. Salvi, J. Chem. Phys. **103**, 1353 (1995).

[34] Y. Wu, S. Sasaki, and H. Shimizu, J. of Raman Spectroscopy **26**, 963 (1995).

[35] S. Sasaki, N. Nakashima, and H. Shimuzu, Physica B **219** & **220**, 380 (1996).

[36] S. Marx and R. Simmons, J. Chem. Phys. **81**, 944 (1984).

[37] W. Press, B. Dorner, and H. Stiller, Solid State Communications **9**, 1113 (1971).

[38] W. Press and A. Huller, in *Anharmonic Lattices,structural transitions and melting*, edited by T. Rieste (Noordhoff Int. Publishing, Noordhoff - Leiden, 1974), p. 185.

[39] W. Press and A. Kollmar, Solid State Communications **17**, 405 (1975).

[40] W. Stirling, W. Press, and H. Stiller, J. of Physics C **10**, 3959 (1977).

[41] M. Prager and *et al.*, J. Chem. Phys. **75**, 1442 (1981).

[42] M. Prager and *et al.*, J. Chem. Phys. **77**, 257 (1982).

[43] I. Krupskii, A. Prokhvatilov, and A. Isakina, Sov. J. Low Temp. Phys. **8**, 317 (1982).

[44] I. Krupskii, A. Prokhvatilov, and A. Isakina, Solid St. Comm. **42**, 59 (1982).

[45] A. Prokhvatilov and A. Isakina, Sov. J. Low Temp. Phys. **10**, 631 (1984).

[46] A. Prokhvatilov and A. Isakina, Sov. J. Low Temp. Phys. **10**, 91 (1984).

[47] H. James and T. Keenan, J. Chem. Phys. **31**, 12 (1959).

[48] T. Yamamoto, J. Chem. Phys. **48**, 3193 (1968).

[49] T. Yamamoto and Y. Kataoka, J. Chem. Phys. **48**, 3199 (1968).

[50] Y. Kataoka and T. Yamamoto, Prog. Theor. Phys. Suppl. Extra Number 436 (1968).

[51] H. Yasuda, T. Yamamoto, and Y. Kataoka, Prog. Theor. Phys. **41**, 859 (1969).

[52] K. Nishiyama, Y. Kataoka, and T. Yamamoto, Prog. Theor. Phys. **43**, 1121 (1970).

[53] Y. Kataoka, Prog. Theor. Phys. **43**, 1132 (1970).

[54] H. Yasuda, Prog. Theor. Phys. **45**, 1361 (1971).

[55] A. Huller, Phys. Rev. B **10**, 4403 (1974).

[56] K. Michel and D. Kroll, J. Chem. Phys. **64**, 1300 (1976).

[57] T. Yamamoto, Y. Kataoka, and K. Okada, J. Chem. Phys. **66**, 2701 (1977).

[58] S. Wonneberger and A. Huller, Zeitshrift fur Physik B 191 (1987).

[59] D. Bounds, M. Klein, and G. Patey, J. Chem. Phys. **72**, 5348 (1980).

[60] W. Gornall and B. Stoicheff, Phys. Rev. B **4**, 4518 (1971).

[61] S. Gewurtz and B. Stoicheff, Phys. Rev. B **10**, 3487 (1974).

[62] D. Landheer *et al.*, Phys. Rev. B **13**, 888 (1976).

[63] Y. Fujii *et al.*, J. Phys. Chem. Sol. **36**, 145 (1975).

[64] R. Fisher and R. Watts, Mol. Phys. **23**, 1051 (1972).

[65] J. Skalyo and Y. Endoh, Phys. Rev. B **7**, 4670 (1973).

[66] J. Barker, M. Klein, and M. Bobetic, Phys. Rev. B **2**, 4176 (1970).

[67] A. Huller, Z. Phys. **245**, 324 (1971).

[68] H. Peter *et al.*, J. Phys. Chem. Sol. **34**, 255 (1973).

[69] M. Klein and R. Murphy, Phys. Rev. B **6**, 2433 (1972).

[70] N. Lurie *et al.*, Phys. Rev. B **9**, 2661 (1974).

[71] J. Skalyo, Y. Endoh, and G. Shirane, Phys. Rev. B **9**, 1797 (1974).

[72] M. Klein and J. Venables, *Rare Gas Solids I and II* (Academic Press, London, 1977).

[73] R. McLaren, H. Kiefte, D. Landheer, and B. Stoicheff, Phys. Rev. B **11**, 1705 (1975).

[74] J. Zuk, H. Kiefte, and M. Clouter, J. Chem. Phys. **92**, 917 (1990).

[75] J. Zuk, D. Brake, H. Kiefte, and M. Clouter, J. Chem. Phys. **91**, 5285 (1989).

[76] R. Lynden-Bell and K. Michel, Rev. Mod. Phys. **66**, 721 (1994).

[77] P. Ehrenfest, Proc. Amsterdam Acad. **36**, 153 (1933).

[78] L. Landau and E. Lifshitz, *Statistical Physics* (Pergamon Press, Oxford, London, 1969).

[79] A. Goncharov *et al.*, in *Proc. of XV Inter. Conf. on Raman Spectroscopy*, edited by S. Asher and B. Stein (John Willey and Sons, Chichester and New York, 1996), p. 1042.

[80] K. Maki and *et al.*, J. Chem. Phys. **66**, 655 (1979).

[81] W. Press, J. Chem. Phys. **56**, 2597 (1972).

[82] D. Bol'shutkin *et al.*, J. Structural Chem. **12**, 313 (1971).

[83] W. Press, B. Dorner, and G. Will, Phys. Letters **31A**, 253 (1970).

[84] E. Arzi and E. Sandor, Acta Crys. **A28**, S188 (1972).

[85] E. Balic *et al.*, J. Chem. Phys. **57**, 1793 (1972).

[86] E. Balic *et al.*, J. Chem. Phys. **58**, 5639 (1973).

[87] L. Landau and E. Lifshitz, *Theory of Elasticity* (Pergamon Press, Oxford, London, 1969).

[88] J. Nye, *Physical Properties of Crystals* (Clarendon Press, Oxford, 1972).

[89] T. Narasimhamurtu, *Photoelastic and Electro-Optic Properties of Crystals* (Plenum Press, New York and London, 1981).

[90] H. Huntington, *The Elastic Constants of Crystals* (Academic Press, New York and London, 1958).

[91] M. Musgrave, *Crystal Acoustics* (Holden-Day, San Francisco, 1970).

[92] Lord Rayleigh, Philos. Mag **47**, 375 (1899).

[93] Lord Rayleigh, *The Theory of Sound* (Dover Publications, New York, 1945).

[94] L. Brillouin, Ann. Phys. **17**, 88 (1922).

[95] L. Mandelstam, Zh. Russ. Fiz. Khim. Ova. **58**, 381 (1926).

[96] E. Gross, Nature **126**, 201,400 (1930).

[97] R. D. Mountain, Rev. Mod. Phys. **38**, 205 (1966).

[98] G. B. Benedek, in *Brandeis University Summer Institute of 1966 in Theoretical Physics*, edited by M. Chretein, E. Gross, and S. Deser (Brandeis University Press, Waltham,Mass, 1968), p. 1.

[99] D. McIntyre and J. V. Sengers, in *Physics of Simple Fluids*, edited by H. N. V. Temperley, J. S. Rowlinson, and G. S. Rushbrooke (North Holland, Amsterdam, 1968), p. 447.

[100] I. L. Fabelinskii, *Molecular Scattering of Light* (Plenum Press, New York, 1968).

[101] P. A. Fleury and J. P. Boon, Adv. Chem. Phys. **24**, 1 (1973).

[102] B. J. Berne and R. Pecora, *Dynamic Light Scattering* (John Wiley, New York, 1976).

[103] G. Benedek and K. Fritsch, Phys. Rev. **149**, 647 (1966).

[104] K. Nelson *et al.*, J. App. Phys **53**, 1144 (1982).

[105] K. Nelson *et al.*, J. Chem. Phys. **77**, 1144 (1982).

[106] M. D. Fayer, Ann. Rew. Phys. Chem **33**, 63 (1982).

[107] J. Brown *et al.*, J. Geoph. Res. **94**, 9485 (1989).

[108] Y. X. Yan, L. T. Cheng, and K. A. Nelson, in *Advances in non-linear spectroscopy*, edited by R. J. H. Clark and R. E. Hester (Wiley, New York, 1988), p. 299.

[109] A. G. Every, Phys. Rev. B **22**, 1746 (1980).

[110] C. Kittel, *Introduction to Solid State Physics* (John Wiley and Sons, New York, 1996).

[111] J. Tyndal, Proc. Roy. Soc. **17**, 1525 (1886).

[112] A. Smekal, Naturwiss. **11**, 873 (1923).

[113] C. V. Raman and K. S. Krishnan, Nature **121**, 501,711 (1928).

[114] G. Landsberg, *Izbrannye Trydy (Selected Works)* (Izdatel'stvo AN SSSR, Moscow, 1958).

[115] L. Mandelstam, *Izbrannye Trydy (Selected Works)* (Izdatel'stvo AN SSSR, Moscow, 1947).

[116] *The Raman Effect*, edited by A. Anderson (Marcel Dekker, Inc., New York, 1971).

[117] G. Herzberg, *Molecular Spectra and Molecular Structure* (D. Van Nostrand Company, New York, 1960).

[118] S. Freeman, *Applications of Laser Raman Spectroscopy* (John Wiley & Sons, New York, 1974).

[119] W. Hayes and R. Loudon, *Scattering of Light by Crystals* (John Wiley & Sons, New York, 1978).

[120] P. Sherwood, *Vibrational Spectroscopy of Solids* (Cambridge University Press, London, 1972).

[121] *Vibrational Spectroscopy of Phase Transitions*, edited by Z. Iqbal and F. Owens (Academic Press, Inc, Orlando, 1984).

[122] H. Ibach and H. Luth, *Solid-State Physics* (Springer-Verlag, Berlin, 1990).

[123] B. Shrader, Angew. Chem. Int. Ed. Engl. **12**, 884 (1973).

[124] V. Askarpour, H. Kiefte, and M. J. Clouter, Can. J. Chem. **66**, 541 (1988).

[125] H. Kiefte and M. Clouter, J. Chem. Phys. **62**, 4780 (1975).

[126] J. M. Vaughan, *The Fabry-Perot Interferometer* (Adam Hilger, Bristol, 1989).

[127] S. Ahmad, Ph.D. thesis, Memorial University of Newfoundland, 1980.

[128] S. Ahmad, H. Kiefte, M. J. Clouter, and M. D. Whitmore, Phys. Rev. B **26**, 4239 (1982).

[129] J. C. Brice, *The Growth of Crystals from the Melt* (North-Holland, Amsterdam, 1965).

[130] E. Hecht, *Optics* (Adison-Wesley, Reading, 1979).

[131] M. Clouter, H. Kiefte, and C. Deacon, Phys. Rev. A **33**, 2749 (1986).

[132] M. Clouter, Ann. Rev. Phys. Chem. **39**, 69 (1988).

[133] J. L. Amoros, N. J. Burger, and M. C. Amoros, *The Laue Method* (Academic Press, New York, 1975).

[134] B. D. Cullity, *Elements of X-Ray Diffraction* (Adison-Wesley, Cambridge, 1967).

[135] L. Azaroff, *Elements of X-Ray Crystalography* (McGraw-Hill, New York, 1968).

[136] P. Gammon, Ph.D. thesis, Memorial University of Newfoundland, 1981.

[137] R. Simmons, Transactions ACA **17**, 17 (1981).

[138] Z. Hashin and S. Shtrikman, J. Mech. Phys. Solids **10**, 343 (1962).

[139] P. Bezuglyi, N. Burma, and R. Minyafaev, Sov. Phys. Solid State **8**, 596 (1966).

[140] N. Ashcroft and N. Mermin, *Solid state Physics* (Saunders College, Philadelphia, 1976).

[141] R. Beaumont, H. Chihara, and J. Morrison, Phys. Soc. Proc. **78**, 1462 (1961).

[142] O. Rice, *Statistical Mechanics Thermodynamics and Kinetics* (W.H. Freeman and Company, San Francisco, 1967).

[143] M. L. Klein, G. K. Horton, and J. L. Feldman, Phys. Rev. **184**, 968 (1969).

[144] O. G. Peterson, B. N. Batchelder, and R. O. Simmons, Phys. Rev. **150**, 703 (1966).

[145] D. Losee and R. Simmons, Phys. Rev. **172**, 944 (1968).

[146] E. Gregoryanz, M. Clouter, N. Rich, and R. Goulding, Phys. Rev. B **58**, (1998).

[147] E. Grigoriantz and M. Clouter, J. Low Temp. Phys. **111**, 717 (1998).

[148] M. Born and K. Huang, *Dynamical Theory of Crystal Lattices* (Clarendon Press, Oxford, 1954).

[149] J. Watt and L. Peselnick, J. Appl. Phys. **111**, 1525 (1980).

[150] N. Parsonage and L. Staveley, *Disoreder in Crystals* (Clarendon, Oxford, London, 1978).

[151] G. Briganti *et al.*, Can. J. Phys. **56**, 1182 (1978).

[152] P. Loubeyre *et al.*, Nature **383**, 702 (1996).

# Appendix A

## Brillouin scattering data

Table A.1: Brillouin scattering data for $CH_4$-I at 90 K, $\theta$=85.56$^0$, $\chi$=201.90$^0$.

| Angle $\phi$ | Observed frequency shifts (GHz) | | | Calculated best fit shifts (GHz) | | |
|---|---|---|---|---|---|---|
| | L | $T_1$ | $T_2$ | L | $T_1$ | $T_2$ |
| 253.52 | 8.090 | 4.945 | 3.587 | 8.165 | 4.868 | 3.555 |
| 263.10 | 8.024 | 4.989 | 3.675 | 8.043 | 4.989 | 3.661 |
| 273.04 | 8.096 | 4.897 | 3.684 | 8.059 | 4.934 | 3.700 |
| 283.36 | 8.245 | 4.691 | 3.631 | 8.201 | 4.733 | 3.652 |
| 293.12 | 8.415 | 4.451 | 3.479 | 8.396 | 4.491 | 3.510 |
| 203.25 | 8.592 | 4.230 | 3.313 | 8.580 | 4.281 | 3.324 |
| 213.43 | 8.698 | 4.230 | 3.208 | 8.711 | 4.107 | 3.201 |

Table A.2: Brillouin scattering data for $CH_4$-II at 17.3 K, $\theta$=99.37$^0$, $\chi$=115.83$^0$.

| Angle $\phi$ | Observed frequency shifts (GHz) | | | Calculated best fit shifts (GHz) | | |
|---|---|---|---|---|---|---|
| | L | $T_1$ | $T_2$ | L | $T_1$ | $T_2$ |
| 265.67 | 10.171 | 6.890 | 5.554 | 10.158 | 6.760 | 5.677 |
| 270.67 | 10.148 | 6.871 | 5.661 | 10.080 | 6.867 | 5.688 |
| 275.00 | 10.070 | 6.897 | 5.620 | 10.041 | 6.932 | 5.676 |
| 290.35 | 10.246 | - | 5.485 | 10.229 | - | 5.470 |
| 295.35 | 10.362 | - | 5.225 | 10.380 | - | 5.331 |
| 300.50 | 10.559 | - | 5.225 | 10.567 | - | 5.151 |
| 309.30 | 10.755 | - | 5.054 | 10.842 | - | 4.941 |

Table A.3: Brillouin scattering data for $CD_4$-I at 88.2 K, $\theta=58.91^0$, $\chi=28.18^0$.

| Angle $\phi$ | Observed frequency shifts (GHz) | | | Calculated best fit shifts (GHz) | | |
|---|---|---|---|---|---|---|
| | L | $T_1$ | $T_2$ | L | $T_1$ | $T_2$ |
| 192.98 | 7.707 | 4.158 | 2.667 | 7.707 | 4.247 | 2.611 |
| 202.47 | 7.711 | 4.307 | - | 7.716 | 4.332 | - |
| 211.28 | 7.654 | 4.380 | 2.492 | 7.654 | 4.408 | 2.497 |
| 221.50 | 7.529 | 4.411 | 2.732 | 7.527 | 4.482 | 2.741 |
| 232.08 | 7.404 | - | 3.045 | 7.386 | - | 3.057 |
| 240.59 | 7.262 | 4.692 | 3.350 | 7.263 | 4.475 | 3.388 |
| 250.93 | 7.195 | - | 3.660 | 7.202 | - | 3.658 |

Table A.4: Brillouin scattering data for $CD_4$-II at 32.0 K, $\theta=135.23^0$, $\chi=113.80^0$.

| Angle $\phi$ | Observed frequency shifts (GHz) | | | Calculated best fit shifts (GHz) | | |
|---|---|---|---|---|---|---|
| | L | $T_1$ | $T_2$ | L | $T_1$ | $T_2$ |
| 113.11 | 9.563 | - | 3.987 | 9.669 | - | 4.127 |
| 123.31 | 9.457 | - | 4.113 | 9.538 | - | 4.139 |
| 133.52 | 9.238 | - | 4.311 | 9.317 | - | 4.285 |
| 143.87 | 9.117 | - | 4.647 | 9.020 | - | 4.594 |
| 153.34 | 8.639 | - | 5.209 | 8.664 | - | 5.029 |
| 163.92 | 8.2515 | - | 5.501 | 8.285 | - | 5.510 |
| 173.35 | 8.0432 | 6.040 | 5.990 | 7.973 | 5.994 | 5.900 |

Table A.5: Brillouin scattering data for $CD_4$-III at K, $\theta$=135.23$^0$, $\chi$=113.80$^0$.

| Angle $\phi$ | Observed frequency shifts (GHz) | | | Calculated best fit shifts (GHz) | | |
|---|---|---|---|---|---|---|
| | L | $T_1$ | $T_2$ | L | $T_1$ | $T_2$ |
| 113.11 | 9.870 | 5.555 | 5.785 | 9.757 | 5.629 | 5.569 |
| 123.11 | 9.752 | 5.493 | - | 9.753 | 5.680 | - |
| 128.11 | 9.638 | - | 5.698 | 9.742 | - | 5.669 |
| 133.11 | 9.670 | 5.639 | - | 9.726 | 5.786 | - |
| 143.11 | 9.658 | 5.880 | - | 9.679 | 5.882 | - |
| 153.11 | 9.629 | - | 5.930 | 9.621 | - | 5.893 |
| 163.11 | 9.629 | - | 6.078 | 9.567 | - | 5.985 |

# Appendix B

# X-ray diffraction pattern and Brillouin spectra

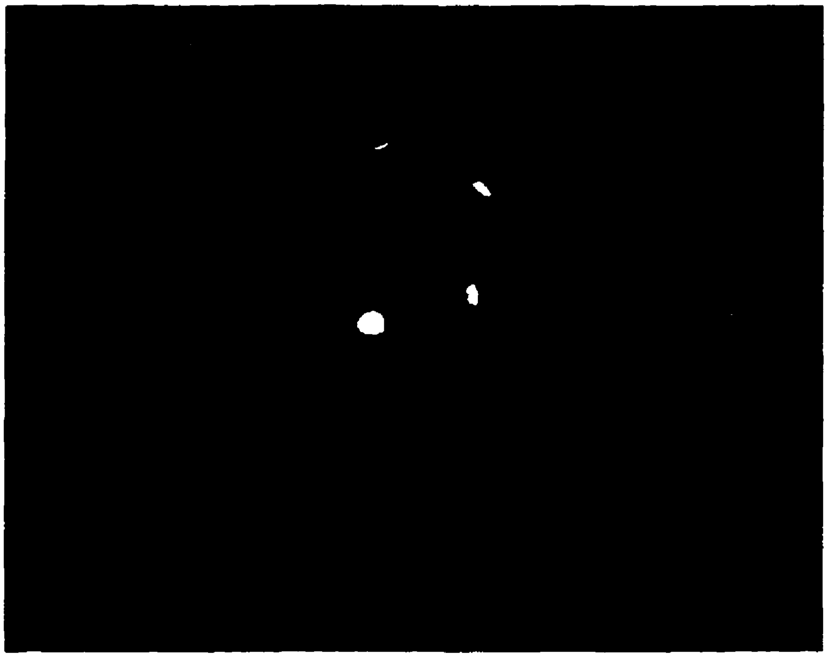

Figure B.1: The diffraction pattern of $CH_4$-I at 90 K.

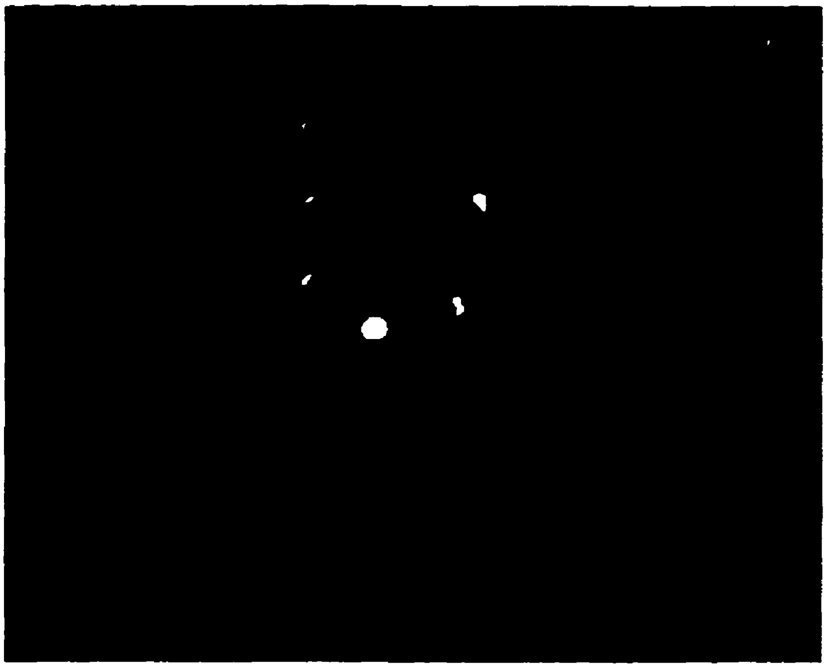

Figure B.2: The diffraction pattern of $CH_4$-I at 22 K after crystal has gone twice through the I-II phase transition.

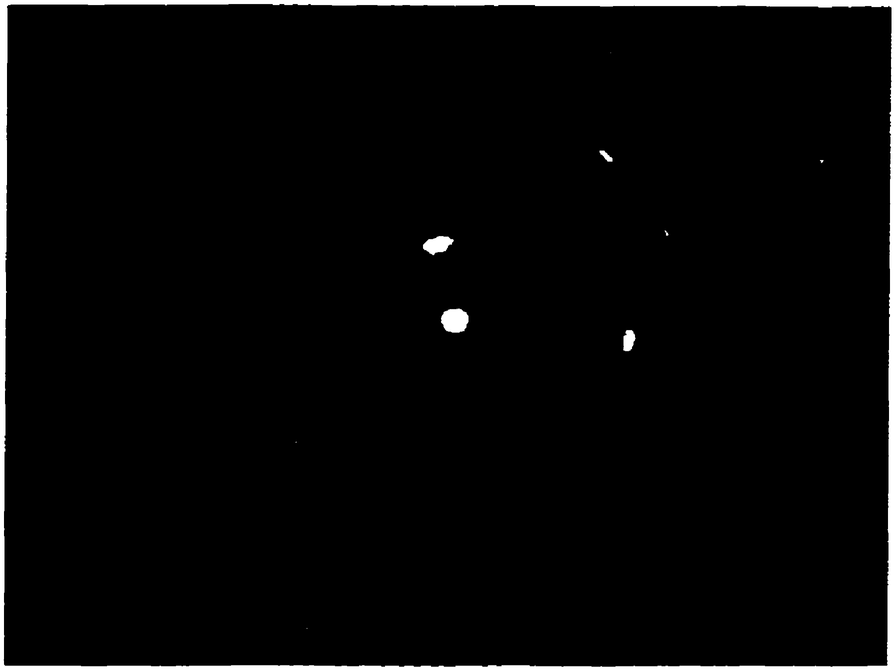

Figure B.3: The diffraction pattern of $CD_4$-I at 88.2 K.

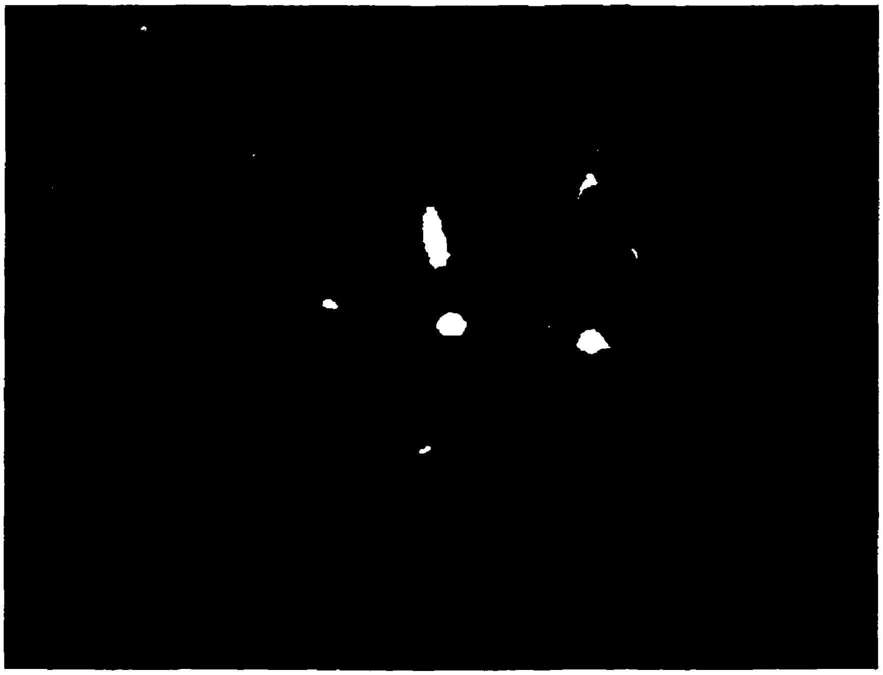

Figure B.4: The diffraction pattern of $CD_4$-II at 25 K.

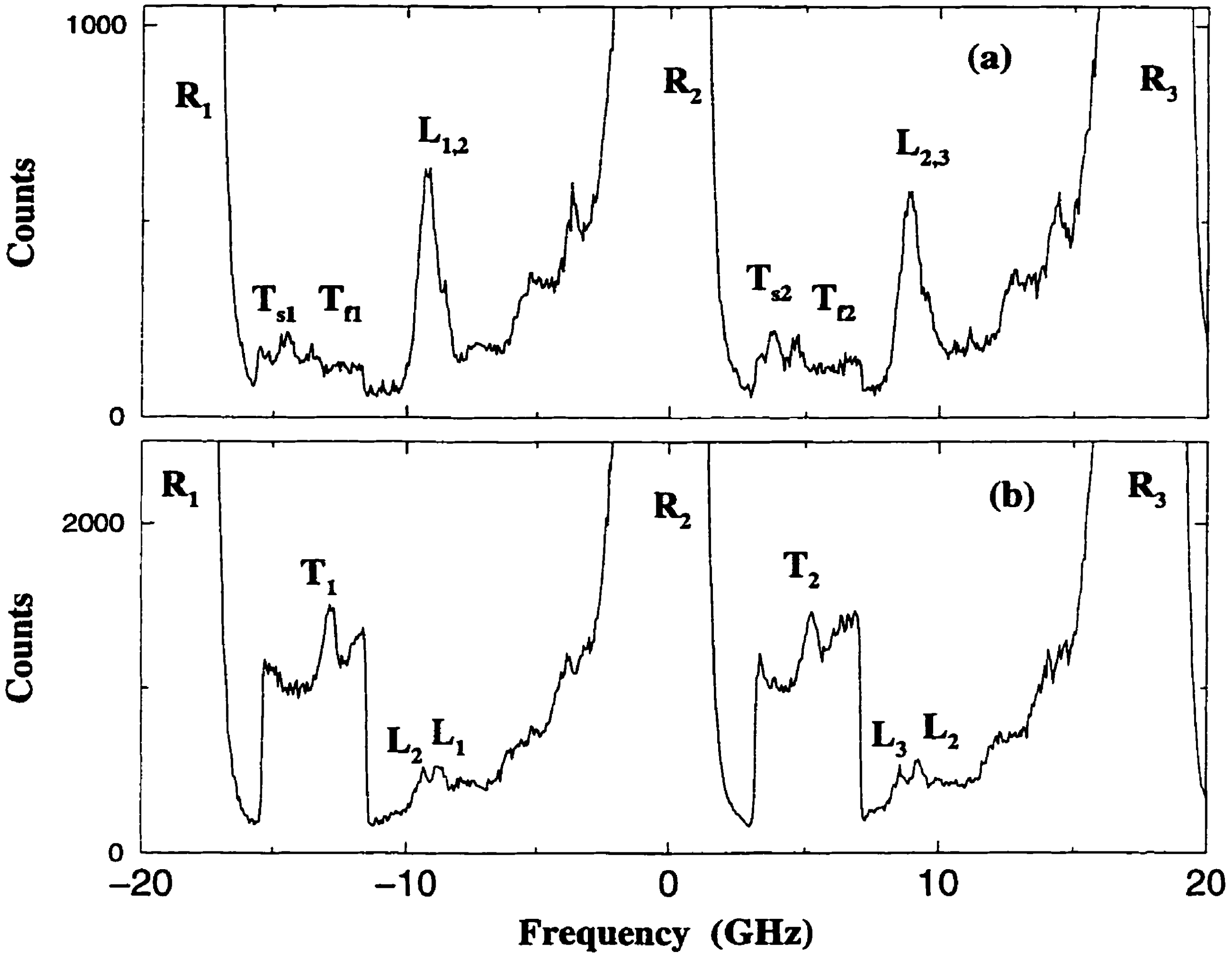

Figure B.5: Representative Brillouin spectra of $CD_4$ in phases I (a) and III (b). The Rayleigh peaks are labeled $R_i$, longitudinal $L_i$, where $i$ is the number of corresponding Rayleigh and longitudinal peak. Transverse modes are labeled $T_{(s,f)i}$ where $s,f$ stand for slow and fast transverse modes and $i$ shows the Rayleigh peak to which a given transverse peak belongs.

# IMAGE EVALUATION TEST TARGET (QA-3)

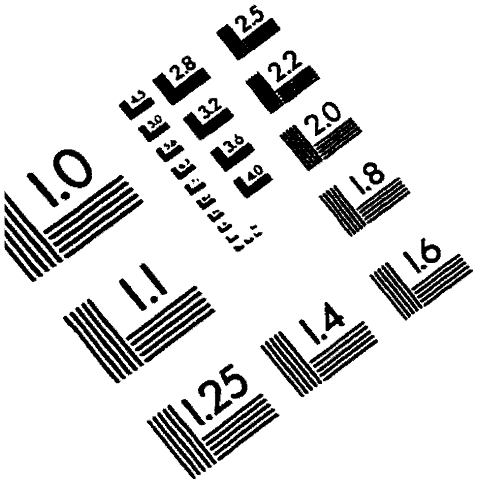
1.0
1.1
1.25
1.4
1.6
1.8
2.0
2.2
2.5
2.8
3.2
3.6
4.0

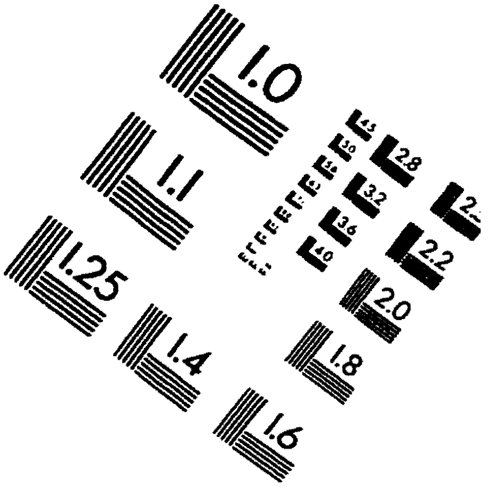
1.0
1.1
1.25
1.4
1.6
1.8
2.0
2.2
2.8
3.2
3.6
4.0

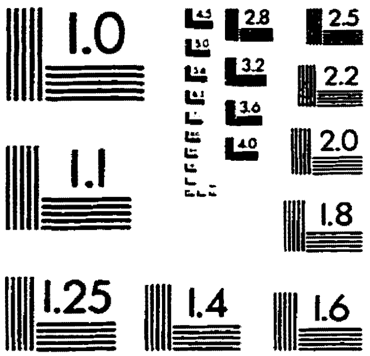
1.0
2.8
2.5
3.2
2.2
3.6
2.0
4.0
1.1
1.8
1.25
1.4
1.6

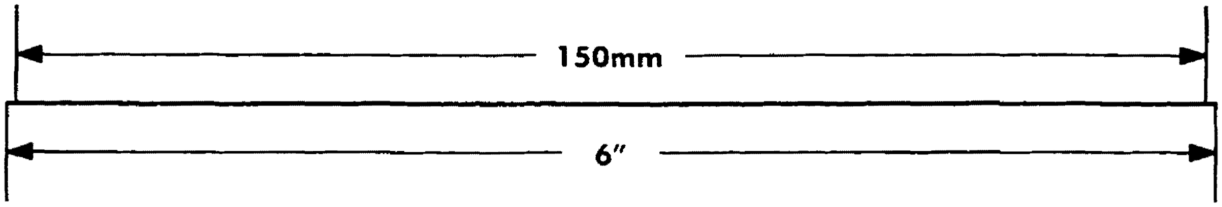

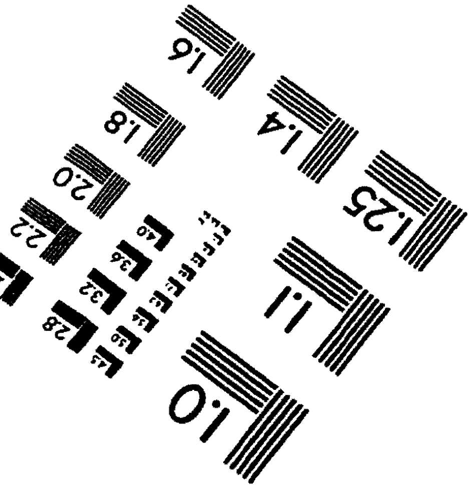
1.6
1.8
1.4
2.0
1.25
2.2
4.0
3.6
1.1
3.2
2.8
1.0

APPLIED IMAGE . Inc
1653 East Main Street
Rochester, NY 14609 USA
Phone: 716/482-0300
Fax: 716/288-5989

© 1993, Applied Image, Inc., All Rights Reserved

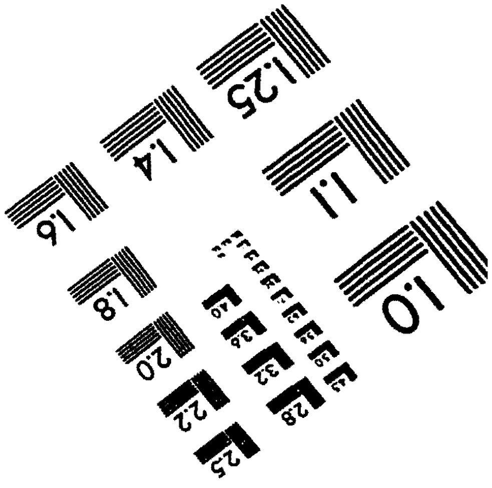
1.25
1.4
1.1
1.6
1.0
1.8
4.0
3.6
2.0
3.2
2.8
2.2
2.5